

RTTOV v14

SCIENCE AND VALIDATION REPORT

James Hocking¹, Brett Candy¹, Mhari Dell¹, David Rundle¹, Alan Geer², Cristina Lupu², Tracy Scanlon², Emma Turner², Mary Borderies³, Philippe Chambon³, Jean-Marie Lalande³, Jérôme Vidot³, Florian Baur⁴, Christina Köpken-Watts⁴, Pascal Raisig⁴, Leonhard Scheck⁴, Olaf Stiller⁴, Christina Stumpf⁴, Vasileios Barlakas⁵, Eva Borbas⁶, Laurent Labonnote⁷, Rohit Mangla⁸

Affiliations:

¹*Met Office, U.K.*

²*European Centre for Medium Range Weather Forecasts*

³*MétéoFrance*

⁴*Deutscher Wetterdienst*

⁵*CS Group - Germany GmbH*

⁶*University of Wisconsin*

⁷*University of Lille*

⁸*Centre for Remote Imaging, Sensing and Processing, National University of Singapore*

This documentation was developed within the context of the EUMETSAT Satellite Application Facility on Numerical Weather Prediction (NWP SAF), under the Cooperation Agreement dated 7 September 2021, between EUMETSAT and the Met Office, UK, by one or more partners within the NWP SAF. The partners in the NWP SAF are the Met Office, ECMWF, DWD and Météo France.

Copyright 2025, EUMETSAT, All Rights Reserved.

Change record			
Version	Date	Author / changed by	Remarks
0.1	14/10/2024	J Hocking	Initial template requesting input from developers
0.2	21/01/2025	All	First full draft nearing completion
1.0	29/01/2025	All	Complete version
1.0.1	31/01/2025	TS/AG/CS/JH	Final minor updates after comments

Table of contents

1.	Introduction	4
2.	Scientific changes from RTTOV v13 to RTTOV v14	5
2.1	Changes to profile structure	6
2.1.1	Interpolation in RTTOV	9
2.1.2	Impact of interpolation on direct model	11
2.1.3	Impact of interpolation on Jacobians	14
2.2	Updates to microwave coefficients	19
2.2.1	Microwave spectroscopy	19
2.2.2	Variable ozone for microwave sensors	23
2.3	Zeeman coefficients based on v13 predictors	24
2.3.1	Comparison with previous Zeeman coefficients	27
2.3.2	Zeeman validation statistics	28
2.4	UV simulations	31
2.5	Rayleigh scattering depolarisation	34
2.6	RTTOV-SCATT science implemented in RTTOV	35
2.6.1	Delta-Eddington solver	35
2.6.2	Cloud overlap options	37
2.6.3	Radar solver	38
2.6.4	Other scattering options and calculations	39
2.7	Tang <i>et al</i> /modification to Chou-scaling	40
2.8	MFASIS-NN solver	42
2.8.1	General concept	42
2.8.2	Heterogeneous surfaces	46
2.8.3	Quality flags	46
2.8.4	Code vectorisation	47
2.8.5	MFASIS-NN accuracy and available instrument channels	47
2.9	Flexible VIS/IR hydrometeor optical properties	51
2.10	ICON-ART aerosol optical properties	52
2.11	Updates to microwave hydrometeor optical properties	53
2.11.1	Large hydrometeor contents	53
2.11.2	New PSD options	56
2.11.3	Updates on the bright-band	58

2.11.4	Phase functions	59
2.12	Physically based polarisation treatment	61
2.13	Per-channel effective T _{skin} input	63
2.14	Microwave sea surface emissivity models	64
2.15	Heterogeneous surfaces	66
2.16	Updates to treatment of diffuse reflectance	72
2.17	Updates to land surface emissivity/BRDF atlases	73
2.17.1	Interface to CAMEL v3 atlases	73
2.17.2	Option to return nearby emissivity/BRDF values	78
2.18	Generalisation of dynamic emissivity retrieval outputs	78
2.19	Updated NLTE coefficients	80
2.20	PC-RTTOV updates	83
2.21	Additional changes to RTTOV inputs, outputs and internal calculations	84
2.21.1	Changes to default option values	84
2.21.2	Changes to RTTOV outputs	84
2.21.3	Capabilities that have been removed	85
2.21.4	Deprecation of older optical depth coefficients	87
3.	Testing and Validation of RTTOV v14	88
3.1	Comparison of simulations between RTTOV v13 and RTTOV v14	88
3.1.1	MTG FCI comparisons	88
3.1.2	MetOp IASI comparisons	95
3.1.3	MetOp GOME-2 comparisons	98
3.1.4	Suomi-NPP ATMS comparisons	98
3.1.5	MetopSG ICI comparisons	101
3.2	Comparisons with observations - IFS	103
3.2.1	Monitoring results	103
3.2.2	Data assimilation results – full cycling results	108
4.	Summary	113
5.	Acknowledgements	117
6.	References	117

1. Introduction

The purpose of this report is to document the scientific aspects of the latest version of the NWP SAF fast radiative transfer model, referred to hereafter as RTTOV v14, which are different from the previous model RTTOV v13 and present the results of the validation tests comparing the two versions of RTTOV which have been carried out. The enhancements to this version, to be released in early 2025, have been made under the auspices of the EUMETSAT [NWP SAF](#).

The RTTOV v14 software is available at no charge to users on request from the NWP SAF [web site](#). Note the licence agreement must first be accepted on the web site after registering [here](#). RTTOV v14 documentation, including the latest version of this document, can be viewed on the [NWP SAF web site](#), and may be updated from time to time. Technical documentation about the software and how to run it can be found in the RTTOV v14 user's guide which can also be downloaded from the link above and is provided as part of the package distributed to users.

The baseline document for the original version of RTTOV is available from ECWMF as Eyre (1991) and the basis of the original model is described in Eyre and Woolf (1988). This was updated for RTTOV v5 (Saunders *et al* 1999a, Saunders *et al*, 1999b) and for RTTOV v6, RTTOV v7, RTTOV v8, RTTOV v9 (Matricardi *et al*, 2004), RTTOV v10, RTTOV v11, RTTOV v12, and RTTOV v13 with the respective science and validation reports for each version hereafter referred to as R7REP2002, R8REP2006, R9REP2008, R10REP2010, R11REP2013, R12REP2017, and R13REP2020 respectively all available from the NWP SAF web site at the link above and the links to the individual reports are given in the [references section](#) of this report. A more recent peer review paper giving an overview of RTTOV is Saunders *et al* (2018) to which new users of RTTOV are referred. The changes described here only relate to the scientific differences from RTTOV v13. The RTTOV v14 user guide lists the scientific and technical differences between RTTOV v13 and v14 and the RTTOV v14 user interface changes document provides detailed advice for users who are upgrading to RTTOV v14 from an earlier version.

This document also describes comparisons and validations of the output values from this new version of the model by comparing with previous versions, other models, and observations. In general, only aspects related to new and improved science are presented in this report, but some results are presented of the overall performance of the new RTTOV package. Many of the details of the new science are given in other papers/reports which are referenced in this document and so only a summary is presented here in order to keep this document manageable in size. [Section 2](#) describes the individual scientific changes in RTTOV v14 and the changes they make to simulations. [Section 3](#) describes the overall

performance of the new model for a limited number of satellite instruments. [Section 4](#) gives a summary.

2. Scientific changes from RTTOV v13 to RTTOV v14

RTTOV v14 comprises significant changes compared to RTTOV v13. The main scientific changes are listed here in addition to changes implemented in RTTOV v13.1 and v13.2:

- The representation of the vertical profile has changed in v14 in respect of the way the pressure levels and layers are defined. The surface pressure now *always* lies at the bottom of the atmospheric profile, which means v14 cannot be run on input profiles that are defined on fixed pressure levels. This implies that the RTTOV internal interpolator is always used.
- Updated microwave spectroscopy and coefficients for microwave sensors now include variable ozone.
- Zeeman coefficients are available based on v13 predictors.
- Simulations for UV sensors are now possible.
- Depolarisation is now accounted for in the Rayleigh scattering phase function.
- Scattering simulations for MW sensors are now done through the main RTTOV model (rather than using the separate RTTOV-SCATT model which no longer exists). The delta-Eddington solver is now available in RTTOV for IR and MW sensors, and other scientific capabilities from RTTOV-SCATT have been implemented within RTTOV.
- The Tang *et al* (2018) modification to the Chou-scaling fast solver for IR scattering has been implemented.
- The MFASIS-NN neural network based fast visible/near-IR scattering solver has been further improved and extended to more frequencies on top of the initial implementation in RTTOV v13.2 and the less accurate LUT version is no longer available.
- The VIS/IR hydrometeor optical properties are now fully flexible in the same way as aerosol and MW hydrometeor properties. In all cases the optical property files define properties for an arbitrary collection of particle types that may be used separately or together in any combination in the simulations.
- New aerosol optical property tables are available defining optical properties for a subset of ICON-ART aerosol species.
- MW hydrometeor optical property training options have been updated to improve melting layer treatment and to add new particle size distributions.
- An alternative physically-based treatment of polarisation, ARO-scaling, has been implemented.
- Optional input of per-channel effective skin temperature.

- A new neural network based MW sea surface emissivity model, SURFEM-Ocean, has been implemented.
- Heterogeneous surfaces: option to associate each profile with more than one surface, each of which has its own set of associated properties and surface coverage fraction.
- Updates to the treatment of diffuse reflectance in RTTOV.
- Support for the CAMEL v3 single-year and climatology IR land surface emissivity atlases.
- Dynamic emissivity retrieval generalised to clear-sky and all cloud overlap options.
- New/updated NLTE coefficients for IASI, IASI-NG, MTG-IRS based on LBLRTM v12.8.
- Updates to PC-RTTOV.

Each sub-section below gives more details on each of these components and references as required for all the details.

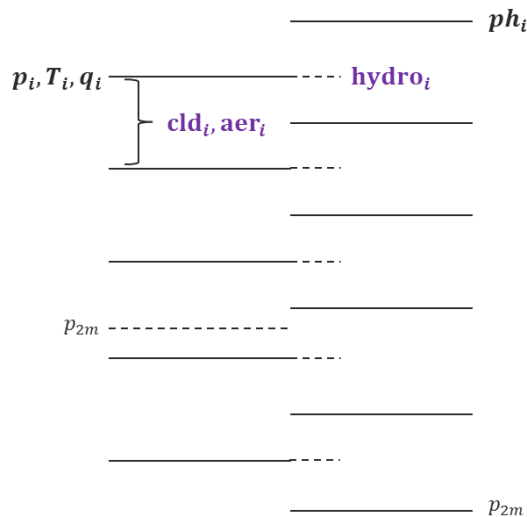
2.1 Changes to profile structure

A major design goal in RTTOV v14.0 was to unify the RTTOV-SCATT model (previously the separate radiative transfer model for hydrometeor scattering for microwave sensors) with the core RTTOV model that performs clear-sky simulations at all wavelengths and scattering simulations for ultra-violet/visible/infrared sensors. Unifying the models yields much improved consistency in the treatment of scattering across the whole spectrum which is a strong motivation as all-sky radiance assimilation gains increasing focus in NWP centres around the world. It also benefits users in a technical sense, by providing a single common interface to all types of simulations in RTTOV.

[Section 2.6](#) discusses the implementation of the science contained in RTTOV-SCATT within RTTOV v14. Before those updates could be implemented it was necessary first to consider the representation of the vertical atmospheric profile in RTTOV v13 as this is different to that in RTTOV-SCATT. Figure 2.1.1 illustrates the profile structure in RTTOV v13 and RTTOV-SCATT and shows the new structure in RTTOV v14.

NWP models typically provide fields of temperature, water vapour, cloud and other variables on the same vertical grid. RTTOV v13 and earlier require temperature, water vapour and other gases on pressure levels, and require scattering inputs (clouds, aerosols) on the layers bound by those levels. This is inconsistent with the NWP model representation of the atmosphere and typically means that there is a half-layer vertical shift in the scattering profiles in RTTOV with respect to the NWP model. This results in systematic biases in RTTOV scattering simulations for ultra-violet/visible/infrared sensors.

RTTOV v13 / RTTOV-SCATT



RTTOV v14

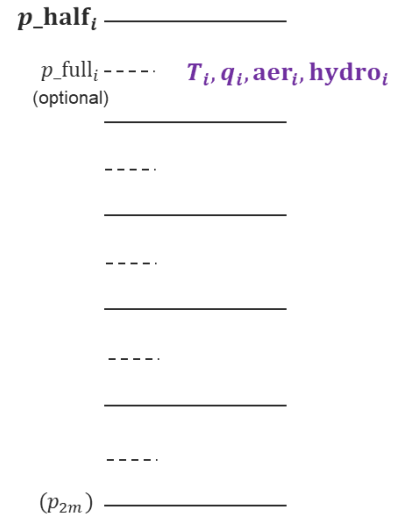


Figure 2.1.1: Input atmospheric profile structure in RTTOV v13 and RTTOV-SCATT, and the new structure in RTTOV v14. See description in the text.

By contrast, RTTOV-SCATT requires pressure half-levels to be defined in addition to the standard RTTOV profile pressure (full-)levels. It uses the same temperature and water vapour inputs as RTTOV, while the hydrometeor inputs for microwave scattering are provided on the pressure full-levels for the layers bound by the half-levels. This means the RTTOV-SCATT scattering inputs are provided on the same vertical grid as the temperature and water vapour, which is consistent with NWP models, but inconsistent with RTTOV.

The RTTOV gas absorption optical depth parameterisation operates on fixed pressure levels. In early versions of RTTOV, the input profiles had to be provided on those fixed pressure levels requiring the surface pressure (p_{2m}) to be an independent input. The radiative transfer equation is integrated down to the surface pressure. The partial layer between the surface pressure and the first pressure level above must always be treated as a special case for every solver that is implemented in RTTOV which introduces complexity into the code.

In RTTOV v9 an interpolator was implemented (R9REP2008) within RTTOV allowing users to input profiles on arbitrary pressure levels, and then RTTOV performs the interpolation to the fixed levels for the optical depth regression and interpolates the computed optical depths back to the input pressure levels for the radiance calculation. Since that version, this has been the recommended way of calling RTTOV because it is scientifically better to carry out the radiance calculation using atmospheric profile data on the native NWP model vertical

grid rather than interpolating the profile to the fixed pressure levels, especially when the NWP model has finer vertical resolution than the fixed coefficient levels.

By contrast, in RTTOV-SCATT the interpolator must always be used, and the surface must always lie on the bottom pressure half-level. It does not allow the surface to be specified independently of the pressure levels. This was another difference between the two models that had to be reconciled for RTTOV v14.

Since it is strongly recommended to use the RTTOV interpolator, and as the surface lies on the bottom level for most NWP models, and because the treatment of the independent surface pressure added complexity to the RTTOV code, it was decided in RTTOV v14 to move to the RTTOV-SCATT representation of the atmosphere as illustrated in Figure 2.1.1.

The pressure half-levels are a mandatory input. The top half-level can be at 0 hPa but does not need to be. It should be sufficiently small that the pressure half-levels encompass the weighting functions of the channels being simulated (this is true for any radiative transfer model). The bottom pressure half-level is implicitly the surface pressure. There is no independent surface pressure input variable in RTTOV v14.

The pressure half-levels define atmospheric layers. Each layer is associated with a pressure full-level. The half-level and full-level terminology is consistent with NWP models like ECMWF's Integrated Forecast System (IFS). The pressure full-levels are an optional input. If not defined (i.e., if any input values are zero) the full-level pressures are computed as the mean of adjacent half-level pressures. This is consistent with models like the IFS. For some NWP models, the full-level pressures are computed differently. In these cases, users may wish to input the full-level pressures explicitly to be as consistent as possible with the NWP model. All profile input variables (temperature, water vapour, trace gases, hydrometeors/ clouds, aerosols) are provided on the pressure full-levels. This now provides a consistent profile representation for scattering across the spectrum, is more consistent with NWP models, and eliminates the complexity in the code associated with having an independent surface pressure variable.

As there is no independent surface pressure in RTTOV v14, the surface pressure Jacobian may be obtained by enabling the *pressure_gradients* option (so that pressure is an active TL/AD/K variable), and then the surface pressure Jacobian is contained in the bottom pressure half-level of the *profiles_k* Jacobian output.

The radiance solvers in RTTOV carry out calculations for the layers bound by the pressure half-levels. These solvers require temperature values on the pressure half-levels. In addition, the local path geometry calculations (which include computing pressure half- and full-level altitudes, and local zenith angles due to Earth curvature and refraction) require temperature and water vapour concentration on the half-levels. These half-level values are

obtained by linear interpolation of the full-level profiles in log-pressure within RTTOV. The top-most half-level values are set equal to the values in the top full-level. The bottom-most half-level values are either set equal to the values in the bottom full-level, or for temperature and water vapour, they may be taken from the 2m values as discussed next.

The 2m temperature (t_{2m}) and 2m water vapour (q_{2m}) are now both optional inputs to RTTOV v14 (previously only q_{2m} was optional). These are enabled/disabled via the *use_t2m* and *use_q2m* options respectively. When enabled, the bottom half-level (atmospheric) temperature and water vapour concentrations are set to t_{2m} and q_{2m} respectively. These are then used in the radiance solvers and geometry calculations as discussed above. In addition, when enabled, the 2m values are used in computing the predictors for the optical depth calculations. [Section 2.1.1](#) describes the profile interpolation and illustrates how the 2m values are used. (Note that t_{2m} is the atmospheric temperature just above the surface and is distinct from the surface skin temperature which is a separate input to RTTOV).

The top half-level may be set equal to or arbitrarily close to 0 hPa. This means that the altitude and hence layer thickness of the top-most layer cannot be calculated accurately. Layer thickness is required for scattering calculations. Any scattering inputs (aerosols, hydrometeors) in the top-most atmospheric layer (i.e., at the top pressure full-level) are ignored by RTTOV v14. This should not be a limitation as there should be no such scattering particles at the top of the atmosphere.

For non-scattering simulations for microwave sensors including absorption by cloud liquid water (CLW), the calculation of layer CLW content has changed. In RTTOV v13 the CLW profile is input on the vertical pressure levels, and the calculations are done for the layers bound by adjacent pairs of pressure levels. The CLW layer concentrations are computed as the mean of CLW concentrations on the bounding pressure levels. In RTTOV v14, the CLW profile is provided on pressure full-levels, and the calculations are done for the layers bound by adjacent pairs of pressure half-levels. The input CLW values are used directly to represent the layer concentrations.

These various changes to the profile representation affect RTTOV in a fundamental way and as such v14 cannot replicate v13 radiances. Comparisons of v13 and v14 are shown in [section 3](#) for a variety of sensors and simulation types.

2.1.1 Interpolation in RTTOV

The optical depth parameterisation in RTTOV is carried out for layers defined by fixed pressure levels (“coefficient levels”). The input profiles on user-specified pressure levels are interpolated onto the coefficient levels. The predictors for the optical depth regression are calculated from the layer values, and the optical depths are obtained from the regression. The resulting optical depths are interpolated back into the user levels, and all subsequent

calculations are carried out on the user levels. These interpolation steps are illustrated in Figure 2.1.2.

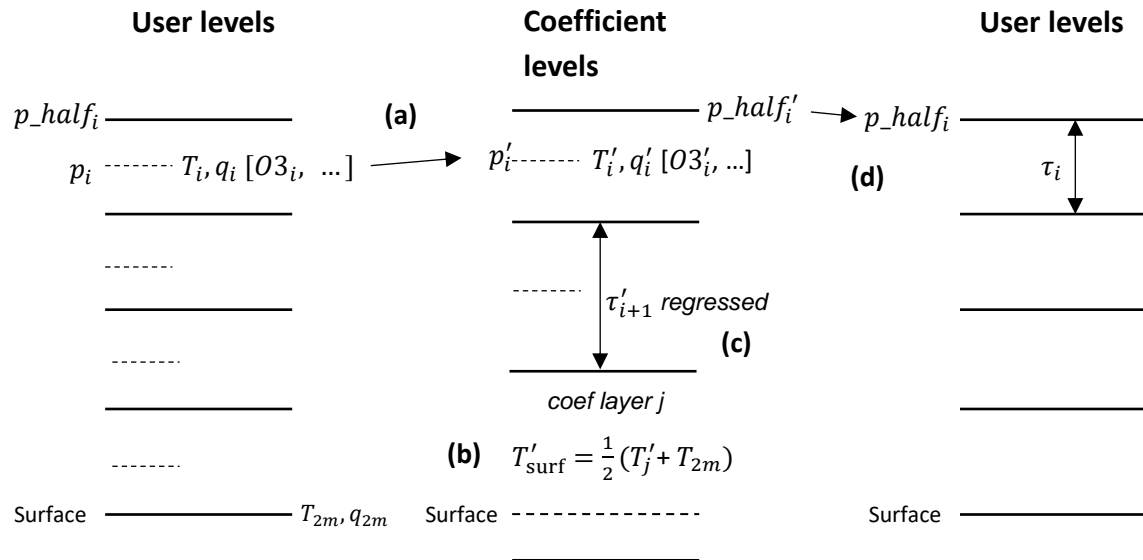


Figure 2.1.2: (a) Interpolation of input profiles of temperature and gas concentrations from user levels to coefficient levels is based on the pressure full levels. Quantities on coefficient levels are denoted by primes (').

(b) For the coefficient layer containing the surface, the temperature and water vapour values incorporate the 2m T and q values if the relevant options are enabled (only temperature is shown).

(c) Layer gas absorption optical depths are computed using the gas optical depth regression for the layers bound by the coefficient levels.

(d) Interpolation of the layer optical depths back onto user levels is based on the pressure half-levels.

As noted in [section 2.1](#), if enabled, the 2m temperature and/or water vapour are used in the predictor calculations for the coefficient layer containing the surface. In that case the temperature/water vapour concentration of the surface layer is computed as the mean of the interpolated value for that layer and the corresponding 2m variable value.

The original interpolator implemented in RTTOV v9 (R9REP2008) was based on the scheme described by Rochon *et al* (2007). In RTTOV v11, additional interpolation modes were introduced (Hocking, 2014, henceforth "H14") in order to eliminate the jaggedness observed in Jacobians in certain cases. A study was carried out, described in H14, to determine the optimal interpolation mode. In that study, it was determined that modes 4 and 5 were recommended when the input levels are more densely spaced than the coefficient

levels, and modes 1 or 3 were recommended otherwise. Table 2.1.1 reproduces Table 1 in H14, summarising the interpolation modes available in RTTOV.

Mode	Profile interpolation	Optical depth interpolation
1	Rochon	Rochon on optical depths
2	Log-linear	Log-linear of optical depths
3	Rochon	Log-linear on optical depths
4	Rochon	Rochon on $\Delta\tau / \Delta p$
5	Rochon	Log-linear on $\Delta\tau / \Delta p$

Table 2.1.1: The five interpolation modes available in RTTOV. Each mode involves two interpolation steps, first the input profile is interpolated onto coefficient levels. Level-to-space optical depths are calculated for the coefficient levels, and these are then interpolated onto the user (input) levels.

The changes to the profile representation mean that the interpolation is done differently in RTTOV v14: the first interpolation step from user levels to coefficient levels is carried out on pressure full-levels resulting in profile values for the coefficient layers. These interpolated values are used directly in the predictor calculations. Coefficient full-level pressures are computed as the mean of adjacent coefficient half-level pressures. This is different to RTTOV v13 and earlier where the values on user pressure *levels* were interpolated onto the coefficient pressure *levels*, and then the coefficient *layer* values were obtained by taking the mean of interpolated values on adjacent coefficient levels. The atmospheric predictors were then computed from these averaged values.

This change in RTTOV v14 requires that a new study is carried out to determine the optimal interpolation mode(s) under the modified profile representation. This replicates the methodology used in section 3 of H14.

2.1.2 Impact of interpolation on direct model

To compare the interpolation modes for the forward model, a line-by-line (LBL) radiative transfer model is run to generate channel-integrated transmittances for all ATMS channels for a diverse set of 52 profiles. These are computed on various sets of vertical pressure levels and corresponding brightness temperatures are computed using a simple integration of the radiative transfer equation assuming a nadir observation and surface emissivity of 1. These are compared with brightness temperatures computed via the same calculation using transmittances from RTTOV for the same input profiles. RTTOV gas optical depth coefficients on either 54 or 101 levels are used. The LBL brightness temperatures are considered to be the “truth”, and the RMS brightness temperature differences are computed for RTTOV runs with each interpolation mode. The differences between the LBL and RTTOV brightness temperatures come from the errors introduced by the optical depth regression and from the interpolation. The differences between the different RTTOV brightness temperatures are due solely to the interpolation mode used.

Figure 2.1.3 shows plots for “case 1” in which the input levels are more densely spaced than the coefficient levels. Interpolation modes 4 and 5 result the smallest differences to the LBL across these cases. The top two plots may be compared directly with Figures 7 and 8 in H14. This shows that the interpolation errors in RTTOV v14 with modes 4 and 5 are generally significantly smaller than for the previous RTTOV versions in all channels. The lower right plot also indicates the potential benefits in terms of accuracy that optical depth coefficients on 101L may yield when there is a larger number of input levels.

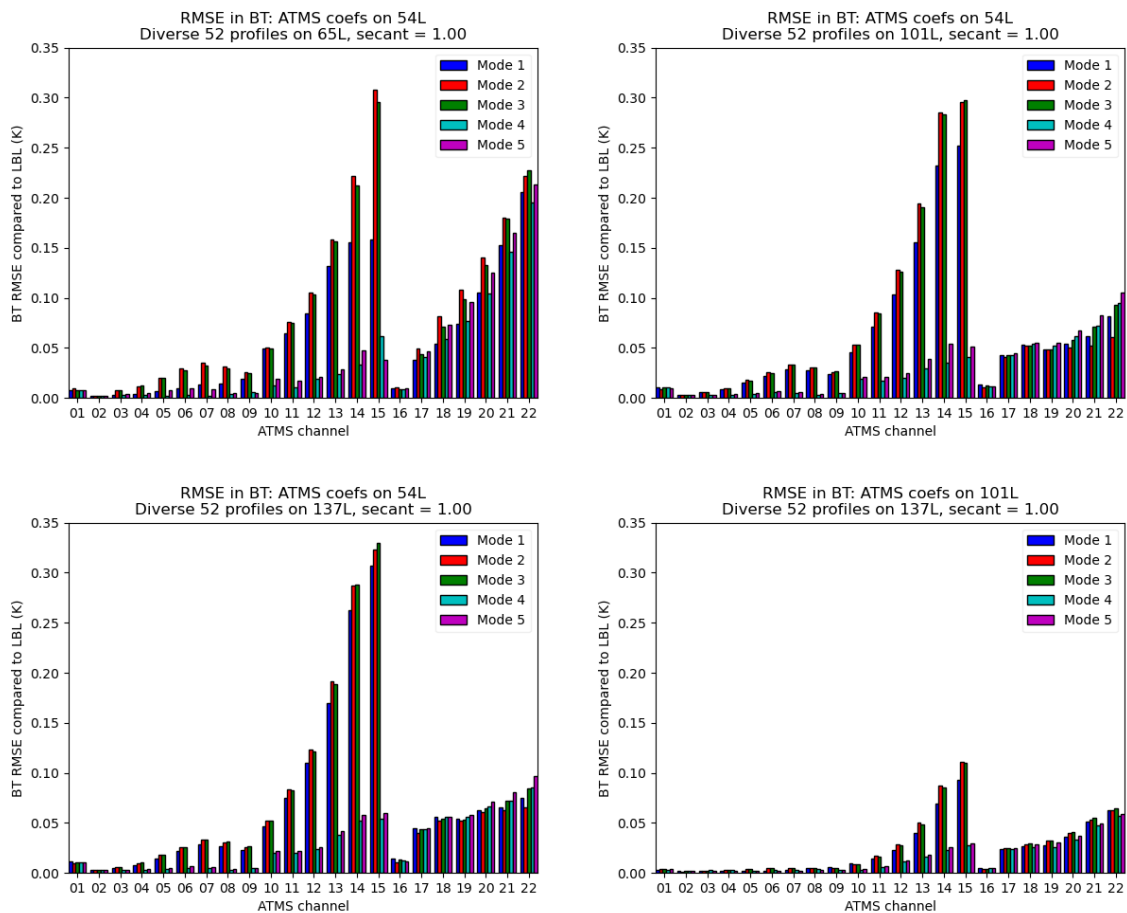


Figure 2.1.3: RTTOV vs LBL brightness temperature RMS differences for ATMS for the five RTTOV interpolation modes. Each plot shows results for input profiles on a particular set of 65, 101, or 137 levels and RTTOV coefficients on either 54 or 101 levels as indicated in the plot titles. These are cases where the input levels are more densely spaced than the coefficient levels.

Figure 2.1.4 shows plots for “case 2” in which the user levels are more sparse than the coefficient levels. Overall mode 5 appears to yield the smallest differences to the LBL across these cases. The top two plots may be directly compared to Figures 12 and 13 in H14. This

shows that for the temperature sounding and window channels, RTTOV v14 has smaller interpolation errors than the earlier RTTOV versions for this case. However, for the water vapour channels the interpolation errors appear similar for coefficients on 54L and larger in v14 for coefficients on 101L with the input profiles on 44L.

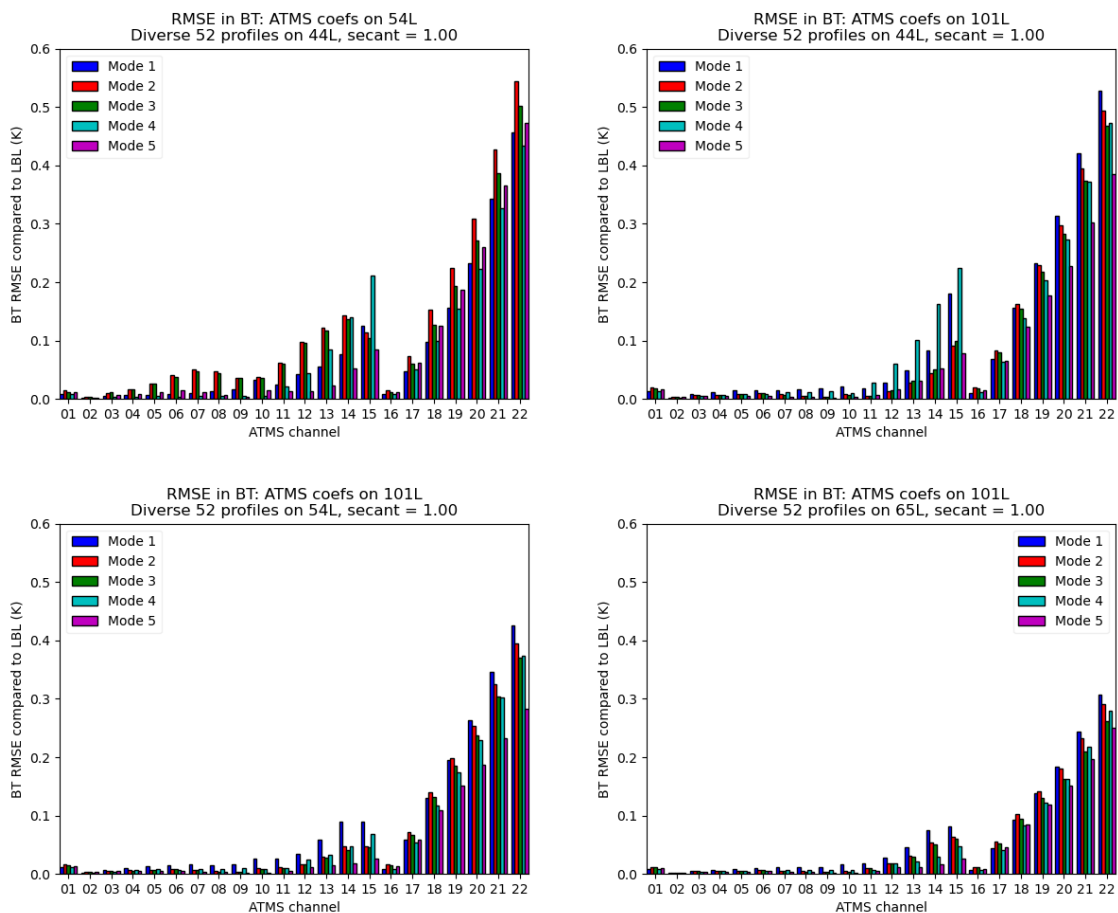


Figure 2.1.4: RTTOV vs LBL brightness temperature RMS differences for ATMS for the five RTTOV interpolation modes. Each plot shows results for input profiles on a particular set of 44, 54, or 65 levels and RTTOV coefficients on either 54 or 101 levels as indicated in the plot titles. These are cases where the input levels are more sparsely spaced than the coefficient levels.

In practice, modern NWP models typically have more than 60 vertical levels and it is strongly recommended to input profiles to RTTOV v14 on the native NWP model levels.

Overall, the results indicate that for the window and lower-peaking temperature sounding channels (1-9, 16), the interpolation errors in RTTOV v14 with modes 4 and 5 are sufficiently small to be considered negligible. This is a significant improvement over previous versions

of RTTOV. For the temperature sounding channels (10-15), the errors are well below 0.1 K with modes 4 and 5 for all cases with input profiles on at least 54L (which is usual in contemporary operational NWP systems as noted above). This is also an overall improvement compared to the previous versions of RTTOV. For the water vapour channels (18-22) and the window channel at 166 GHz (17), the results are more mixed. Modes 4 and 5 yield errors up to around 0.1 K in channel 22 (the highest peaking water vapour channel) when the number of input levels exceeds around 100. However, interpolation errors with modes 4 and 5 are generally largest for these channels in case 2 and in particular when the number of input levels is small.

The results above are generally a positive indication that interpolation errors are smaller in RTTOV v14 than previous versions for the most common use cases, with the possible exception of water vapour channels in the case where the number of input levels is less than the number of coefficient levels. On the basis of these results, modes 4 and 5 are recommended to users, with mode 5 being preferable to minimise interpolation errors in the case where the number of input levels is less than the number of coefficient levels.

2.1.3 Impact of interpolation on Jacobians

An important reason for implementing the alternative interpolation modes originally was to eliminate oscillations that were observed particularly in temperature Jacobians. In this section we consider temperature and water vapour Jacobians with the different interpolation modes for the mean profile from the 52 profile set where surface emissivities are computed for a sea surface. Only modes 1, 3, 4 and 5 are considered as mode 2 is not suitable for Jacobian calculations as discussed in H14.

Figures 2.1.5 and 2.1.6 show the temperature and water vapour Jacobians for ATMS for “case 1” where the input profile is on 101 levels and the coefficients are on 54 levels. The oscillations are evident in the temperature Jacobians for mode 1 as discussed in H14. Mode 5 exhibits some “artefacts” (oscillations) in the lower layers (to the right of the plots) in both the temperature and water vapour Jacobians. Mode 4 gives the smoothest Jacobians overall.

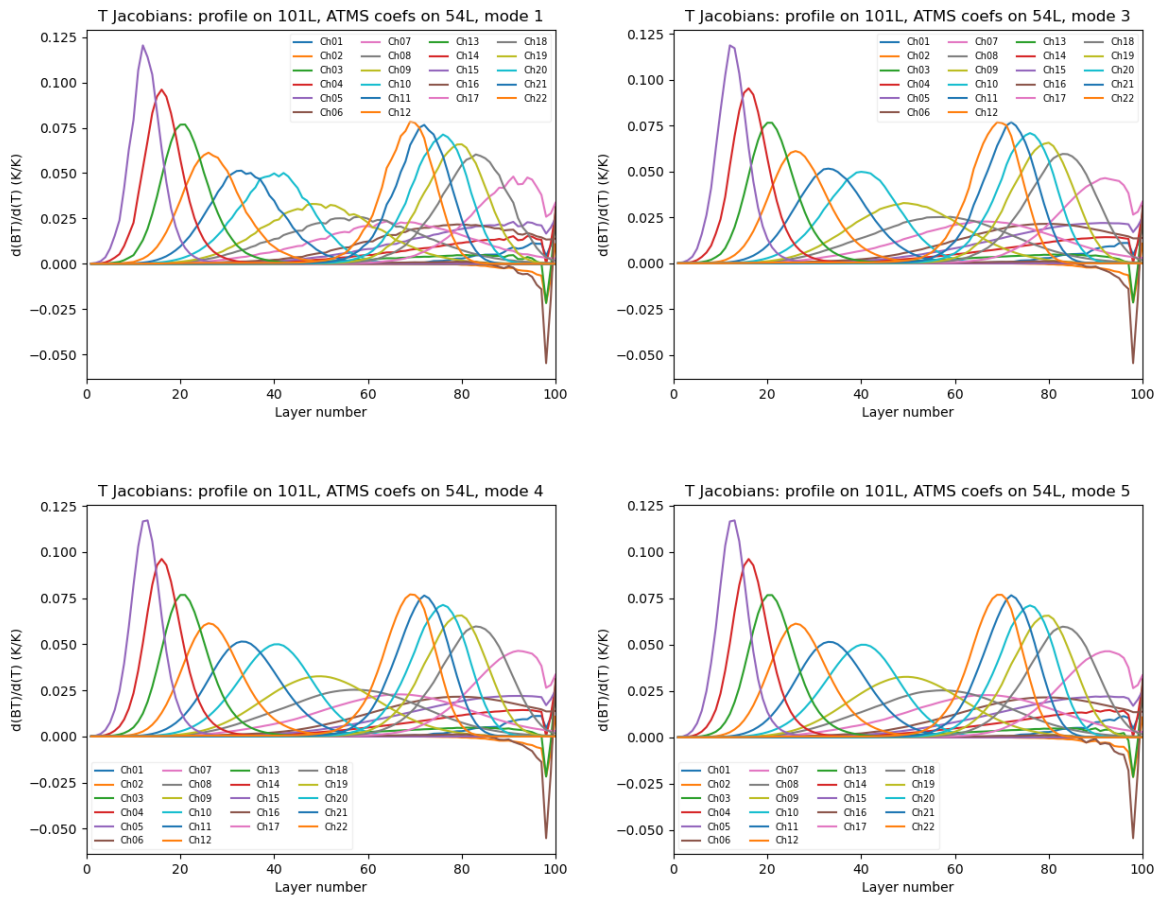


Figure 2.1.5: temperature Jacobians for ATMS channels for an input profile on 101L and coefficients on 54L. Plots are shown for interpolation modes 1, 3, 4, and 5.

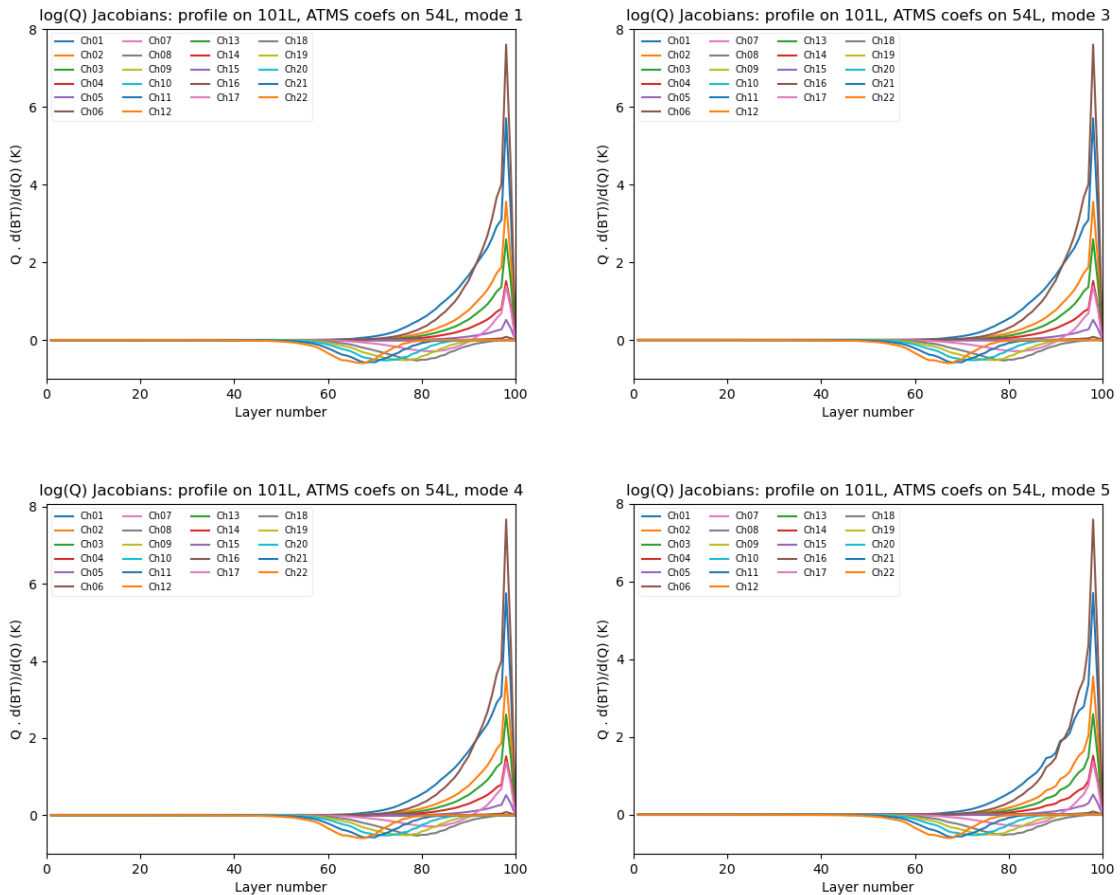


Figure 2.1.6: water vapour ($\log(Q)$) Jacobians for ATMS channels for an input profile on 101L and coefficients on 54L. Plots are shown for interpolation modes 1, 3, 4, and 5.

Figures 2.1.7 and 2.1.8 show the same for “case 2” where the input profile is on 44 levels and the coefficients are on 101 levels. Modes 1, 3 and 4 give very similar Jacobians with only small differences between them. The mode 5 temperature Jacobians again exhibit some artefacts near the surface, and the water vapour Jacobians clearly show oscillations.

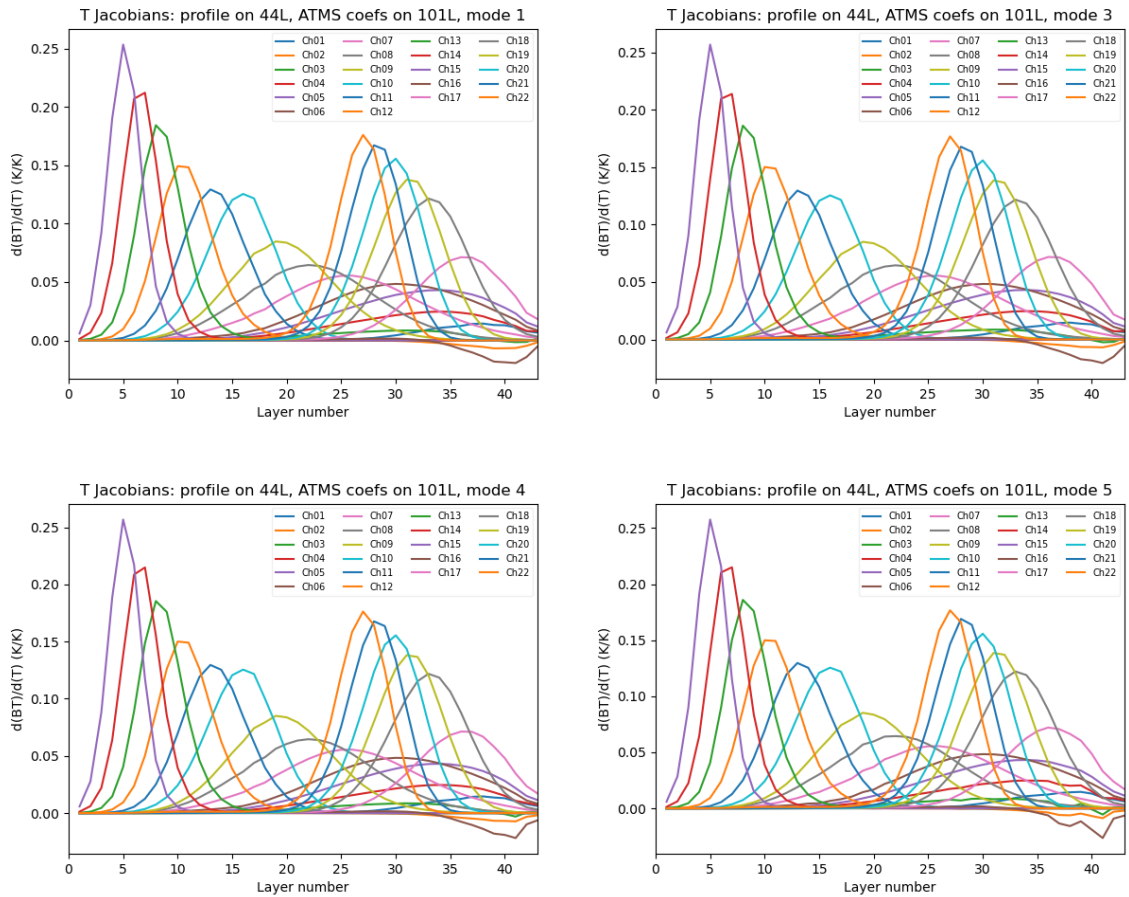


Figure 2.1.7: temperature Jacobians for ATMS channels for an input profile on 44L and coefficients on 101L. Plots are shown for interpolation modes 1, 3, 4, and 5.

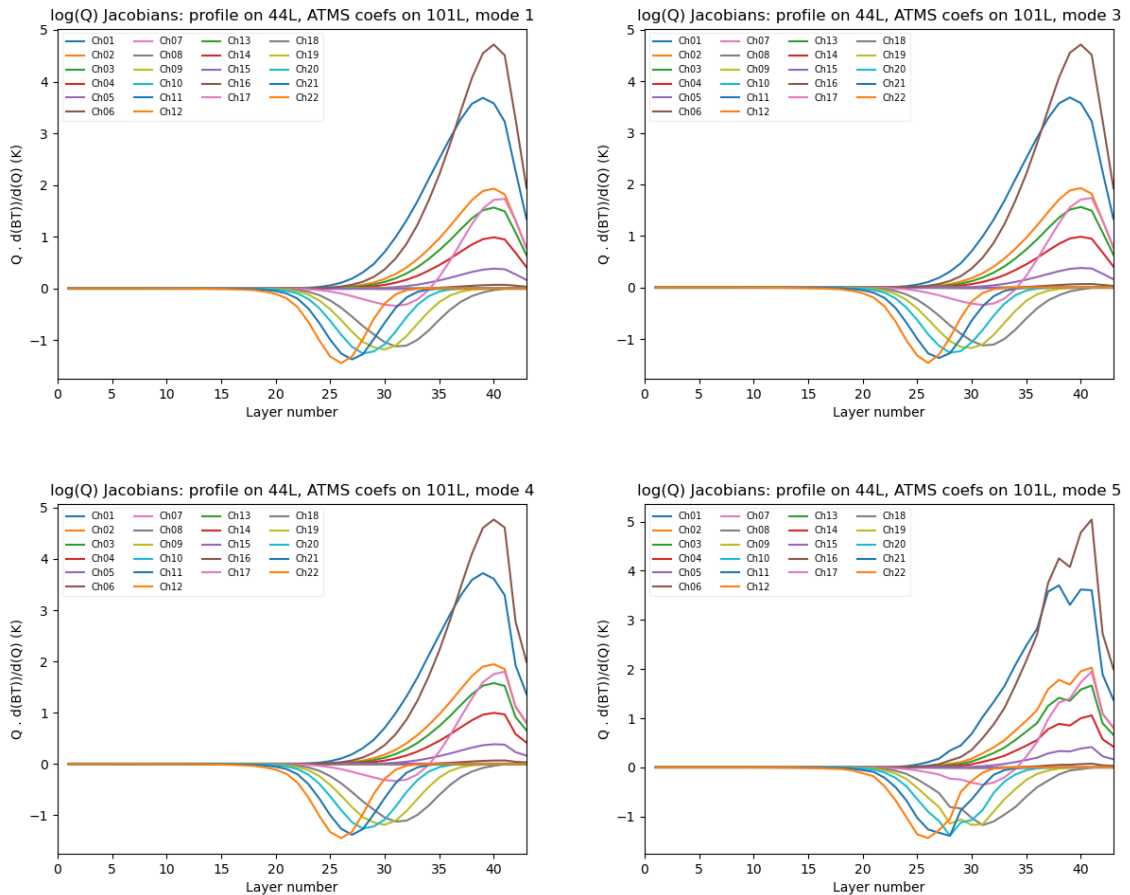


Figure 2.1.8: water vapour ($\log(Q)$) Jacobians for ATMS channels for an input profile on 44L and coefficients on 101L. Plots are shown for interpolation modes 1, 3, 4, and 5.

The conclusions here are similar to H14. Overall mode 4 gives the smoothest Jacobians. Mode 5, while giving the smallest interpolation errors overall (as discussed in [section 2.1.2](#)) yields Jacobians with oscillations or jaggedness. This is not necessarily a problem for retrieval applications as noted in H14 as the vertical correlations tend to smooth out the effects of such oscillations.

For RTTOV v14.0, mode 4 is the default, and modes 4 and 5 are recommended over modes 1, 2 and 3.

2.2 Updates to microwave coefficients

2.2.1 Microwave spectroscopy

Since the release of RTTOV v13, AMSUTRAN line-by-line calculations for instruments containing channels in the sub-millimetre range (frequencies beyond 200 GHz) have made use of updated spectroscopic data for water vapour and ozone, as suggested by Turner and Saunders (2019a) and Turner *et al* (2022). These datasets contain a greater number of lines for both gases and are necessary to accurately model the sub-millimetre region as the existing spectroscopic datasets used (as described in Turner *et al*, 2019b) do not contain a sufficient frequency range to accurately model channels operating at frequencies beyond 200 GHz. In this approach treatment of the mixed gases (oxygen, nitrogen) are unchanged from Turner *et al* (2019b).

For the microwave coefficients created for the RTTOV v14 release the approach for the sub-millimetre has been applied to all instruments, including those without submillimetre channels, for consistency. Table 2.2.1 compares the details of the new spectroscopic data with the previous configuration. Before the present update only the 35 most intense ozone lines below 300 GHz were included.

Gas	Number of lines	Source	Version	Previous number	Previous source
Ozone	1242	HITRAN	2020	35 < 300 GHz	HITRAN 2000
Water Vapour	366	AER	3.8	30	MPM89*
Water Vapour continuum	-	MT-CKD	4.2	-	MPM89

Table 2.2.1 The sources of the spectroscopic databases for ozone and water vapour lines and the continuum model for water vapour. The last two columns show the previous configuration for microwave coefficients (*with modifications to air broadening parameters for the 22 and 183 GHz lines, see R12REP2017).

An example of the resulting change in the simulated brightness temperatures for an existing microwave instrument, in this case ATMS, is shown in Figure 2.2.1. The largest change is 0.2 ± 0.1 K and is present at the highest frequency with the most sensitivity to the 183.31 GHz water vapour line, as might be expected. The main temperature sounding set of frequencies (channels 5-15) are unaffected.

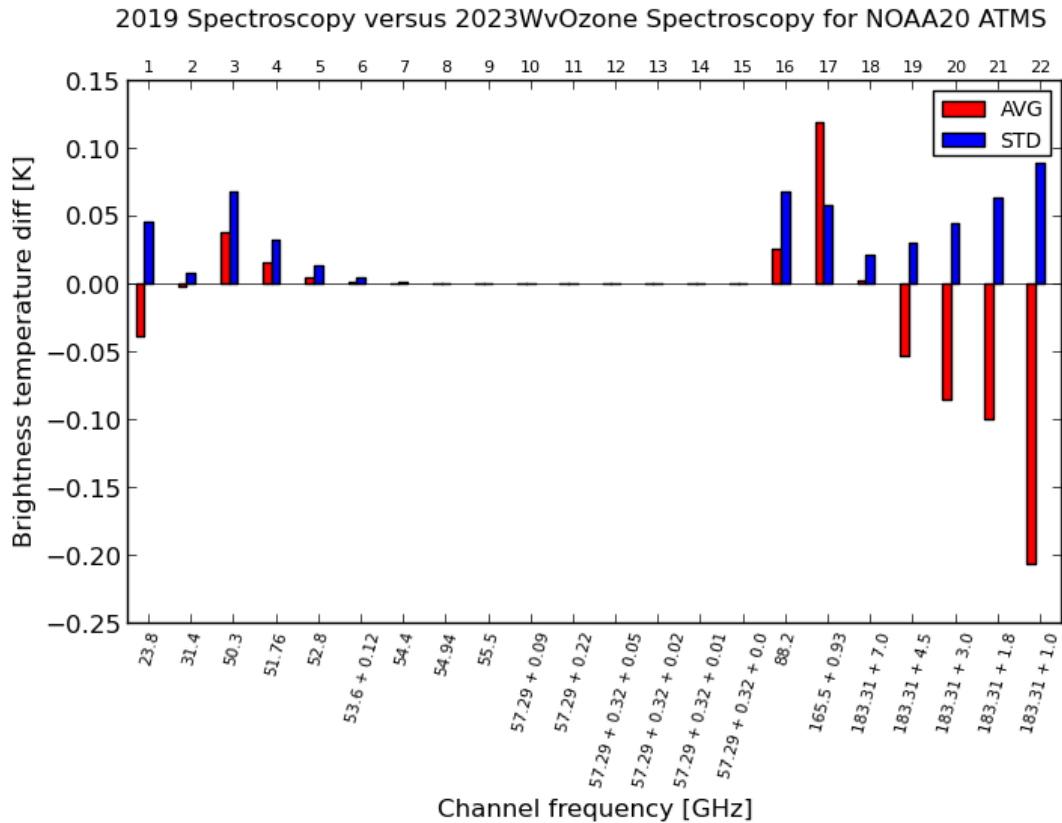


Figure 2.2.1: The mean and standard deviation of the difference between AMSUTRAN TOA brightness temperatures for runs with original spectroscopy and the updated water vapour and ozone spectroscopy. Simulations are for the set of 83 diverse profiles used for training RTTOV optical depth coefficients.

The performance of the RTTOV 14 coefficients with updated spectroscopy implemented within the ECMWF Integrated Forecast System (IFS) CY49R1 is shown in Figure 2.2.2, for five different instrument types. The normalised change in background standard deviation after bias correction is either reduced or neutral in the cases of GMI, CrIS, geostationary instruments, and conventional water vapour measurements. There are increases in some channels of ATMS and AMSU-A (left panel of Figure 2.2.3). However, the degradation is variable depending on the individual instrument, for example the fit is much worse for AMSU-A on NOAA-19 (right panel of Figure 2.2.3) than it is for AMSU-A on MetOp-B (centre panel of Figure 2.2.3).

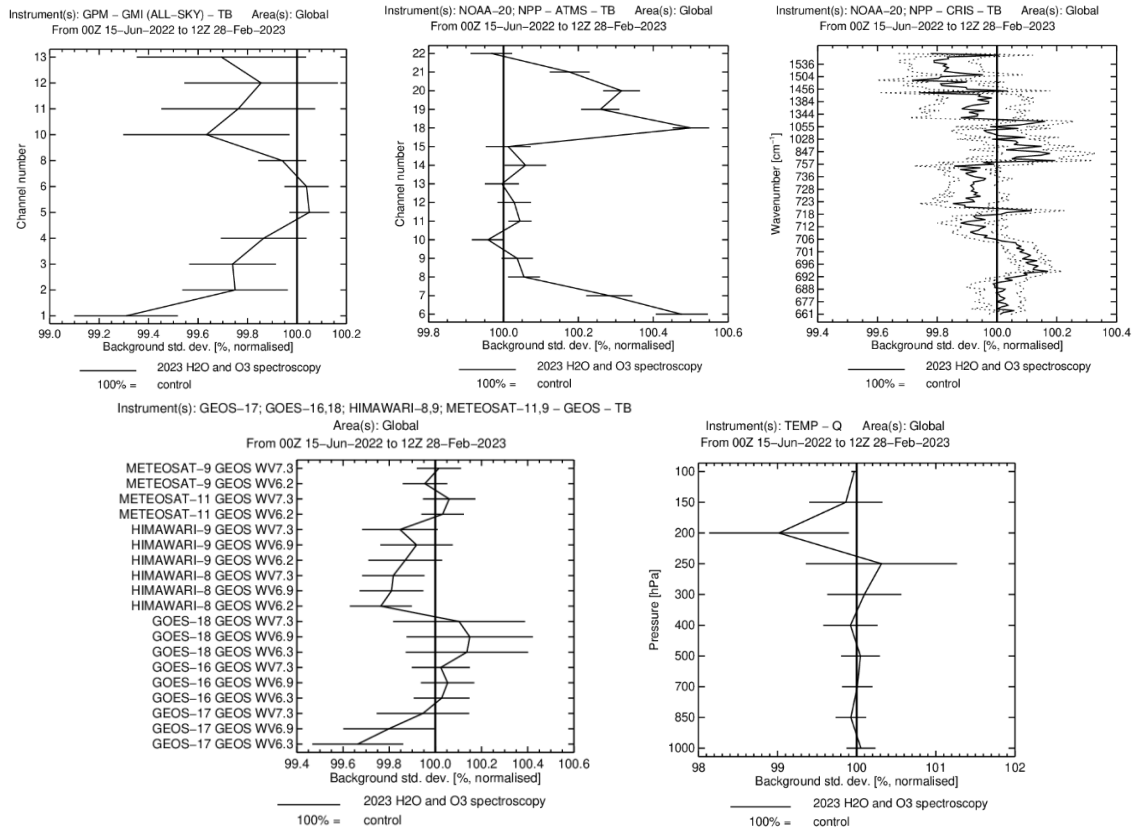


Figure 2.2.2: The effect of the new spectroscopy in RTTOV 14 coefficients on the standard deviation of global bias corrected background in combined summer 2022 and winter 22/23 experiments from the ECMWF model IFS-CY49R1. The panels show GMI, ATMS and CrIS (the latter two are composite of Suomi-NPP and NOAA-20 satellite platforms), geostationary, and conventional water vapour observing types.

The performance of the new microwave coefficients has also been tested in the Met Office NWP system (OS46 configuration which uses RTTOV v12.3). There is evidence that the fits of the 183 GHz channels have improved (e.g., Figure 2.2.4) as expressed by the change in standard deviation of less than 100%. For the lower frequencies there appears to be a mixed response (Figure 2.2.5). For instance, channel 5 (23.8 GHz, sensitive to the total water vapour column) shows an improvement. Overall, the impact for existing operational instruments such as GMI, but also ATOVS and ATMS, are considered neutral within the Met Office scheme.

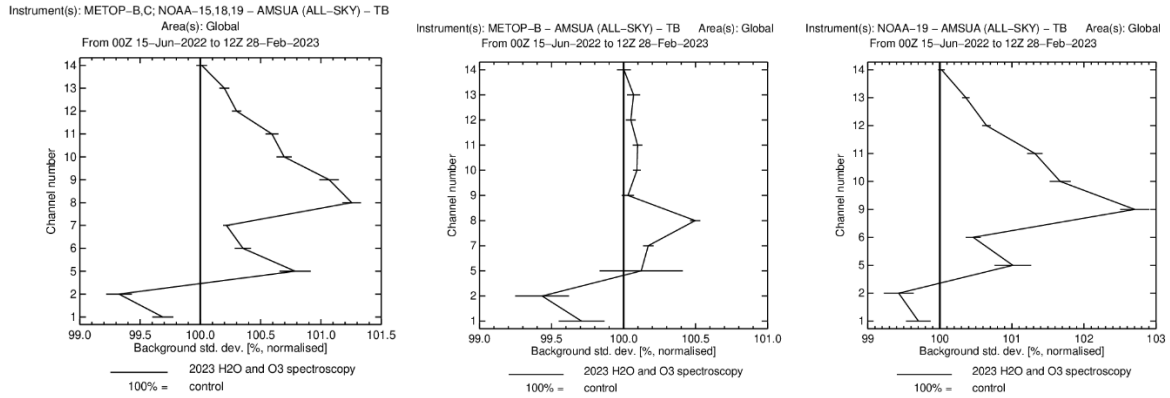


Figure 2.2.3: Same as Figure 2.2.2 but for: left panel: AMSU-A composite of five platforms (NOAA-15,18 and 19 and MetOp-B and C), centre panel: AMSU-A on MetOp-B and, right panel: AMSU-A on NOAA-19

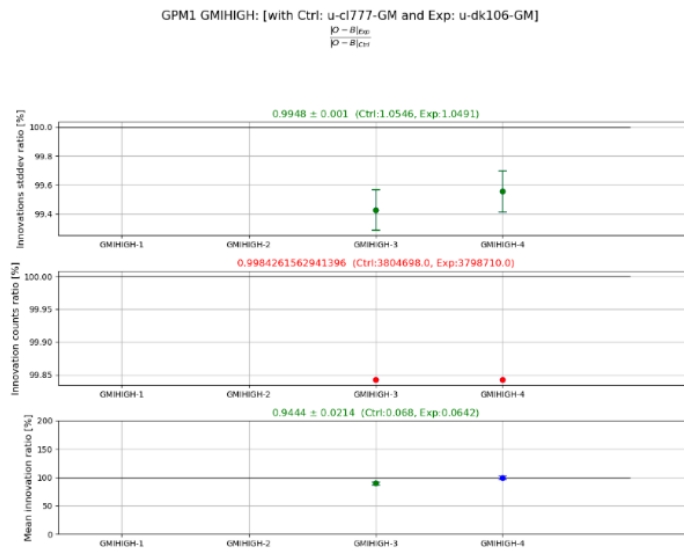


Figure 2.2.4: The effect of the new coefficients on the change in Corrected-Background difference for GMI High Frequency channels 3 (183.31 ± 7) and 4 (183.31 ± 3 GHz) in a Met Office NWP experiment. Top panel: change in standard deviation, mid panel, change in counts, bottom panel, change in mean difference.

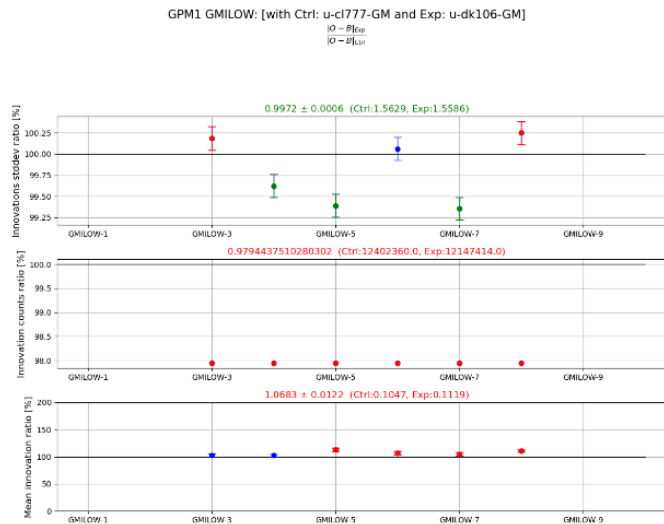


Figure 2.2.5: The effect of the new coefficients on the change in Corrected-Background difference for GMI low frequency channels 3-8 operating at 18.7V, 18.7H, 23.8V, 36.5V, 36.5H and 89V GHz in a Met Office NWP experiment. Top panel: change in standard deviation, mid panel, change in counts, bottom panel, change in mean difference.

2.2.2 Variable ozone for microwave sensors

Within the sub-millimetre frequency range, for instruments such as ICI and AWS, the greater sensitivity of the observations to ozone necessitates treating ozone as a variable gas, rather than including it with the mixed gases which can be a tolerable assumption for lower frequency channels. A variable gas is one that uses its own RTTOV predictors, in this case the RTTOV v13 ozone predictors, rather than being included with the mixed gases. At sub-millimetre frequencies RTTOV cannot adequately represent the increased amount of ozone absorption with the mixed gas predictors, resulting in biases of up to 1.5 K at 664 GHz for the ICI instrument (Turner and Saunders 2019a, Figure 29). It has recently been found by some users that treating ozone as a variable gas for the lower frequencies can have a non-negligible effect and can be beneficial. For example, Figure 2.2.6 shows that the effect of allowing ozone to vary can change the simulated values of ATMS channels by up to 0.2 K, with a strong spatial gradient in the Southern Ocean. Consequently, the new coefficients released with RTTOV v14 treat ozone as a variable gas for all microwave instruments (although users always have the option to use the reference profile, which is the default if no suitable source of ozone is available).

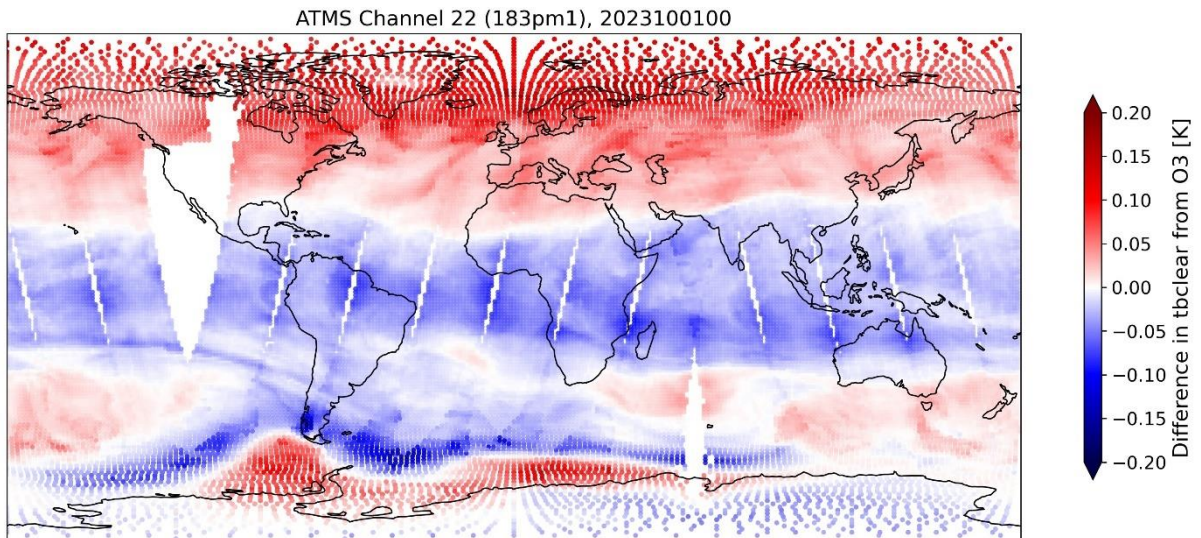


Figure 2.2.6: The impact on ATMS channel 183 +/- 1 GHz by treating ozone as a variable gas rather than a fixed profile. Source: ECMWF (David Duncan)

2.3 Zeeman coefficients based on v13 predictors

Zeeman coefficients for SSMI/S channels 19-22 and AMSU-A channel 14 were first released with the RTTOV v10 package and for non-Zeeman affected channels and levels were based on the v7 predictors (R10REP2010). New coefficients have been created based on the v13 predictors, and additionally extended to ATMS channel 15, which is nominally identical to AMSU-A channel 14.

Apart from the upgrade from v7 to v13 predictors there have been further developments to the scientific basis for modelling the Zeeman splitting in the line-by-line code, AMSUTRAN. The new model (called Zeeman2) uses improved parameters derived by Larsson *et al* (2019, Table 2). Larsson adopts a more recent model of rotational fine-structure states for molecular oxygen rather than using the Hund case (b) assumption, which is what the previous coefficient was based on and has known flaws (Rosenkranz *et al*, 1988). Larsson calculates so-called 'g-factors', which scale the magnetic field for each state. Zeeman2 incorporates 37 hyperfine spectral oxygen lines (an increase of 3 from the former version) with line parameters taken from Tretyakov *et al* (2005, Table 5), whereas the previous implementation used parameters from HITRAN 1996 (Rothman *et al*, 1998). This update also has the benefit of making the line parameters consistent with the non-Zeeman channels, as Tretyakov *et al* (2005) is currently the standard configuration for all oxygen lines in AMSUTRAN. The parameters used in the complex line shape approximation are also updated to increase accuracy (Rosenkranz, 2023).

The extended atmospheric profiles, which are necessary for training the high peaking SSMI/S channels, have been retained from the RTTOV 10 Zeeman coefficients. The Zeeman predictors, which are only applied to Zeeman channels and only on levels above a specified altitude, are unchanged from the previous implementation, originally produced by Han (2007). These coefficients can only be run in RTTOV 14 and not previous versions.

The following plots with Zeeman coefficients in this section were carried out using an adapted version of RTTOV v13 as the development work was done when RTTOV v14 was in an early stage of development. See Figure 2.3.7 at the end of this section for a comparison of Zeeman simulations in v13 vs v14.

Figure 2.3.1 shows global TOA brightness temperature differences in channels 19-22 of SSMI/S between updated Zeeman coefficient simulations and the equivalent from non-Zeeman coefficients. Zeeman affected brightness temperatures can deviate strongly, by up to 10 K relative to non-Zeeman (channel 20 over equatorial regions). Channel 22, however, shows only minor effects up to ~0.2 K because it peaks lower around 40 km and is hence only very lightly affected by the Earth's magnetic field. The general pattern of negative and positive differences is reversed between pairs of channels 19-20 and 21-22 because of the different predictors used. Channels 19 and 20, contain predictors that are inversely proportional to magnetic field (BFIELD), or $BFIELD^2$. As these channels have the peak of their weighting functions in the mesosphere where the temperature decreases with height the brightness temperature increases with the Zeeman effect (peak moves lower). The opposite is true for channels 21 and 22, which are in the upper stratosphere and hence predictors for these channels are directly proportional to BFIELD.

ATMS (or AMSU-A) is not strongly affected by the Zeeman effect in channel 15, as shown in Figure 2.3.2. Values are ~0.2 K in magnitude for most of the globe but differences can reach 0.5 K in southern high latitudes. Satellite zenith angle has little effect so only results for a zenith angle of 0° are shown.

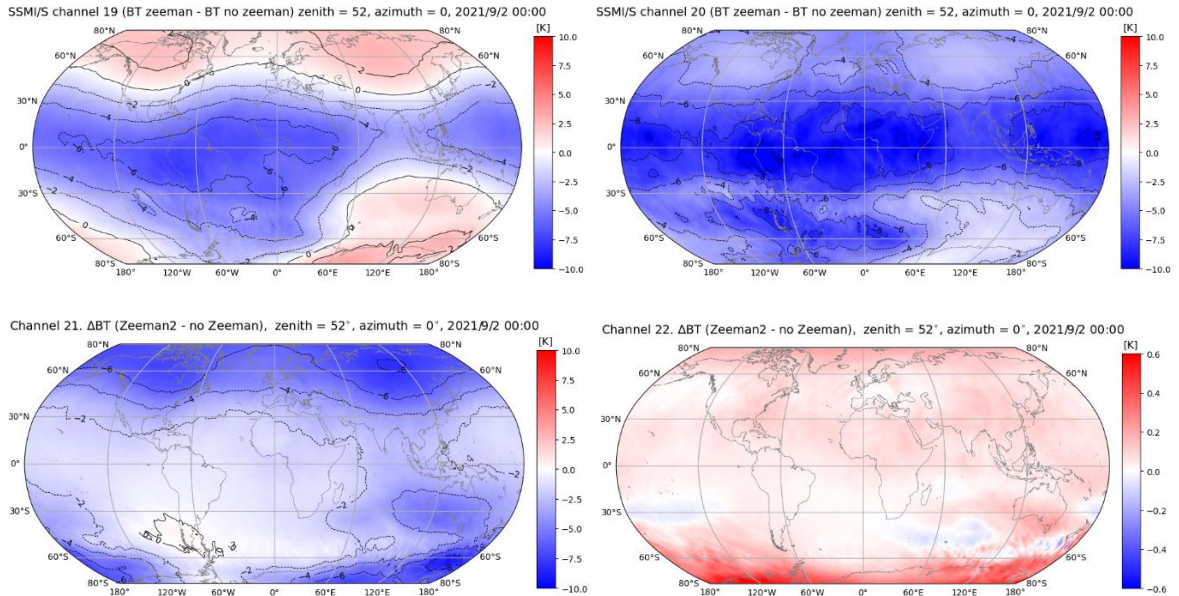


Figure 2.3.1. Brightness temperature differences between Zeeman and non-Zeeman simulations for channels 19-22 of SSMI/S, using the improved zeeman2 spectroscopy. Channel 22 uses a different contour scale. A satellite zenith angle of 52° is specified.

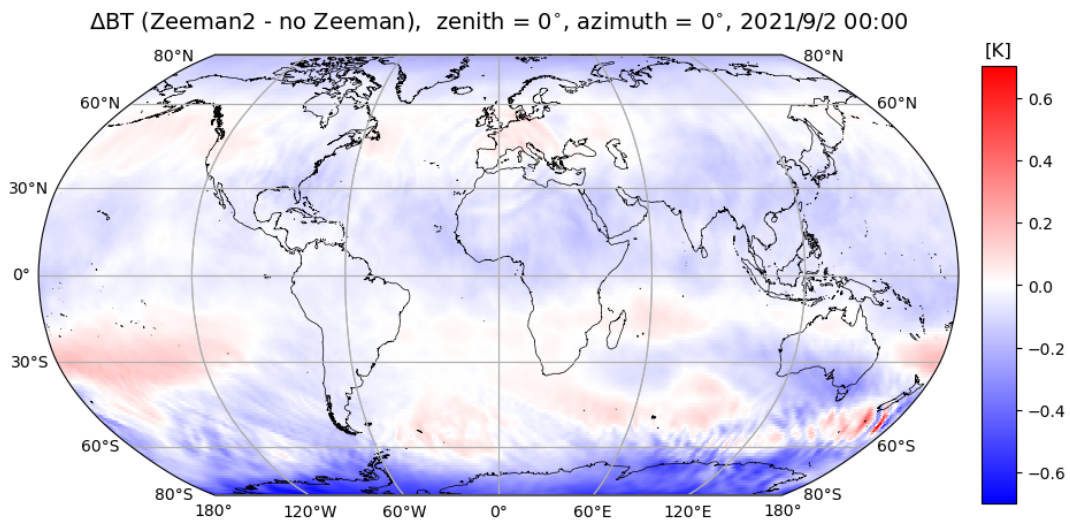


Figure 2.3.2. Brightness temperature differences between Zeeman and non-Zeeman simulations for channel 15 of ATMS, using the zeeman2 spectroscopy. A satellite zenith angle of 0° is specified.

2.3.1 Comparison with previous Zeeman coefficients

The following figures present RTTOV simulations of the Zeeman effect across the full range of valid values of BFIELD (0.2 to 0.7 G) and the cosine of the angle between BFIELD and satellite viewing angle, COSBK (-1.0 to 1.0), for the four Zeeman channels of SSMI/S. All calculations are performed with an independent dataset of 83 diverse profiles on 101 levels where the mean profile (83rd) is shown in red and the remaining 82 are shown in grey.

The differences between the new and old (RTTOV 10) Zeeman coefficients are shown in Figure 2.3.3 for channels 19-22 of SSMI/S. They are mostly below 1 K and results are reasonably constant with changing BFIELD apart from channel 20 at low BFIELD values, suggesting most differences are probably due to other interim changes between the versions of RTTOV. As channel 22 is sparsely affected by the Zeeman effect this suggests that there is a mean change of 0.5 K due to the difference between v7 and v13 water vapour predictors in this channel.

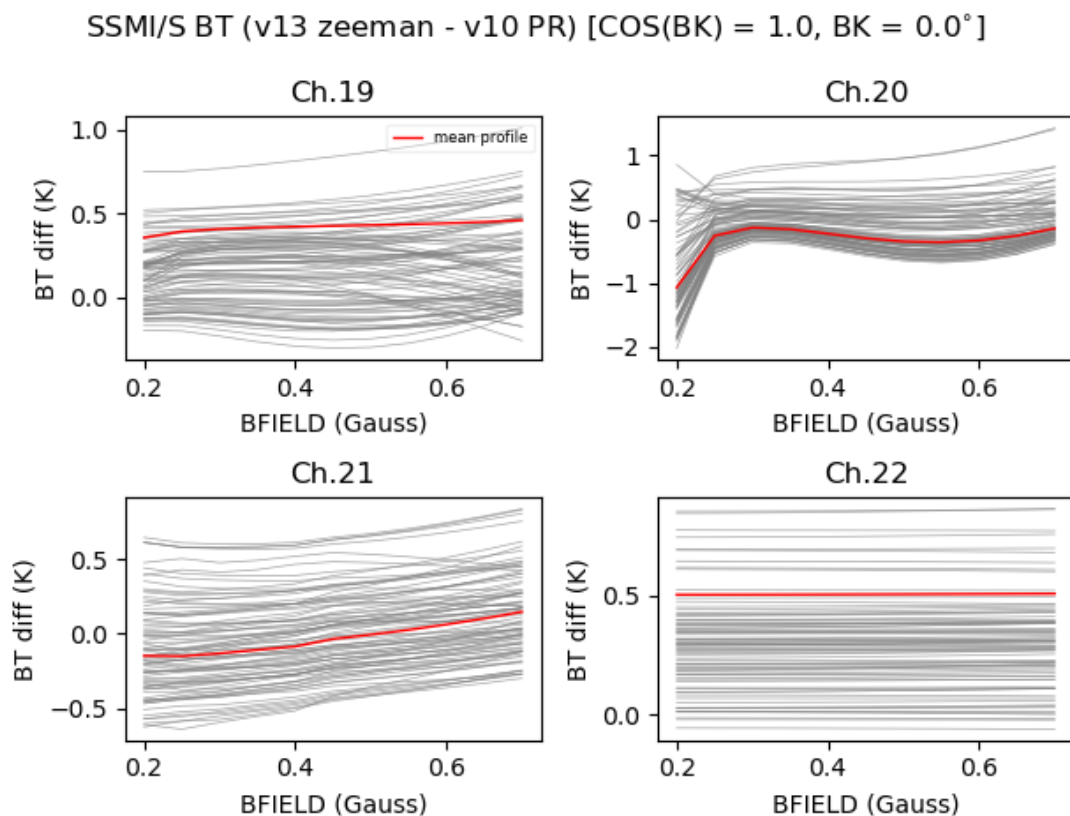


Figure 2.3.3. SSMI/S channel brightness temperature differences between RTTOV 13 and RTTOV 10 Zeeman coefficients, with variable magnetic field and fixed cosine of the angle between the magnetic field and satellite view.

See Figure 2.3.4. for the isolated effect of improving the spectroscopic configuration mentioned earlier. It is far less than the Zeeman effect itself, at or below 1 K, apart from channel 22 where this difference is equivalent to the magnitude of the Zeeman effect. There is little dependence on magnetic variable (none at all in channel 22), apart from the sharp change between 0.2 - 0.25 Gauss in channel 20, which is a feature of the Zeeman predictors.

SSMI/S BT (v13 zeeman - v13 zeeman2) [COS(BK) = 1.0, BK = 0.0°]

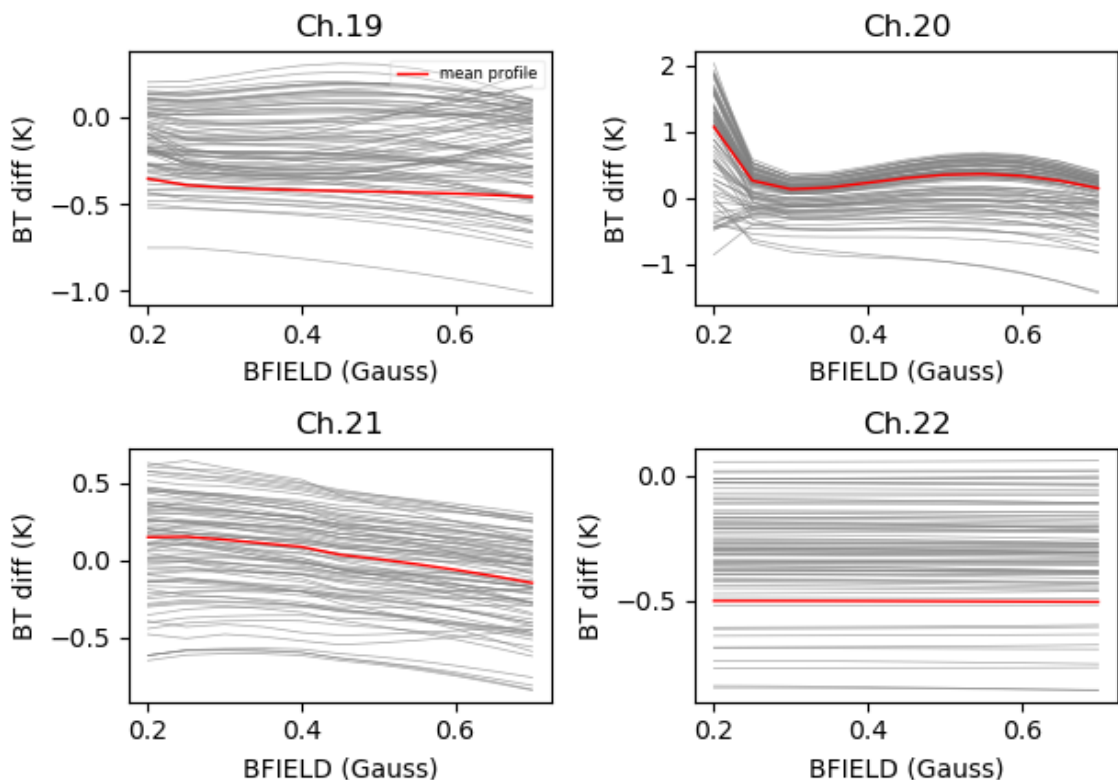


Figure 2.3.4. SSMI/S channel brightness temperature differences between RTTOV 13 and RTTOV 10 Zeeman coefficients, with variable magnetic field and fixed cosine of the angle between the magnetic field and satellite view.

2.3.2 Zeeman validation statistics

Figure 2.3.5 shows the validation statistics for the SSMI/S Zeeman coefficients. The biases between LBL and RTTOV are much larger than the typical non-Zeeman statistics due to the significant impact of the Zeeman effect. The largest values are in channel 20 where RMS differences are around 0.6 K, and absolute maximum differences reach 4 K. The values for

RMS look very similar to the equivalent results in Han *et al* (2007, Figure 7) giving confidence in the implementation.

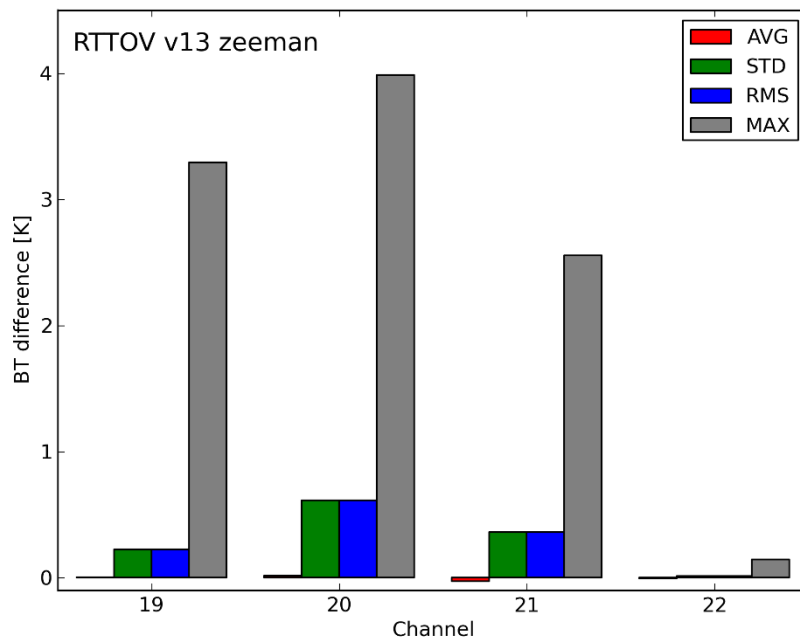


Figure 2.3.5. Validation statistics for four channels on SSMI/S including the Zeeman effect, for version 13 of RTTOV. The training dataset used is 52 profiles on 84 smoothed levels with three SSMI/S secants over 11 BFIELD and 11 COSBK values.

Figure 2.3.6 shows validation statistics for channel 15 of ATMS for a Zeeman coefficient and a non-Zeeman. The differences for the Zeeman simulation are increased around 4 or 5-fold over the non-Zeeman case but are still low overall.

As noted earlier, all plots in this section were generated with RTTOV v13. Figure 2.3.7 compares RTTOV v14 with v13 for the new SSMI/S Zeeman coefficients based on v13 predictors for the 5000 temperature-sampled subset of the 137L NWP SAF profile dataset (Eresmaa and McNally, 2014 & 2016). The BFIELD and COSBK values are varied among the profiles through their respective ranges of valid values. The standard deviations of the differences in each channel are much smaller than the typical magnitude of the Zeeman effect itself, and for channels 19, 20, and 21, they are smaller than the errors in the fit to the LBL training simulations (Figure 2.3.5).

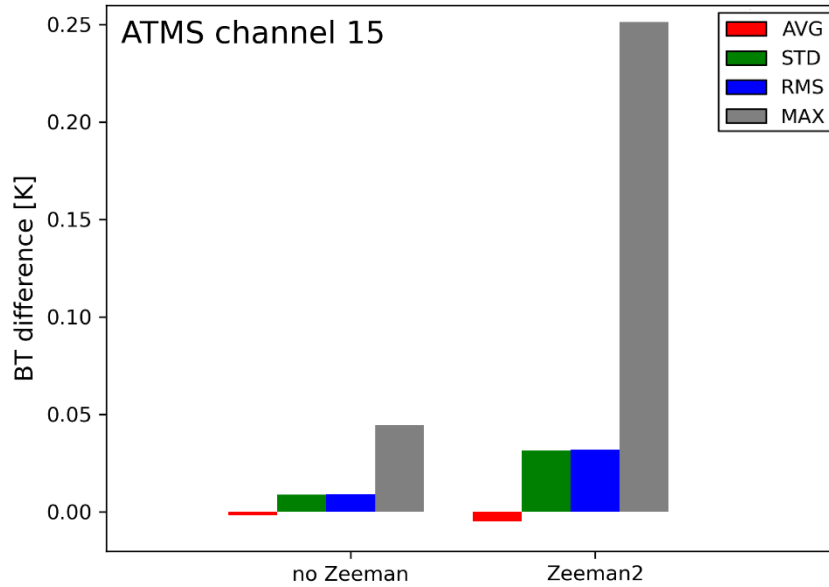


Figure 2.3.6. Validation statistics for ATMS channel 15 using RTTOV v13 for a non-Zeeman and a Zeeman simulation where the latter is using zeeman2 spectroscopy. The dataset is an independent set of 83 profiles on 101 levels.

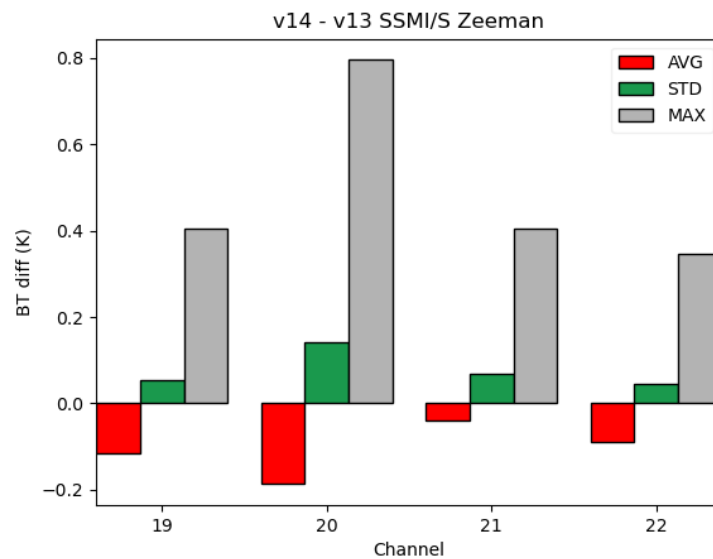


Figure 2.3.7: statistics of RTTOV v14 minus v13 brightness temperatures for clear-sky SSMI/S Zeeman channel simulations for the 5000 temperature-sampled subset of the 137L profile dataset with varying BFIELD and COSBK values.

2.4 UV simulations

The extension to the UV part of the electromagnetic spectrum was introduced in RTTOV v13.1. This extension was implemented and tested in the framework of the NWP SAF visiting scientist program with KNMI scientists involved in trace gas and aerosol retrievals in the AC SAF using satellite observations from UV/VIS/NIR spectrometers from GOME-2 onboard METOP satellites. In this work, an evaluation of RTTOV UV capabilities was done by comparing RTTOV simulations from clear-sky and aerosol-contaminated scenes with the radiative transfer model DISAMAR of KNMI (Wang and Tuinder, 2022).

The calculation of the coefficients is based on the line-by-line model LBLRTM version 12.8 currently used for VIS/NIR and IR. Figure 2.4.1 shows the total transmittance for profile 83 (the mean of the set of profiles used for training RTTOV coefficients) calculated between 1000 and 42000 cm^{-1} at 0.1 cm^{-1} resolution that is the chosen spectral resolution before SRF convolution. The strong ozone absorption band below 300 nm is well represented by LBLRTM.

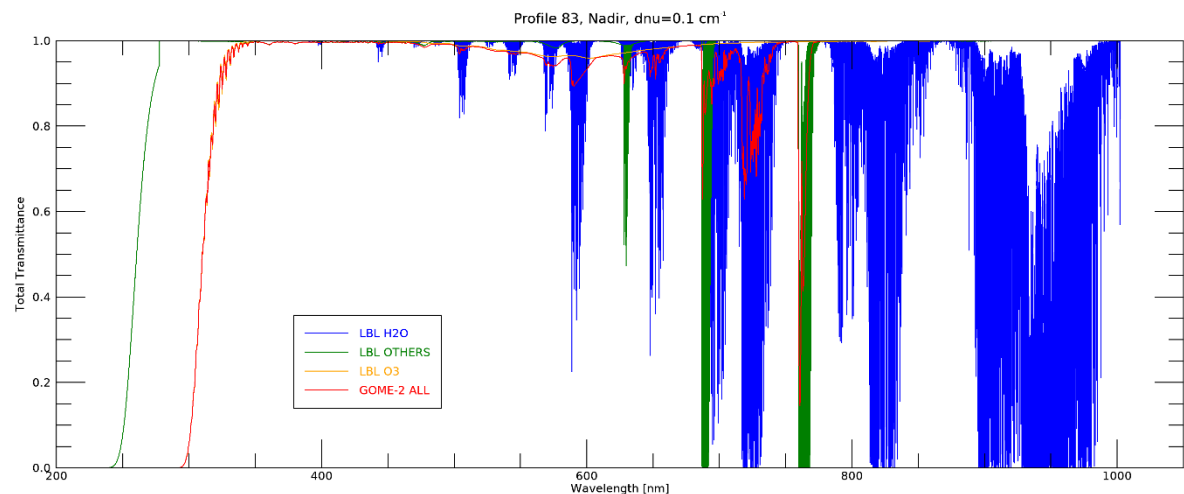


Figure 2.4.1: Transmittance from LBLRTM between 238 nm and 1000 nm (or 42000 cm^{-1} and 1000 cm^{-1} at 0.1 cm^{-1} spectral resolution) for water vapour (in blue), ozone (in orange) and other molecules (in green). In red line is represented the convolved total transmittance for GOME-2.

This resolution has been chosen to have sufficient spectral points for the SRF convolution and to keep the LBL transmittance database size manageable. Figure 2.4.2 shows GOME-2 SRFs for a few channels chosen between the first channel at 241 nm ($\sim 41483 \text{ cm}^{-1}$) and the last channel at 775 nm ($\sim 12890 \text{ cm}^{-1}$). The width of the SRF in wavenumber space decreases as the central wavenumber decreases and is around 60 cm^{-1} for the first channel to 20 cm^{-1} for the last channel, equivalent to 600 down to 200 spectral points for the convolution.

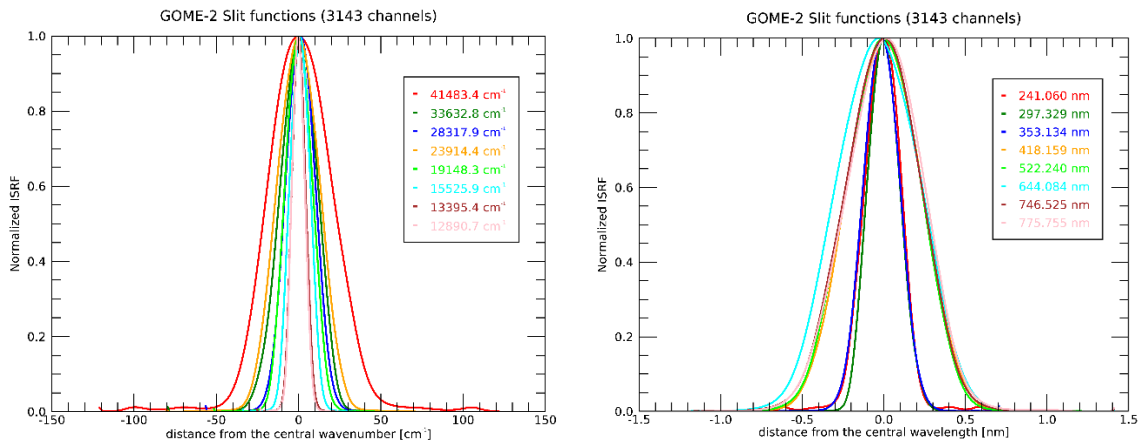


Figure 2.4.2: GOME-2 SRF (slit functions) for few channels along the GOME-2 spectral range 240-775 nm in wavenumber space (left) and in wavelength space (right).

The validation of the GOME-2 coefficient against LBLRTM is shown in Figure 2.4.3 where the statistical difference in reflectance is plotted for the mean spectral bias (in red), the standard deviation of the bias (in blue) and the maximum of the bias (in grey). The statistics were calculated for the 83 profiles used for training RTTOV coefficients with coefficients on 101L based on v13 predictors with variable O₃. The simulations are run for a range of satellite and solar zenith angles with a relative azimuth of 180 degrees. The simulations include contributions from atmospheric Rayleigh scattering and surface reflection assuming a surface BRDF of 0.3/π located at the bottom level of the coefficient pressure profile.

Figure 2.4.4 shows the difference in simulated GOME-2 clear-sky spectra between RTTOV and DISAMAR for two scenes, one with a surface spectral albedo of 0 (a) and one with a surface spectral albedo of 0.8 (b). This plot is taken from Wang and Tuinder (2022) and as such is based on RTTOV v13. See [section 3.1.3](#) for comparisons between RTTOV v13 and v14 for GOME-2. For the dark surface, the simulated spectra are dominated by Rayleigh scattering where we can see that the RTTOV model (R13REP2020) that has been extended to the UV is slightly biased compared to DISAMAR (> 0.3% in relative difference). This difference was at least partially ascribed to RTTOV not accounting for depolarisation in the treatment of Rayleigh scattering which was subsequently remedied (see [section 2.5](#)). We can also see differences due to different spectroscopy between the models, for ozone (below 350 nm) and for water vapour (above 580 nm). Interestingly we found large biases in the O₂-A band at 760 nm even though the O₂ spectroscopy is the same.

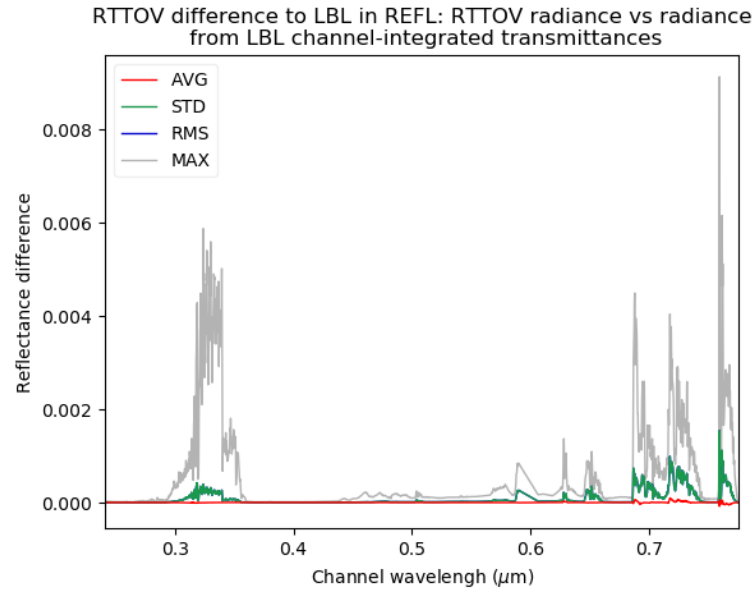


Figure 2.4.3: Validation statistics for the GOME-2 RTTOV coefficients on 101L based on v13 predictors with variable O_3 only.

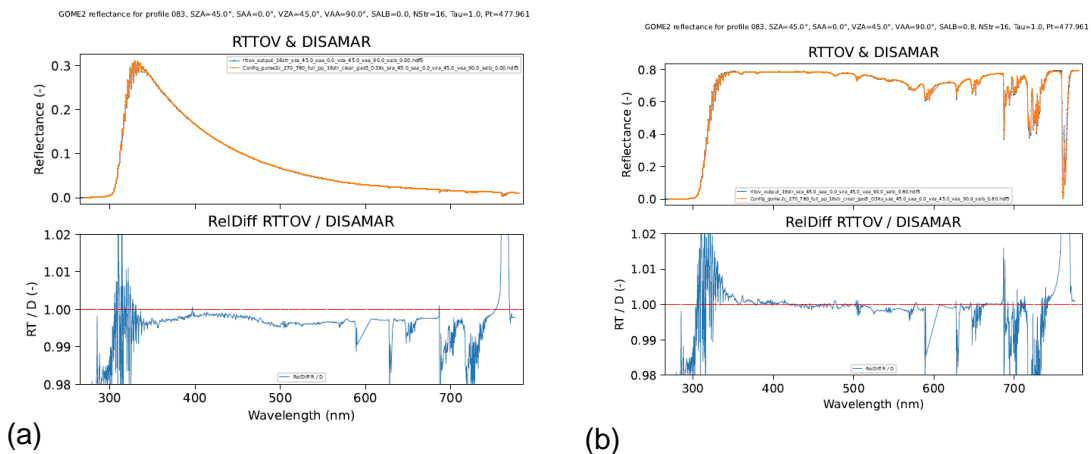


Figure 2.4.4: Comparison between GOME-2 simulated spectra from RTTOV and DISAMAR for a dark surface (a) and for a bright surface (b).

The scattering properties of aerosol and cloud have been extended to the UV and a first test for a simple aerosol case is shown in Wang and Tuinder (2022) with a good agreement. It should be mentioned that however, the current BRDF atlas does not cover the UV part as it starts at 400 nm. It is planned to update this in a future RTTOV release.

2.5 Rayleigh scattering depolarisation

As described in [section 2.4](#), an intercomparison of RTTOV with the DISAMAR radiative transfer model for UV simulations was carried out (Wang and Tuinder, 2022), and one recommendation from it was that RTTOV should account for the effect of depolarisation in Rayleigh scattering.

RTTOV had previously represented the Rayleigh scattering phase function as:

$$P_{\text{ray}}(\theta) = \frac{3}{4}(1 + \cos^2 \theta)$$

where θ is the scattering angle. However, as discussed in Bucholtz (1995), molecular anisotropy affects the scattering distribution, and a more accurate formulation of the phase function is given by:

$$P_{\text{ray}}(\theta) = \frac{3}{4(1 + 2\gamma)} [(1 + 3\gamma) + (1 - \gamma) \cos^2 \theta]$$

where γ is a function of the wavelength-dependent depolarisation factor ρ_n :

$$\gamma = \frac{\rho_n}{2 - \rho_n}$$

Bucholtz (1995) tabulates values of γ for wavelengths in the range 0.2 – 1 μm . Within RTTOV, these tabulated values are linearly interpolated onto the channel central wavelengths for all solar-affected channels when the optical depth coefficient file is read in. For channels at wavelengths outside the given range, constant value extrapolation is applied. This is unlikely to have a significant effect at wavelengths above 1 μm as the impact of molecular Rayleigh scattering rapidly diminishes with increasing wavelength. RTTOV does not currently support channels at wavelengths below 0.2 μm . This more accurate formulation of the phase function is applied for both the Rayleigh single scattering parameterisation in RTTOV and the treatment of Rayleigh multiple scattering in the Discrete Ordinates Method solver (R13REP2020).

The use of this modified Rayleigh phase function was introduced on a switch in RTTOV v13.2, and in RTTOV 14.0 the switch was removed, and depolarisation is always taken into account. Figure 2.5.1 illustrates the impact of this change can be up to around 1% in simulated reflectance.

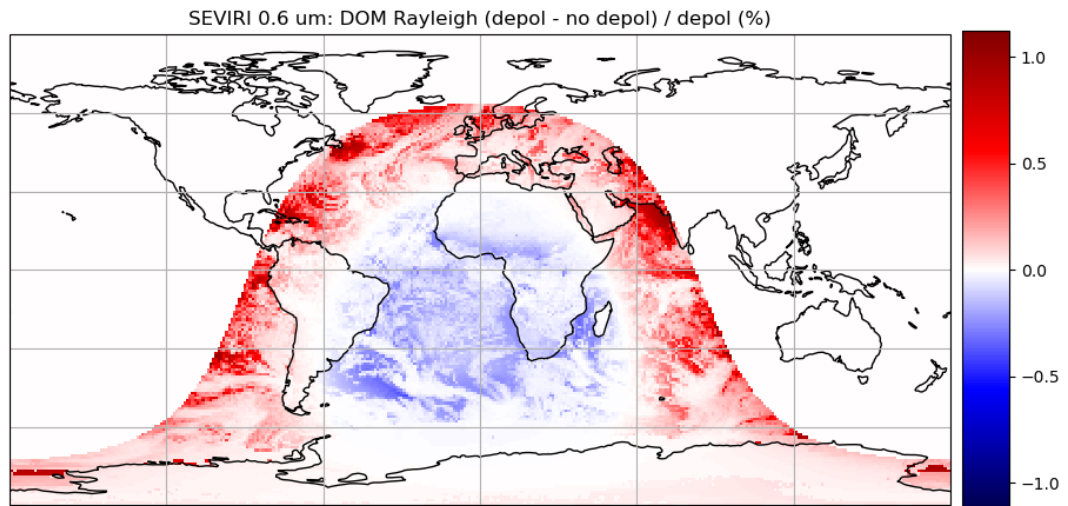


Figure 2.5.1: relative impact of Rayleigh depolarisation on simulated reflectances as a percentage of the reflectance with depolarisation using full multiple scattering simulations for an ECMWF analysis at 1200UTC on 01/12/2020.

2.6 RTTOV-SCATT science implemented in RTTOV

A key goal of RTTOV v14 is to enable all simulations through the core RTTOV interface, and to eliminate the separate RTTOV-SCATT interface/model for hydrometeor scattering simulations for microwave sensors. The science contained in RTTOV-SCATT at RTTOV v13.2 has been implemented into RTTOV as described in this section.

Further information on the historical development of RTTOV-SCATT including optical properties and cloud overlap treatment can be found in the RTTOV v8, v9, v10, v11 and v13 Science and Validation Reports. The optical properties supplied with RTTOV v14 remain the same as those provided for RTTOV v13, but the file format has changed so new files must be downloaded for use with v14.

2.6.1 Delta-Eddington solver

The delta-Eddington solver (Bauer *et al*, 2006) has been implemented in RTTOV v14 and is now an option for both infrared and microwave sensors. It has been generalised to work with any cloud overlap option so that, for example, it can be used with maximum/random overlap in the infrared.

In RTTOV-SCATT the clear-sky radiance is obtained from a call to RTTOV, while in RTTOV v14, the clear-sky radiance is computed by the delta-Eddington solver for consistency. The

difference between the “standard” RTTOV clear-sky and delta-Eddington clear-sky radiances is of order 0.01 K at most.

In RTTOV-SCATT, the gas absorption optical depths computed by a call to RTTOV are for the layers bound by the RTTOV pressure levels. RTTOV-SCATT interpolates these to obtain gas optical depths for the layers bound by the pressure half-levels. RTTOV v14 computes gas absorption optical depths for the layers bound by the pressure half-levels directly ([section 2.1](#)) so these are used directly by the delta-Eddington solver.

RTTOV-SCATT imposes an arbitrary restriction that at most one pressure half-level can be above 0.004985 hPa, and likewise for pressure full-levels. RTTOV v14 imposes no such restrictions.

The extension of the delta-Eddington solver to infrared instruments for both aerosol and hydrometeor scattering simulations is new in RTTOV. This required the calculation and storage of the asymmetry parameters in the aerosol and hydrometeor optical property files for infrared sensors, ingest and interpolation of these values within RTTOV, and extension of the delta-Eddington solver to general cloud overlap schemes as noted above.

Figure 2.6.1 compares nadir delta-Eddington and Chou-scaling radiances (the two fast solvers) to full multiple scattering DOM simulations (R12REP2017) with 8 streams for MTG-FCI IR channels. Hydrometeor simulations are run for the NWP SAF 25000 diverse profile set on 137 levels (Eresmaa and McNally, 2014 & 2016). Aerosol simulations are run for 20000 profiles from the NWP SAF 60 level MACC profile dataset (Eresmaa *et al*, 2012a&b) using the nine CAMS aerosol species for which optical properties are provided for RTTOV. The surface emissivity is set to 1 to avoid differences due to the differing surface assumptions in the DOM solver vs the fast solvers.

The mean and standard deviations compared to the reference DOM simulations are similar for delta-Eddington and Chou-scaling for both hydrometeors and aerosols. The maximum differences to DOM are larger for delta-Eddington in the hydrometeor case, but smaller for aerosols. Overall, the results indicate that the delta-Eddington solver is a reasonable alternative to the Chou-scaling solver in the IR.

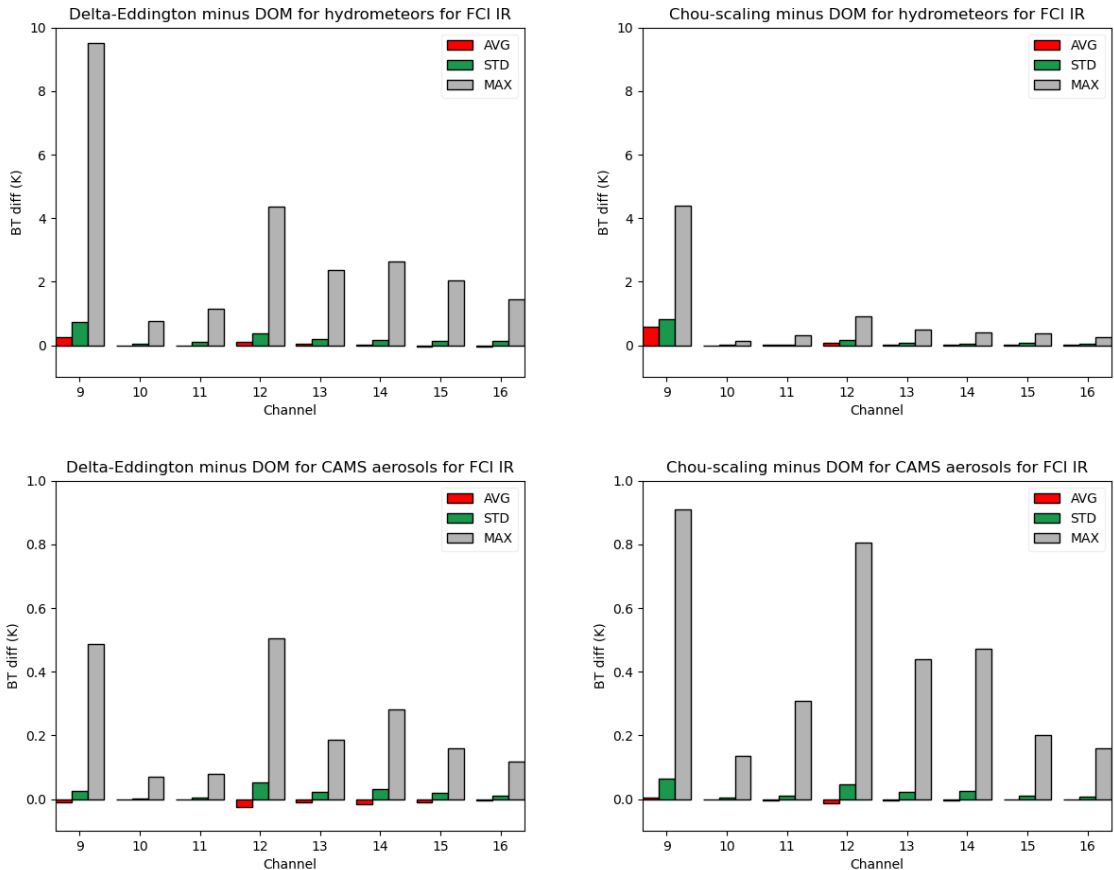


Figure 2.6.1: Statistics (mean, standard deviation, maximum absolute value) of delta-Eddington (left) and Chou-scaling (right) radiances minus DOM radiances (8 streams) with unit emissivity for the MTG FCI IR channels. All simulations are at nadir. The top panels show hydrometeor simulations based on the 25000 NWP SAF 137 level profile set, and the bottom panels show aerosol simulations based on 20000 profiles from the NWP SAF 60 level MACC profile set.

2.6.2 Cloud overlap options

The two-column hydrometeor-weighted cloud overlap calculation used in RTTOV-SCATT by default (Geer *et al*, 2009a,b) is available as an option in RTTOV v14 and is the default cloud overlap parameterisation for microwave sensors. Users can also choose to input a value for each profile effective cloud fraction explicitly in RTTOV v14 if they wish, as in RTTOV-SCATT.

The option to specify individual hydrometeor cloud fractions is now enabled via the `opts%cloud_overlap%per_hydro_frac` option. This works in RTTOV v14 in the same way as in RTTOV-SCATT. It is applicable only to the two-column hydrometeor-weighted cloud overlap parameterisation, and to the radar solver (see [section 2.6.3](#)).

The *hydro_frac_tlاد* option implemented in RTTOV-SCATT can be used to disable the hydrometeor sensitivity in the effective cloud fraction calculation in the TL/AD. This is available in RTTOV v14 and is applicable only to the two-column hydrometeor-weighted cloud overlap option.

2.6.3 Radar solver

The radar solver (R13REP2020) from RTTOV-SCATT has also been implemented in RTTOV v14 and is activated by setting the *opts%scatt%radar* option to true. Unlike in RTTOV-SCATT, the passive radiances are computed at the same time as the radar reflectivities in v14.

A validation of the radar simulator in v14 has been performed using the Météo-France ARPEGE (Action de Recherche Petite Echelle Grande Echelle) global NWP model for a case study located over the Atlantic Ocean on 2nd January 2021. This case study is further documented in Mangla *et al* (2025). Figure 2.6.2 compares the horizontal cross-section of GPM/DPR Ku band unattenuated reflectivity at three different heights (i.e., 2, 3.25 and 6 km from left to right) for the observations (top panels) and the simulations. Overall, the spatial structures of the simulated cloud are well matched with the observations. In addition, the simulations performed using v14 (bottom panels) are in very good agreement with the ones performed using v13.2 (middle panels) at all levels. It should be noted that this very good agreement was also obtained at Ka band, and also for the attenuated reflectivity (not shown here). One can observe that the reflectivity is overestimated within (at 3.25 km) and below the melting layer (at 2km), which is due to the fact that the bright-band is not simulated here. This overestimation of the Ku band reflectivities in the rainy levels is further documented in Mangla *et al* (2025).

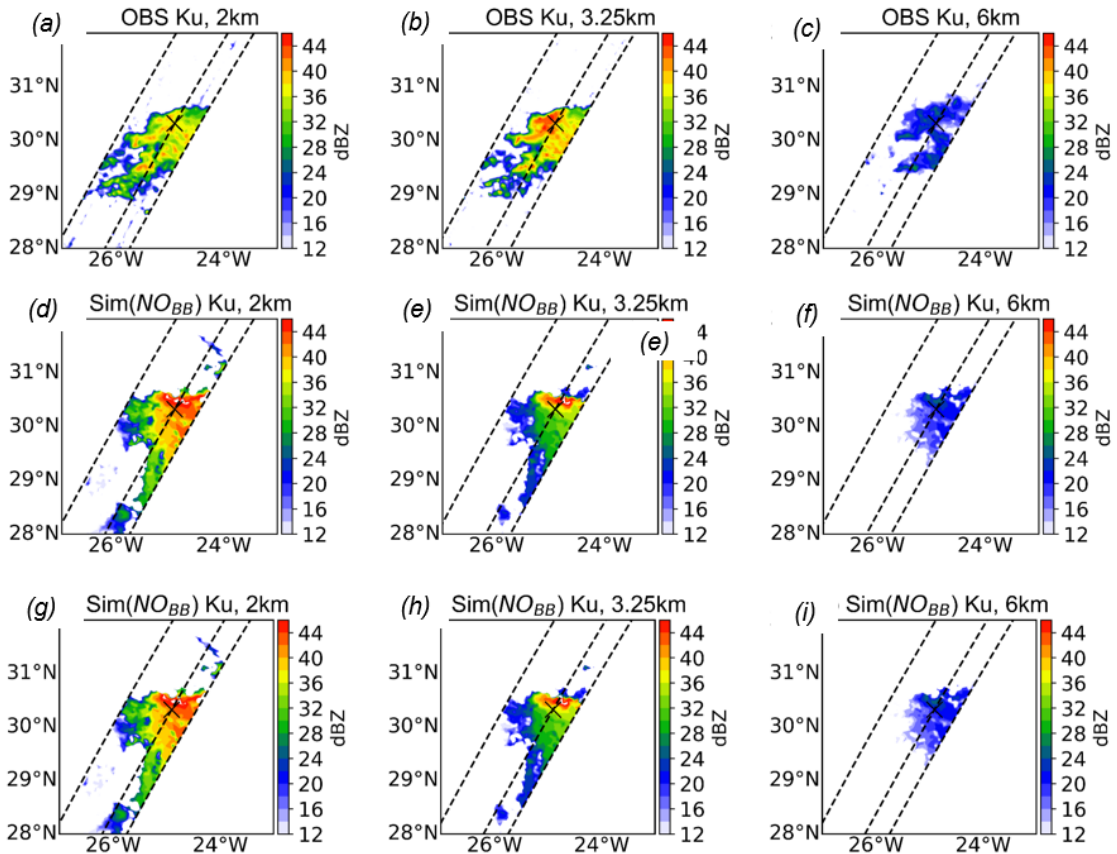


Figure 2.6.2: Horizontal cross-section at 2 km, 3.5 km and 6 km heights for Global Precipitation Measurement (GPM) DPR/Ku band reflectivities. The top panels (a-c) show the observations, (d-f) show the simulations with RTTOV-SCATT v13.2, (g-i) show the simulated reflectivities using RTTOV v14.

2.6.4 Other scattering options and calculations

RTTOV-SCATT assumes input hydrometeor concentrations are in units of kg/kg with respect to dry air. In RTTOV v14, if the profile *mmr_hydro* flag is true, then the input units are kg/kg with respect to moist air. This is consistent with the treatment of hydrometeors in the infrared and is also more consistent with NWP model cloud/hydrometeor fields.

RTTOV v14 continues to support rain and snow hydrometeor inputs in units of flux ($\text{kg}/\text{m}^2/\text{s}$) with no change to the unit conversion calculations. The user must set the *flux_conversion(:)* member of the profile structure appropriately for every individual profile in RTTOV v14.

The approximate treatments of polarisation implemented in RTTOV v13.0 (empirical, R13REP2020) and v13.2 (ARO-scaling, [section 2.12](#)) are both implemented in RTTOV v14 with no changes.

The *zero_hydro_tlad* option in RTTOV-SCATT enables or disables hydrometeor concentration TL/AD sensitivity in clear layers (i.e., layers with zero hydrometeor concentration). This is implemented in RTTOV v14 but can only be used for microwave sensors with any two-column cloud overlap parameterisation with the delta-Eddington solver. This also applies to the radar solver if enabled ([section 2.6.3](#)).

See [section 2.18](#) for the dynamic emissivity retrieval output that was previously only available from RTTOV-SCATT and has now been generalised in RTTOV v14.

2.7 Tang *et al* modification to Chou-scaling

The treatment of the multiple scattering in IR in RTTOV is based on the approach of Chou *et al* (1999). In this approach the effect of scattering by clouds and aerosols is parameterised by scaling the optical depth by a factor which depends on the backward scattering properties of the particles that compose the layer. The main hypothesis relies on the representation of the diffuse radiance as an isotropic function equal to the Planck function of the layer. With these assumptions, the solution of the radiative transfer equation is similar to the clear-sky solver where the scattering is included in the effective optical depth of the scattering layer, given by:

$$\tau_{eff} = \tau_{abs} + b\tau_{sca}$$

where τ_{abs} and τ_{sca} are the absorption and scattering optical depths respectively and b is the backscattering fraction given by:

$$b = \frac{1}{2} \int_0^1 d\mu \int_{-1}^0 \bar{P}(\mu, \mu') d\mu' = \frac{1}{2} \int_{-1}^0 d\mu \int_0^1 \bar{P}(\mu, \mu') d\mu'$$

where $\bar{P}(\mu, \mu')$ is the particle's azimuthally averaged phase function and μ, μ' are the cosine of the incident zenith angle and the cosine of the zenith angle which defines the direction of the diffuse field, respectively.

The study of Tang *et al* (2018) has shown that the approximation proposed by Chou *et al* can sometimes lead to large errors especially when the incident and scattered radiation occur in two different hemispheres. In that case the Planck function used to approximate the diffuse radiation field can be too large. In their study Tang *et al* proposed a correction to

the Chou *et al* approximation called the adjustment scheme. This error is particularly important in the far infrared (FIR) in presence of ice clouds.

In the frame of a Visiting Scientist from LOA (University of Lille), we implemented the adjustment scheme and tested the improvement of simulated spectra for the FORUM mission. Full details of the adjustment scheme are given in Labonnote *et al* (2022). In that study the adjustment scheme was implemented in RTTOV v13. It should be noted that although the mathematical formulation of the scheme in Labonnote *et al* is correct, there was an error in the implementation which affects the simulations shown in that report. The error was fixed in the RTTOV v14 implementation of the adjustment scheme.

Figure 2.7.1 shows the mean and standard deviation of RTTOV v14 brightness temperature differences between RTTOV-DOM (the Discrete Ordinates Method multiple scattering solver implemented in RTTOV, R12REP2017, using 16 streams) and different scattering approximations based on the Chou *et al* fast approximation. The simulations were performed over a 1370 profile subset of the 137L NWP SAF diverse profile dataset (Eresmaa and McNally, 2014 & 2016). This profile subset contains profiles that include only ice clouds. The cloud fraction was set to 1 in all layers containing cloud. The surface emissivity is set to 1 to eliminate differences due to the differing assumptions between solvers regarding surface reflectance.

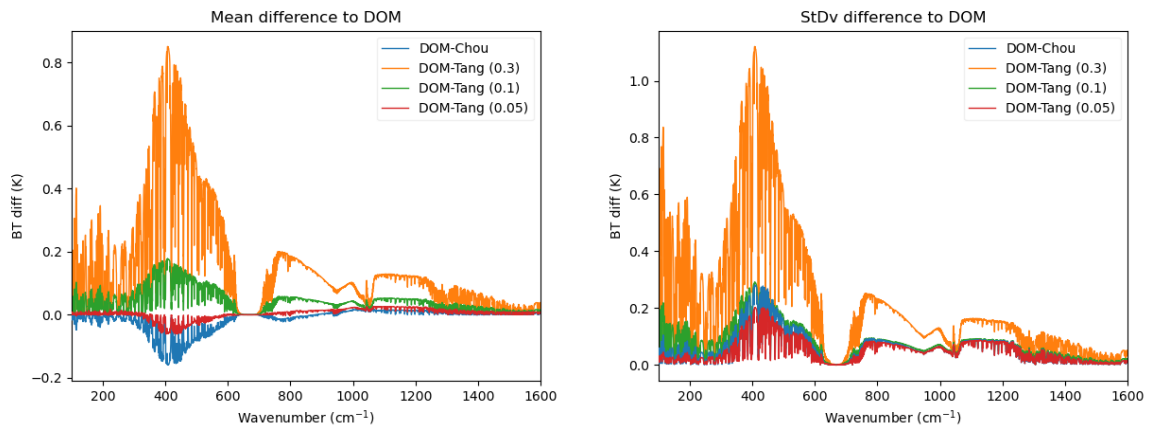


Figure 2.7.1: Mean and standard deviation of differences in FORUM brightness temperatures between RTTOV-DOM and fast scattering approximations.

The first scattering approximation is the Chou *et al* in blue where we can see that the bias increases in the FIR around 400 cm^{-1} as compared with the middle infrared (MIR). The second scattering approximation is the adjustment scheme with the adjustment factor of 0.3 proposed in Tang *et al*. We found that the proposed value of 0.3 is significantly worse than the Chou *et al* approximation. The Labonnote *et al* report recommended a value of 0.1 for the adjustment factor (shown in green), but in the corrected RTTOV v14 implementation this

is no better than the original Chou *et al* approximation. Using a value of 0.05 (shown in red) leads to reduced (or insignificant) biases and standard deviations across the whole spectral range. This is the default value of the factor in the RTTOV v14 code.

This is a first implementation of the Tang *et al* adjustment scheme and testing has so far focussed on ice cloud. It is therefore considered experimental, and users should consider running experiments before making use of it more generally. Future work is planned to investigate/extend the parameterisation for applicability to cloud liquid water and aerosol scattering simulations.

2.8 MFASIS-NN solver

For the simulation of visible and infrared channels in the presence of multiple scattering due to clouds and aerosols, RTTOV offers the Discrete Ordinates Method (DOM), introduced in RTTOV v12 (R12REP2017). As these accurate 1D radiative transfer solutions are normally too slow for some operational applications like data assimilation, the Method for Fast Satellite Image Synthesis (MFASIS) has been included as a fast approximation to the RTTOV-DOM solution for visible channels in the presence of clouds. MFASIS in its initial approach was based on a compressed Look-Up-Table (LUT; see Scheck *et al*, 2016, for details) and has been implemented first in RTTOV v12.2 with further improvements and updates in RTTOV v12.3, v13 and v13.1 (see also R13REP2020). In order to cover a larger range of visible and near-infrared channel frequencies and to further improve the accuracy, the LUT approach was complemented by a neural network (NN) approach in RTTOV v13.2. The NN allows the addition of more input parameters than possible with a LUT approach to characterise the atmospheric situations while at the same time reducing memory and run time requirements. The MFASIS-NN version has been first implemented in RTTOV v13.2 with further updates in v14, allowing improved simulations for many channels, especially at 1.6 μm , and the inclusion of channels at 2.2 μm . With RTTOV v14 the LUT version is discontinued and only the MFASIS-NN version is supported. Details on MFASIS-NN can be found in Scheck (2021a) and Baur *et al* (2023). A version for the fast simulation of visible channel reflectances also for aerosol affected profiles is in development.

2.8.1 General concept

In its current version, the MFASIS-NN solver is designed for the fast simulation of satellite channels in the solar spectral range in the presence of clouds and yields accurate results for non-absorbing or only weakly absorbing satellite channels. In these cases, the details of an atmospheric profile have little influence on the top of atmosphere reflectance and an arbitrary, complex NWP model profile can be described via a limited set of parameters. The relevant parameters used in MFASIS-NN for describing the clouds are illustrated in Figure

2.8.1: a two-layer ice cloud above a two-layer water- and mixed-phase cloud characterised by their optical depths and effective particle radii sufficiently capture the cloud effect on the reflectance. The two-layer cloud structure of ice, water and mixed-phase clouds includes some information on the vertical effective radii gradients and improves simulations of visible satellite channels with stronger sensitivity to effective cloud particle radii, like e.g. at $1.6 \mu\text{m}$ (see also Baur *et al*, 2023). Further parameters are the surface pressure and cloud top pressure, which effectively account for the air masses above the ground and uppermost cloud layer. In this way, effects due to Rayleigh scattering, particularly important for visible channels near the UV frequency limit, and weak absorption by carbon dioxide and methane are included.

In the first implementation of MFASIS-NN in RTTOV v13.2, the above parameters are used to characterise the atmosphere. In terms of water vapour, a fixed profile is assumed. In RTTOV v14, the column-integrated water vapour of the input NWP model profile has been introduced as additional parameter to scale the water vapour content of the simplified profile. This leads to an improvement of MFASIS-NN simulations compared to v13.2 particularly for channels weakly sensitive to water vapour absorption and reduces errors for many other channels.

Further parameters with important influence on the reflectance are the surface albedo and the viewing geometry characterised by the sun and satellite zenith angles and the scattering angle (see Figure 2.8.1).

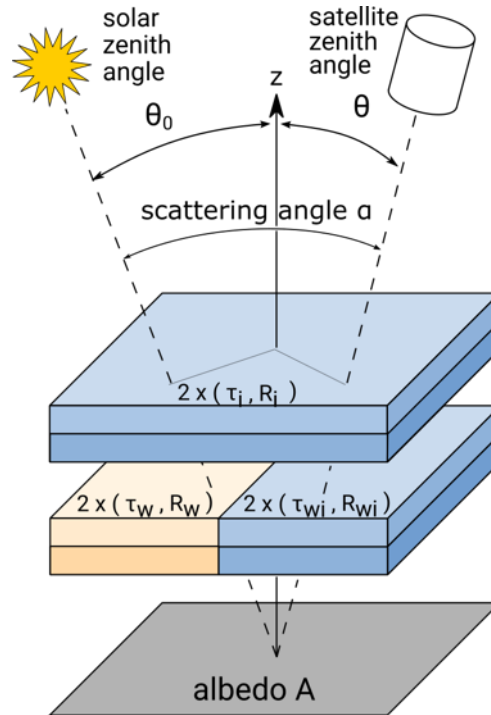


Figure 2.8.1: Schematic view of the atmospheric cloud profile simplification used in MFASIS-NN. The relevant cloud parameters are the optical depths and effective particle radii of a two-layer ice cloud on top of a two-layer water and mixed-phase cloud. See text for more details.

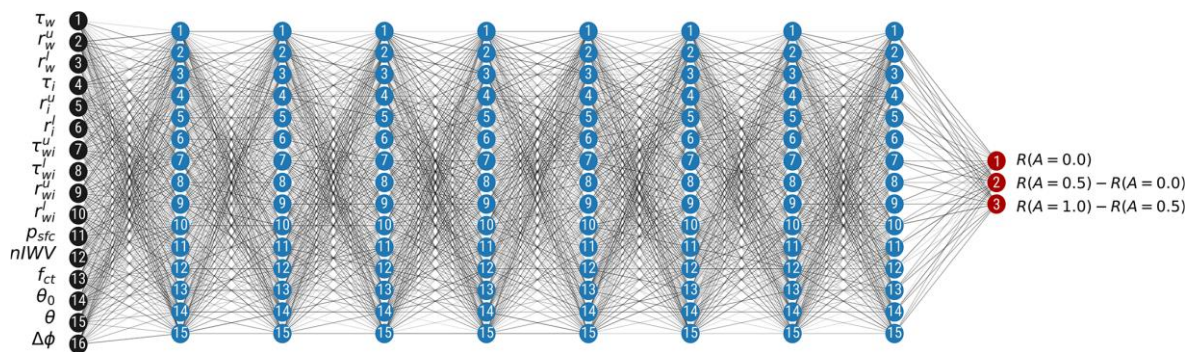


Figure 2.8.2: Neural network design used in MFASIS-NN in RTTOV v14, see text for more details.

The heart of the MFASIS-NN method is the inference of a relatively small feed-forward neural network with typically a few thousand parameters. The optimised Fortran inference code including tangent linear and adjoint versions, FORNADO (Scheck, 2021b), has been included in RTTOV. Figure 2.8.2 illustrates the neural network layout used in RTTOV v14, see also Baur *et al* (2023). The input layer consists of 16 normalised input parameters: the

parameters used to characterise the simplified profile in Figure 2.8.1, and which are derived from the NWP model profiles input to RTTOV. The optical depths of the ice cloud τ_i , water cloud τ_w and the upper and lower layer of the mixed phase cloud τ_{wi}^u and τ_{wi}^l , as well as the effective particle radii in each of the two cloud layers $r_i^u, r_i^l, r_w^u, r_w^l, r_{wi}^u, r_{wi}^l$ parameterise the clouds. Further input parameters are the surface pressure p_{sfc} , the cloud top pressure, expressed as a fraction f_{ct} relative to the surface pressure, the integrated water vapour content $n_{I WV}$ as well as the viewing geometry consisting of the sun zenith angle Θ_0 , satellite zenith angle Θ and scattering angle α . Note that in the input layer of Figure 2.8.2 the difference of the sun and satellite azimuth angles Δ_ϕ is shown instead of the scattering angle α . Both sets of angles equivalently define the viewing geometry. However, since for training the neural network synthetic profiles covering the relevant input parameter range are used in the input layer, the choice Θ_0, Θ and Δ_ϕ guarantees a more evenly sampled space for the viewing geometry in the training data set. Eight hidden layers with 15 or 25 nodes each have been found to be an optimal compromise between accuracy and performance of the neural network, depending on the specific channel (see Scheck, 2021a). The output layer consists of three nodes, providing estimates for reflectances or reflectance differences at different albedo values: $R(A = 0.0), R(A = 0.5) - R(A = 0.0), R(A = 1.0) - R(A = 0.5)$. This choice guarantees positive output values, which can be combined to obtain the final reflectance for the profile-specific albedo using an exact relation following Scheck (2021a) (and Jonkheid *et al*, 2012):

$$R(A) = R(0) + \frac{A \cdot (D_1 + D_{1/2}) \cdot D_{1/2}}{D_1 - A \cdot (D_1 - D_{1/2})} \quad (2.8.1)$$

where $D_{1/2}$ and D_1 denote the reflectance differences from the second and third neural network output nodes respectively. In this way, it is possible to treat the albedo exactly while excluding it from the input layer, thus avoiding errors from an imperfect representation of the albedo dependence by the neural network. The only difference in the neural network layout between RTTOV v13.2 and v14 is the input layer node for the integrated water vapour which was added in v14. The activation function used in the hidden layers is the cheap soft unit (CSU; see also Scheck, 2021a), a computationally cheap, piecewise quadratic approximation to the exponential linear unit (ELU). In the output layer, the softplus activation function is used, ensuring positive output values.

The training data set typically comprises a few ten million reflectances from RTTOV-DOM simulations based on synthetic model profiles. These synthetic profiles are generated using random numbers covering the entire physical range of the input parameters. The open-source Tensorflow package (Abadi *et al*, 2015) is used for training the neural network in typically 500 training epochs using $3 \cdot 10^7$ samples. An early stopping strategy is applied if sufficient convergence of accuracy gains is achieved faster.

As for the other RTTOV components, MFASIS-NN is available as a direct forward model as well as TL/AD/K models.

2.8.2 Heterogeneous surfaces

RTTOV v14 introduces a treatment for heterogeneous surfaces within the satellite footprint. As detailed in [section 2.15](#), the input profiles are extended to multiple surfaces including associated area coverage fractions and the radiance is approximated by a single radiance calculation using combined surface properties from the multiple surfaces. With scattering, the radiance is non-linear in the surface properties and this approach causes larger errors. MFASIS-NN allows for an exact treatment of heterogeneous surfaces in a simple and elegant manner and therefore follows a different approach than the other RTTOV solvers. As described above, the neural network output of MFASIS-NN consists of reflectances and reflectance differences for albedo values 0.0, 0.5 and 1.0, which are combined to the reflectance for an arbitrary albedo $R(A)$ in equation (2.8.1). For heterogeneous surfaces, equation (2.8.1) can be generalised to compute the final reflectance as the sum of the individual surface contributions of the input profile weighted by the associated surface coverage fraction f_i :

$$R(A) = \sum_{i=1}^{nsurfaces} f_i \cdot R(A_i) = \sum_{i=1}^{nsurfaces} f_i \cdot \left[R(0) + \frac{A_i \cdot (D_1 + D_{1/2}) \cdot D_{1/2}}{D_1 - A_i \cdot (D_1 - D_{1/2})} \right] \quad (2.8.2)$$

This is equivalent to calling the MFASIS-NN solver in RTTOV v14 for profiles with single surface types separately and combining the resulting reflectances via a surface area fraction weighted sum. Note that this assumes that the same cloud optical properties apply over all surface types. This may not always be true (e.g., for land vs sea) in which case the solution given here is no longer exact. An example is shown in [section 2.15](#).

2.8.3 Quality flags

Whenever the MFASIS-NN input parameters computed from the input NWP model profiles exceed the neural network limits, they are clipped to these limits. Except for the viewing geometry, this does not affect the simulated reflectances as the neural network limits are chosen such that the reflectance as a function of the input parameter of interest saturates beyond the neural network limits. Also, for most satellite instruments (DSCOVR-Epic currently being the only exception due to its special location in space), the viewing angle range of the neural network is the same as the RTTOV angle range for solar channels.

In RTTOV v13.2, MFASIS-NN follows a similar quality flagging strategy as the latest LUT version (see section 3.9.4 in R13REP2020): quality flags for limits of the sun and satellite zenith angles, the scattering angle and the profile cloud properties are available but are only set in exceptional situations. On the one hand, the flags are set in situations where a

reduced accuracy of the results is expected. On the other hand, RTTOV ensures that zenith angles and cloud effective particle radii are within the RTTOV bounds.

Therefore, the quality flagging in MFASIS-NN has been updated in RTTOV v14. Only one general flag for exceeded neural network limits is available. In practice, it is only set in situations where the sun or satellite zenith angle is exceeded. In future versions, this general flag may also be set for situations where additional input parameters need to be clipped to the neural network limits with expected impact on the simulated reflectances.

2.8.4 Code vectorisation

In RTTOV v14, a substantial acceleration of the MFASIS-NN code particularly on vector machines was achieved by vectorising the call to the neural network inference subroutine, which had been a bottleneck in the first implementation in RTTOV v13.2. This required a restructuring of the MFASIS-NN code to allow, for each channel, the simultaneous computation of reflectances for large numbers of atmospheric input profiles. On the DWD vector machine (NEC SX-Aurora Tsubasa) this achieved a speed-up of the MFASIS-NN subroutine by an order of magnitude and reduced the total CPU time of RTTOV per input profile by up to a factor of five. To profit from this feature, where possible, individual calls to RTTOV should process reasonably large numbers of atmospheric input profiles (rather than calling RTTOV for each profile separately).

2.8.5 MFASIS-NN accuracy and available instrument channels

With MFASIS-NN, the limitation of using only very few parameters to describe the simplified atmospheric profile in the LUT version was overcome. The introduction of additional parameters led to more accurate reflectance simulations, extended MFASIS-NN to more channel frequencies while still leaving room for further improvements and extensions in the future. In its current implementation, the only exception where MFASIS-NN results are still not better than or comparable with the LUT version is for the broader, water vapour sensitive SEVIRI channel at $0.8\mu\text{m}$ onboard the second generation of Meteosat satellites because of a specific correction available in the LUT version (in RTTOV versions 12.3 to 13.2). Such channels with larger water vapour sensitivity are not yet supported in MFASIS-NN, but an extension using additional input parameters is under development. Figure 2.8.3 shows MFASIS-LUT and MFASIS-NN reflectance differences with respect to RTTOV-DOM simulations based on a global ICON model field for SEVIRI's $1.6\mu\text{m}$ channel in RTTOV v13.2. The results are clearly improved for MFASIS-NN. In particular, the better representation of clouds using the two-layer structure has led to a noticeable error reduction in situations with ice or mixed-phase clouds compared to the LUT version.

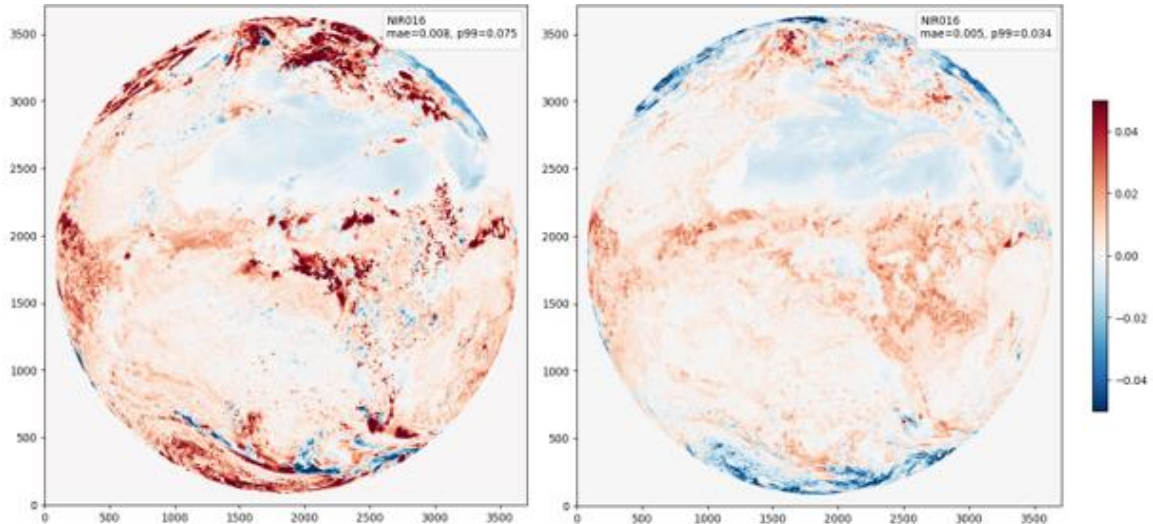


Figure 2.8.3: Reflectance differences MFASIS-LUT minus RTTOV-DOM (left) and MFASIS-NN minus RTTOV-DOM (right) based on global ICON model fields for the $1.6\mu\text{m}$ channel of the SEVIRI instrument.

The accuracy of MFASIS-NN depends on two sources of error: the reflectance error caused by replacing the NWP model profile, which is input to RTTOV, by the simplified profile represented by a limited set of parameters, see [section 2.8.1](#), as well as the additional error from the neural network training. Figure 2.8.4 provides a more quantitative evaluation of the error due to only the profile simplification as well as the total MFASIS-NN error, where both error sources contribute. The reflectance difference histogram (left panel in Figure 2.8.4) shows the improvement of MFASIS-NN in RTTOV v14 compared to v13.2 due to the additional input parameter for the integrated water vapour for SEVIRI's $1.6\mu\text{m}$ channel. The evaluation is based on RTTOV-DOM and MFASIS-NN reflectance simulations for a collection of 5000 diverse IFS model profiles (NWP SAF profile dataset; Eresmaa and McNally, 2014 & 2016) using 64 randomly chosen viewing geometries. It also demonstrates that the error due to the neural network training is small compared to the profile simplification error. The right panel shows the reduction of the profile simplification error from RTTOV v13.2 to v14 for several satellite instruments and channel frequencies due to the additional input parameter. The results are obtained for an albedo value of 1, where the effect is largest. Channels with wavelengths below $\sim 0.7\mu\text{m}$ are already very well described by the input parameters available in RTTOV v13.2. Particularly for the very short wavelengths in this frequency range, Rayleigh scattering effects play an important role, and they are already accounted for sufficiently by the surface and cloud top pressure input parameters. The addition of the integrated water vapour as input parameter noticeably improves results for channels with weak water vapour sensitivity, e.g. at $1.2\mu\text{m}$, $1.6\mu\text{m}$ and $2.2\mu\text{m}$. Channels with larger water vapour sensitivity, e.g. FCI's $0.9\mu\text{m}$ and $1.3\mu\text{m}$ channels, or channels that are affected by other absorption lines, e.g., MetImage's oxygen-sensitive channel at

0.7 μm , still have relatively large profile simplification errors. Their simulation with MFASIS-NN requires additional neural network input parameters to achieve similar accuracy. Note that work is ongoing to extend MFASIS-NN to channels with larger water vapour sensitivity.

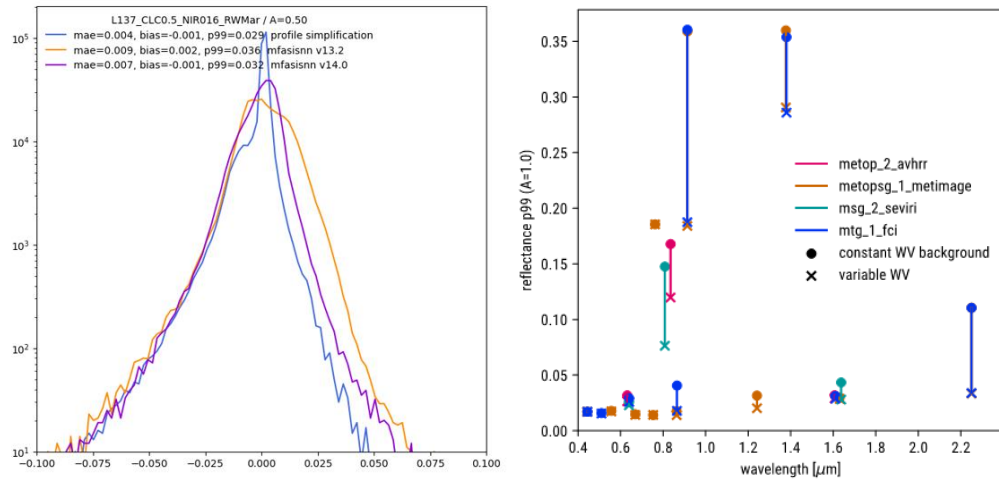


Figure 2.8.4: Evaluation of MFASIS-NN accuracy with respect to RTTOV-DOM simulations. Left panel: Reflectance differences (MFASIS-NN minus DOM) using MFASIS-NN in RTTOV v13.2 (orange) and RTTOV v14 (purple), as well as reflectance differences from RTTOV-DOM simulations based on simplified profiles as used in RTTOV v14 and full model profiles (blue) for SEVIRI's 1.6 μm channel. The simulations are based on the NWP SAF profile dataset for various viewing geometries. Right panel: 99th percentile of the reflectance error from the profile simplification in RTTOV v13.2 (circles) and RTTOV v14 (crosses) based on RTTOV-DOM simulations for various satellite instruments and channel frequencies.

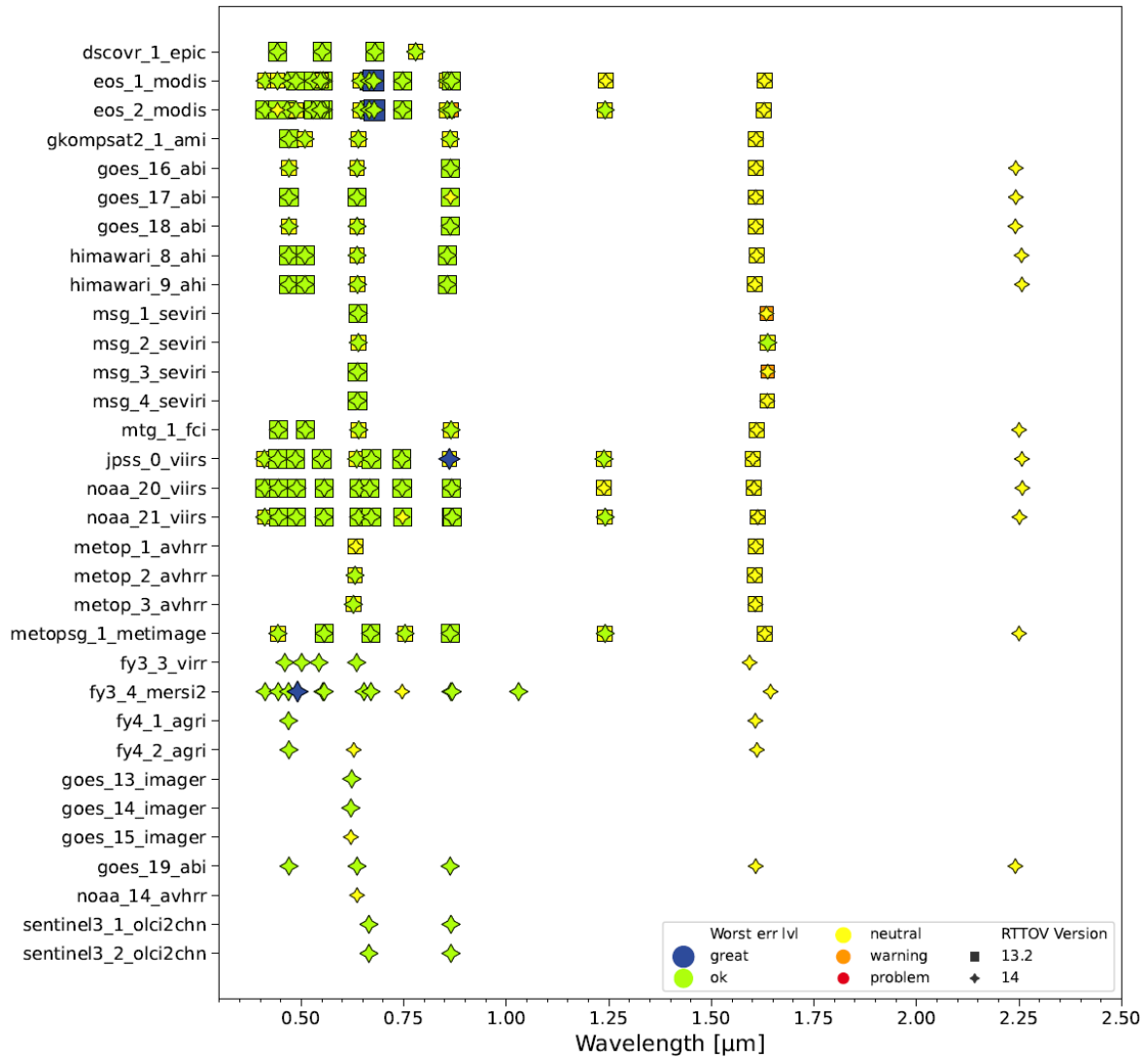


Figure 2.8.5: Overview of the satellite instruments and channel frequencies supported by MFASIS-NN in RTTOV v13.2 (square symbols) and RTTOV v14 (diamond symbols). Colours indicate the expected accuracy of MFASIS-NN simulations for the specific channels. See text for more details.

	me	mae	rmse	p99	p999
blue ('great')	< 0.002	< 0.005	< 0.005	< 0.02	< 0.04
green ('ok')	< 0.005	< 0.010	< 0.010	< 0.03	< 0.06
yellow ('neutral')	< 0.010	< 0.020	< 0.020	< 0.04	< 0.08
orange ('warning')	< 0.015	< 0.030	< 0.030	< 0.05	< 0.10

Table 2.8.1: Colour code tables for the mean error (me), mean absolute error (mae), root mean square error (rmse), 99th percentile (p99) and 99.9th percentile (p999) used to classify the MFASIS-NN accuracy. The intervals are defined successively by their upper limit.

A complete overview of the satellite instruments and channel frequencies supported by MFASIS-NN in RTTOV v13.2 and RTTOV v14 including a colour coding for the expected accuracy is given in Figure 2.8.5. The accuracy of each channel is evaluated by comparing MFASIS-NN and DOM simulations based on the NWP SAF profile dataset and several viewing angles. The colour in the overview represents the worst of the categories 'great', 'ok', 'neutral', 'warning' of the mean error, mean absolute error, root mean square error, 99th and 99.9th percentile of the evaluations per instrument channel, see Table 2.8.1. Note that channels with large errors (red colour, 'problem' in Figure 2.8.5) are subject to further development and are currently not supported by MFASIS-NN, and not listed in the overview plot. All supported channels in RTTOV v14 are classified 'neutral' or better in accuracy. The overview shows the accuracy benefit for some channels and the significant increase in the number of supported instruments and channels with RTTOV v14.

More details on the expected accuracy for all satellite instruments and channel frequencies supported by MFASIS-NN are provided here:

https://nwp-saf.eumetsat.int/downloads/rtcoef_rtov14/MFASISNNFitAndInterpErrors.pdf

2.9 Flexible VIS/IR hydrometeor optical properties

For aerosol simulations in RTTOV, the aerosol optical property files contain optical property data for an arbitrary number of particle types, and RTTOV automatically adapts to the number of aerosol species. This has made it straightforward to generate aerosol optical property files representing alternative sets of aerosol species such as those from the ECMWF Copernicus Atmospheric Monitoring Service (CAMS) model, or more recently those from the ICON-ART model (see [section 2.10](#)). RTTOV v13.0 introduced the same flexibility for the hydrometeor optical property files for microwave sensors.

By contrast, the cloud optical properties for visible/infrared sensors have been somewhat rigidly defined. RTTOV v13 and earlier supported only cloud liquid water and cloud ice water (no other hydrometeor types), and when new optical property parameterisations were introduced, users were forced to select between parameterisations for cloud liquid water, and between parameterisations for cloud ice water. It was not possible to use the different parameterisations for cloud ice simultaneously in the same profile, for example.

RTTOV v14.0 introduces fully flexible optical properties for visible/infrared sensors. The same optical properties are provided as in RTTOV v13, but the hydrometeor optical property file defines the number of available particle types (as for aerosols and the microwave hydrometeor files), and the user is free to use them in any combination in the simulation.

In practice, for the current optical properties it may not make sense to use them all simultaneously. However, this update has significant advantages. It enables the potential for hydrometeor optical property files containing properties for other hydrometeor types than just cloud liquid and ice (such as rain, snow, graupel, and so on). It has enabled unified data structures and the associated file format to be defined for all optical properties across the whole spectrum. It is now possible in principle to generate and use hydrometeor optical properties that are consistent across the whole spectrum from ultra-violet through to the microwave (this is planned for a future release). This forms part of the longer-term goal of improving the spectral consistency in RTTOV described above. Finally, it also makes it possible in principle to create a tool to enable users to generate their own custom visible/infrared hydrometeor optical property files which previously was not practical to do (this is also a longer-term goal).

2.10 ICON-ART aerosol optical properties

RTTOV's application range for aerosol simulations in the visible and infrared spectral range has been extended to the ICON-ART aerosol model. ICON-ART aerosol optical properties have been introduced in RTTOV v13.2 for a subset of species from the ICON-ART model. The corresponding optical property files are made available upon request via the NWP SAF helpdesk. For RTTOV v14, ICON-ART aerosol optical property files are provided on the coefficient website along with the OPAC and CAMS aerosol optical property files. The implementation of ICON-ART aerosol optical properties has been done within an NWP SAF visiting scientist mission. Here, a short overview is provided while a detailed description is available in Muser *et al* (2022).

Look-up tables for the optical properties of the ICON-ART aerosols mineral dust (three modes), sea salt (three modes) and soot (one mode) are precomputed using Mie or T-matrix calculations. The calculations take into account the same assumptions made about the particle size distributions, particle compositions and particle shapes as used in the numerical ICON-ART model to ensure consistency for the RTTOV forward operator.

ICON-ART uses a modal description for the size distribution, where each mode is approximated by a log-normal distribution and represents a range of different particle sizes. The complex refractive indices, taking into account the chemical composition of the particles in their interaction with radiation, is taken from the HITRAN database for sea salt and soot, and from Gasch *et al* (2017) for mineral dust. Sea salt and soot are assumed to be spherical particles and Mie calculations based on the input of refractive indices for a certain spectral range are used to precompute their optical properties. The T-matrix is designed for non-spherical particles, particularly solid particles such as mineral dust. For ICON-ART, the optical properties of mineral dust are based on data from Meng *et al* (2010), who combined

several methods, such as T-matrix calculations and geometric optics, to compile a dataset for tri-axial ellipsoidal mineral dust particles.

An extension to additional ICON-ART aerosol species, having optical properties varying in time, is envisaged for a future RTTOV version.

2.11 Updates to microwave hydrometeor optical properties

RTTOV radar simulations presented in this section are carried out using RTTOV v13. [Section 2.6.3](#) includes a comparison of radar reflectivities between v13 and v14 showing that the differences are small.

2.11.1 Large hydrometeor contents

Since RTTOV v13.2, it has been possible to generate microwave hydrometeor optical properties (hydrotables) using lookup tables spanning a wider range of temperatures and water contents. These lookup tables are not distributed by default but can be optionally generated by the user. The primary application for these extended “v13.2” tables is radar simulations. The following table shows the different ranges. Note that hydrotables with both “v13.0” and “v13.2” settings work with RTTOV v14.0.

	“v13.0” microwave hydrotables	“v13.2” microwave hydrotables
Water contents [kg/kg]	10e-6 - 10e-2	10e-7 - 10e-1
Temperatures (frozen hydrometeors) [K]	204 - 273	178 - 277
Temperatures (liquid hydrometeors) [K]	234 - 303	234 - 333

In “v13.2” hydrotables, water contents are calculated for contents up to 10^{-1} kg/kg, whereas they were only calculated for contents smaller than 10^{-2} kg/kg in the previous versions. As justification, Figure 2.11.1 shows a comparison of a vertical profile of Ku band reflectivity observed by GPM/DPR and simulated with ARPEGE before (in red) and after extending the hydrometeor tables to 10^{-1} kg/kg. As shown by Figure 2.11.1, this extension allows to provide a better fit to the observations above an altitude of approximately 4 km, consistent with the existence of content larger than 10^{-2} kg/kg at these levels for this specific profile. It should be noted that increasing the lookup tables to larger hydrometeor contents doesn’t impact so much the simulation of passive microwave observations (not shown here) but has a noticeable impact on the radar simulations.

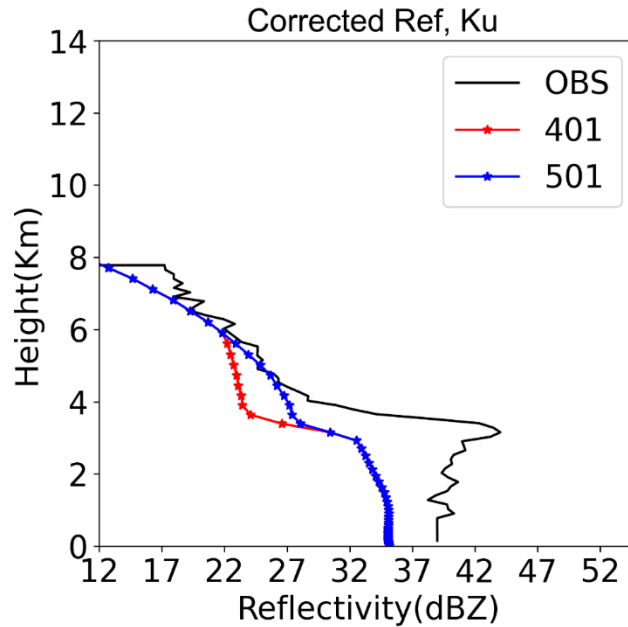


Figure 2.11.1: An observed (in black) vertical profile of GPM/DPR Ku-band reflectivity is compared with ARPEGE simulations before (in red) and after (in blue) extending the hydrometeor lookup tables to 10^{-1} kg/kg.

There are two reasons for the extended temperature range. First, to enable the use of the improved melting layer scheme, temperature bins must go up to 277 K to represent the presence of partially melted particles at temperatures above freezing, and to provide a means to vary the optical properties as a function of temperature through the extended melting layer. Second, significant amounts of frozen hydrometeors are present down as low as 180 K, as shown using the IFS model by Scanlon *et al* (2023). Scanlon *et al* also show that the temperature bin is unnecessary for the liquid hydrometeors, but the number of bins is fixed across all types, so the number of bins for liquid hydrometeors is also extended. Further testing of a prototype version of the move from v13.0 to v13.2 hydrotables is shown in Scanlon *et al* (2023), showing the effect on a sample of simulated TBs in the IFS, and reproduced here (Figure 2.11.2). For standard passive microwave simulations from the IFS, without bright band, maximum changes are around -0.06 K when the temperature range is extended and around -2.0 K when the water content range is extended.

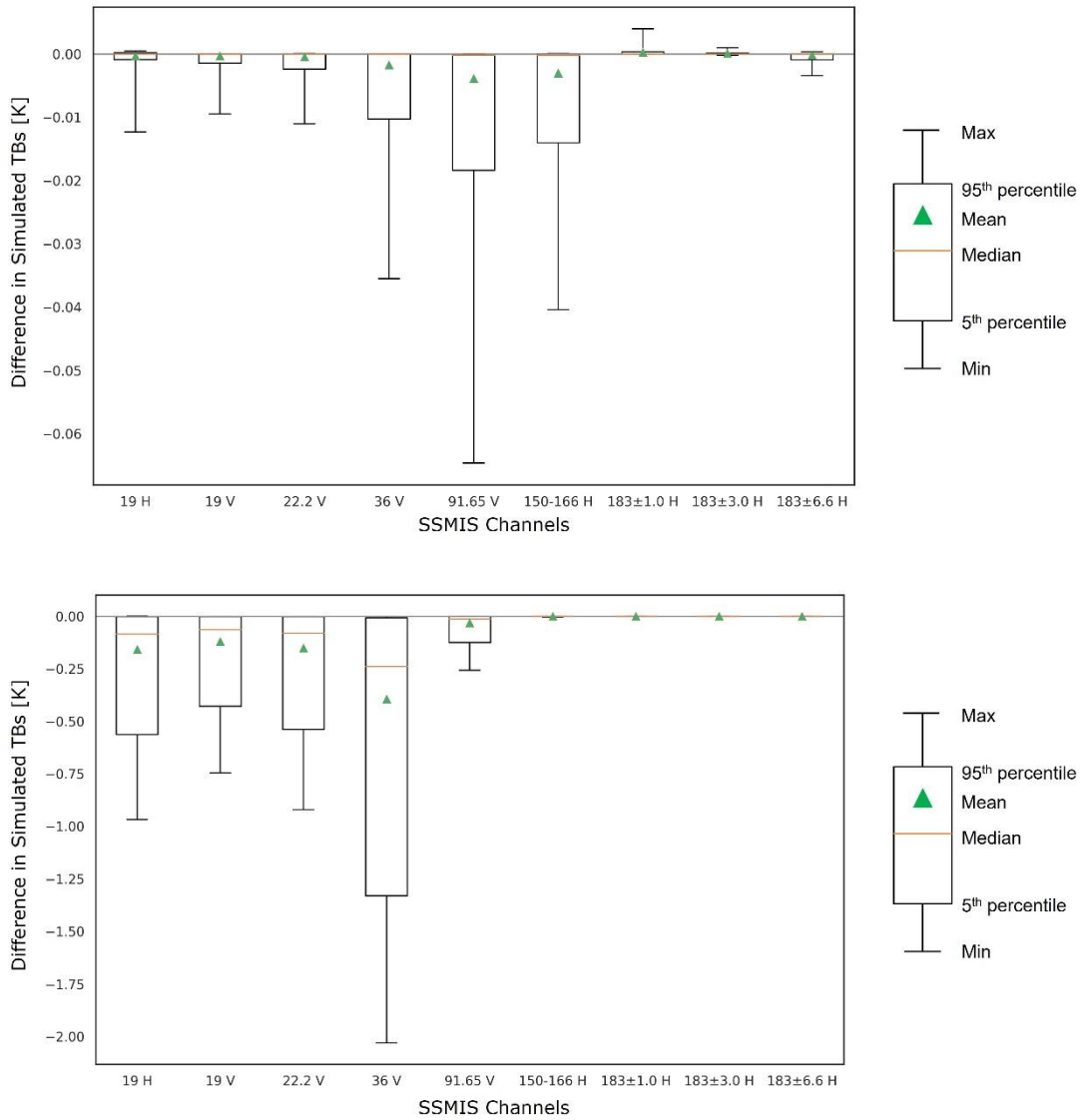


Figure 2.11.2: Figures 26 (upper) and 24 (lower) from Scanlon et al (2024). Upper plot: Change in the simulated TBs when the temperature range of the hydrotables is extended. Lower plot: Change in the simulated TBs when the LWC range of the hydrotables is extended. Both plots present global statistics for the period 2020-07-01 to 2020-07-31.

2.11.2 New PSD options

In addition to the commonly used Marshall and Palmer (1948) PSD (hereafter MP) for rain, two other PSDs have been implemented since RTTOV v13.2. The Abel and Boutle (2012) (with $x_1 = 0.22$ and $x_2 = 2.2$) PSD (hereafter AB) is now also available for large-scale rain. For convective rain, the Illingworth and Blackman (2002) can also be used (hereafter IB). The AB and IB PSD options can be activated when generating the hydrometeor lookup tables. These two PSDs have been successfully used to simulate CPR reflectivities at the 94 GHz frequency in the ECMWF IFS model (Fielding and Janisková, 2020).

Figure 2.11.3a shows the number density (m^{-4}) as a function of the diameter (mm) for different hydrometeor contents (in colours) for the AB PSD (dashed lines) and for the MP PSD (plain lines). The resulting hydrometeor lookup tables are also shown in Figure 2.11.3c at Ku band. They indicate that the use of the AB PSD for stratiform rain decreases the reflectivity for contents below about $10^{-4} \text{ kg.m}^{-3}$, consistent with the fact that the AB PSD tends to diagnose a larger (resp. smaller) number of small (resp. large) particles, compared to the MP PSD for this specific content (blue curve in Figure 2.11.3a). Similarly, the AB PSD increases the reflectivity for contents greater than $10^{-3} \text{ kg.m}^{-3}$, consistent with the greater number of larger particles diagnosed using the AB PSD (see red, yellow and purple curves in Figure 2.11.3a). Finally, Figure 2.11.3c shows that the use of the IB PSD (in yellow) for convective rain results in smaller reflectivities, compared to the ones derived using the MP PSD (in black).

To test these two PSD options, simulations have been performed for the Dual Precipitation Radar (DPR) instrument onboard the Global Precipitation Measurement (GPM) mission using the Météo-France ARPEGE global NWP model for two different one-month periods (June 2020 and January 2021). In Figure 2.11.4 the impact of using the AB PSD for stratiform rain, and IB PSD for convective rain (in blue) is compared with the radar simulations performed using either the default MP PSD for both rain species (in red), or with the MP PSD for stratiform rain and the IB PSD for convective rain (in green). The use of the AB PSD for stratiform rain, and IB PSD for convective rain allows to reduce the bias between Ku-band observations and the simulations in the northern hemisphere and in the tropics. A different tendency is observed in the Southern Hemisphere.

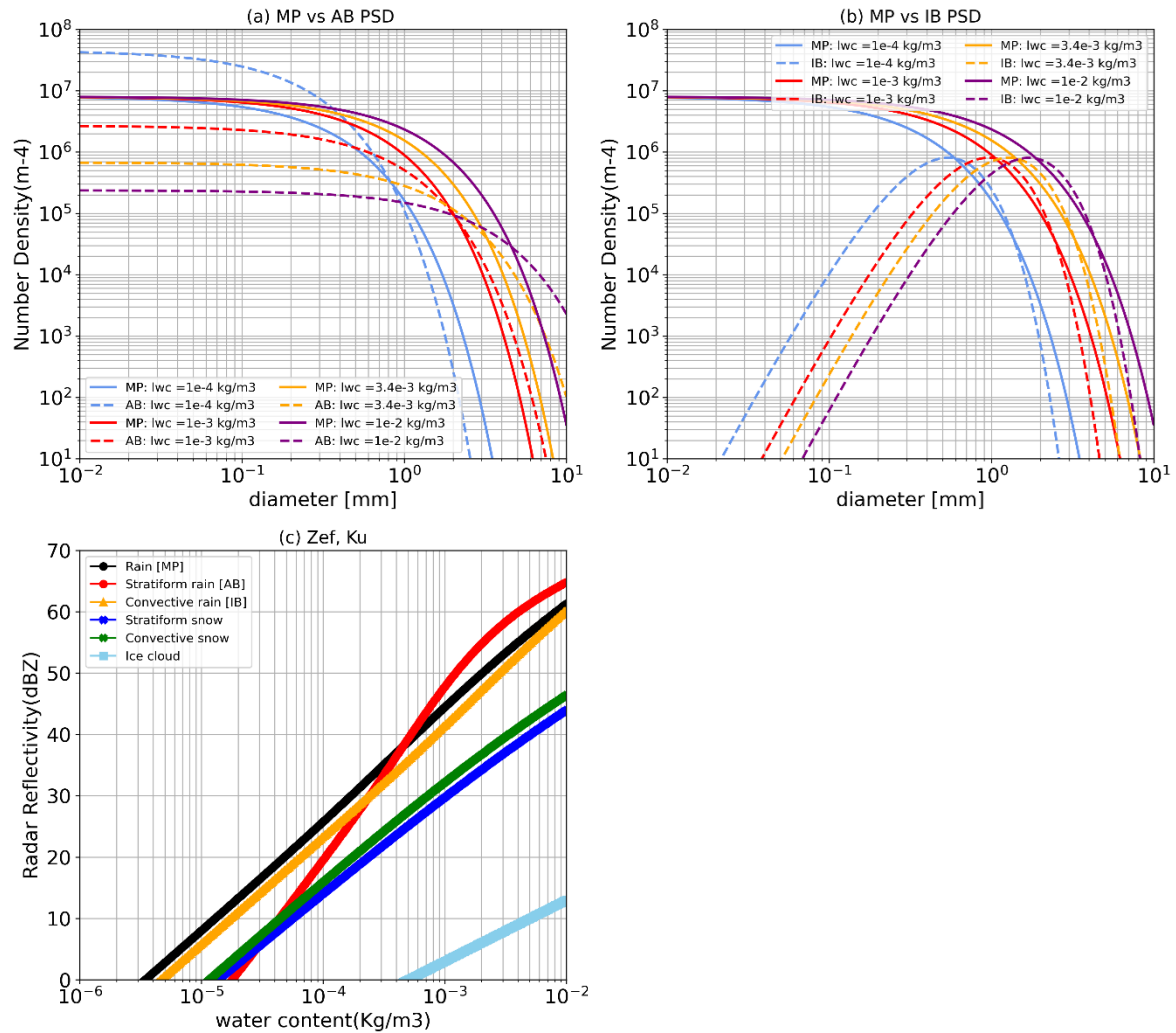


Figure 2.11.3: Panel a shows the number density (in m^{-4}) as a function of the diameter (in mm) for the Abel and Boutle (2012) PSD (dashed line) and the Marshall and Palmer (1948) PSD (plain line) for different rain contents. Similarly, panel b shows the number density as a function of the diameter for the Illingworth and Blackman (2002) PSD (dashed line) for different rain contents. The resulting hydrometeor lookup tables, representing the reflectivity as a function of the content, are depicted in panel c.

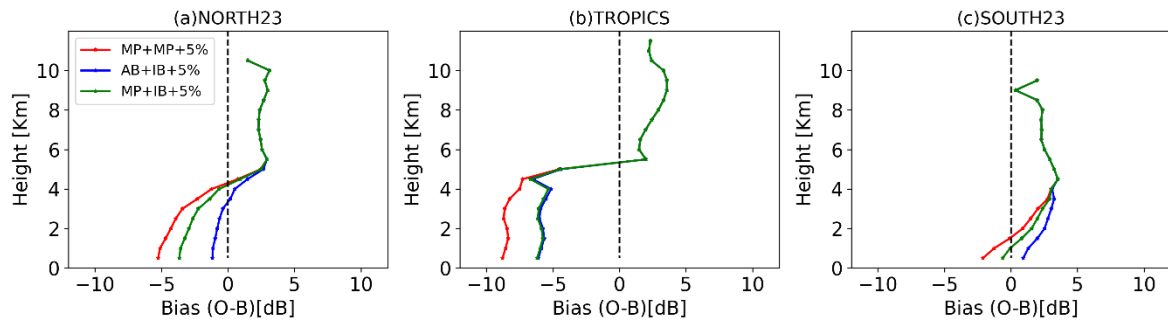


Figure 2.11.4: Vertical profile of the bias of first-guess departure between GPM/DPR Ku band reflectivity observations (corrected from the attenuation), and the simulations performed using the global NWP model ARPEGE with a precipitation fraction of 5% for convective hydrometeors. Simulations have been carried out with different pair of PSD options for stratiform and convective rain: Marshall and Palmer (1948) for both species (in red), Able and Boutle (2012) for stratiform rain with Illingworth and Blackman (2002) for convective rain (in blue), and MP for stratiform rain with IB for convective rain. The statistics have been computed for two different one-month periods (June 2020 and January 2021).

2.11.3 Updates on the bright-band

Based on the work of Mangla *et al* (2025), the optional Bauer *et al* (2001) melting layer parameterisation has been updated for microwave radiometers and radars since v13.2. Note that the bright band is deactivated in standard (“v13.0”) hydrotables. This revised parameterisation provides a smoother and more accurate vertical representation of the reflectivities in the bright band. The design of the revised bright band extends the melting layer to 277 K rather than just to 275 K, based the existence of frozen hydrometeors at these temperature layers in global NWP models. The change also introduces an ad-hoc scaling factor that helps reduce backscatter and improves the fit to the observations. The revisited parameterisation, as well as the different equations, are fully documented in the Appendix B of Mangla *et al* (2025).

A potential limitation of the scheme is that the results are based on Mie spheres whilst a more physical non-spherical modelling of melting particles is being developed (Johnson *et al*, 2016). Therefore, the next step would be to further enhance this melting layer formulation with one that follows a stronger physical basis, including modelling of non-spherical particles. That may be a challenging task and depends on ongoing developments in non-spherical modelling, so it is left for future work.

2.11.4 Phase functions

With the unification of microwave scattering radiative transfer (formerly RTTOV-SCATT, [section 2.6](#)) into the main RTTOV processing, it has become theoretically possible to use the DOM solver (R12REP2017) as an alternative to the delta-Eddington for microwave scattering radiative transfer. However, the DOM solver requires the normalised scattering phase function projected onto Legendre functions, known as the Legendre coefficients. Hence, at v14 we have added the capability to generate Legendre coefficients and to store them in the microwave hydrotables. This facility is controlled by a new switch in the channels.dat file, labelled "(T/F) - Include phase functions in the hydrotables". The treatment of microwave phase functions broadly follows what has already been implemented for infrared and visible DOM radiative transfer. The source of the phase functions used by the hydrotable generation code is as follows:

For optical properties based on particle shapes from the ARTS database, which includes a range of frozen hydrometeors and a liquid sphere, a new extension of the ".rssp" summary optical property format has been provided by the ARTS team. The new format extends the original format to include tables of phase functions. Within the RTTOV world, these input files containing phase functions are labelled ".full" to distinguish them from the existing .rssp files which only contain the basic scattering parameters, e.g., the phase function is represented only by the asymmetry parameter g . Due to their size, the .full files are not provided as part of the standard RTTOV package and must be requested specially from NWP SAF. ARTS phase functions are provided at 721 zenith angles (every 0.25 degrees from 0 (forward) to 180 (backward) scattering) in order to preserve fine-scale features of the scattering that become particularly important for frozen hydrometeors in the sub-mm part of the spectrum.

For optical properties based on the Mie Sphere, typically rain and cloud, the phase function is generated using internal RTTOV routines that calculate the Mie solution on the fly. Phase functions are computed on the 721 zenith angle grid consistent with the ARTS database.

For optical properties based on the Liu database (for example the sector snowflake), the Liu database already provides phase functions on 33 zenith angles, every 5 degrees. The hydrotable generation software is not yet adapted to work on multiple zenith angle grids at once so output of phase functions for particle types from the Liu database is not currently supported but is planned for a future release.

The phase functions from the Liu database are already normalised, but the Mie sphere and ARTS input phase functions are full phase functions. In any case, prior to further processing, the phase functions are normalised. To compute the bulk phase function integrated across the chosen particle size distribution, these normalised phase functions are weighted according to the particle scattering extinction for each particle size in the integration. The

resulting bulk normalised phase function, on the 721 zenith angle grid, is then converted to Legendre coefficients up to a maximum number of 32 currently. These phase functions are then written to the hydrotable. The microwave hydrotables may be generated either with or without the phase functions. The standard distribution does not include phase functions.

To check the quality of the phase function, a comparison is made between the integrated phase function and the pre-computed asymmetry parameter, g . This check is currently only made for the largest particle size of each type, for the highest temperature bin, for performance reasons. An error is thrown if the difference exceeds a tolerance of 0.01 for Mie or Liu optical properties, or 0.05 for ARTS optical properties. The need for larger tolerance for ARTS properties is not fully understood but likely is associated with the much sharper phase function features at high frequencies when considering non-spherical frozen particles; in any case most comparisons to the ARTS asymmetry are correct within 0.02 to 0.03.

Figure 2.11.5 shows an example of the reconstructed phase function for snow, based on the standard RTTOV large plate aggregate hydrometeor, in ATMS channel 18 (183+/-7 GHz), and based on a representative vertical level in an RTTOV test profile. This reconstruction is based on 8 Legendre coefficients, corresponding to a typical setting of the DOM solver. The sharp forward scattering peak, and broader forward scattering lobe, are expected from snow hydrometeors at higher frequencies.

Further validation and testing of the RTTOV DOM capability in the microwave, as compared to the default and widely-used delta-Eddington approach, are ongoing. Hence, users are advised to only use this facility with caution. For this reason, also, microwave hydrotables containing phase functions are not yet provided to users, although the facility to generate them exists as described above.

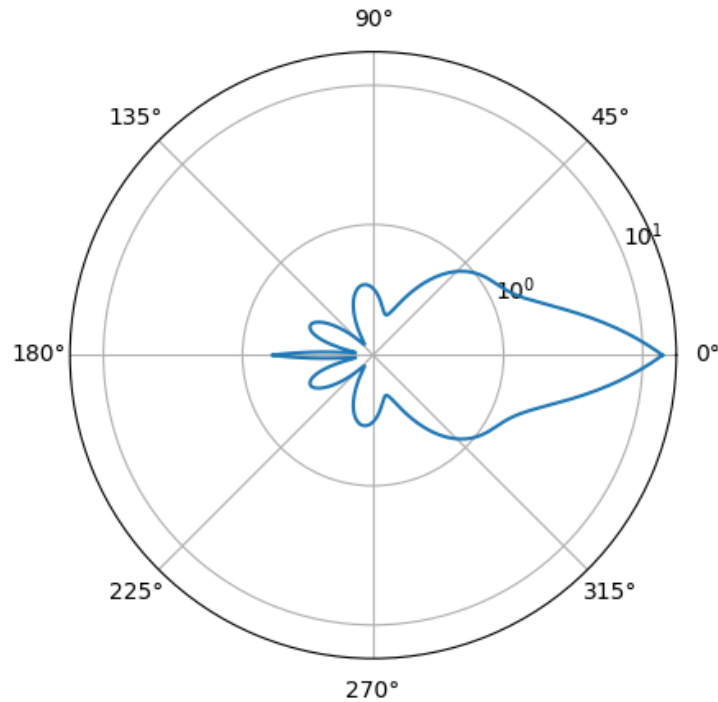


Figure 2.11.5: Example of a microwave scattering phase function used in the DOM solver around 183 GHz, based on the ARTS large plate aggregate bulk optical properties, and reconstructed from the 8 Legendre coefficients used by the solver.

2.12 Physically based polarisation treatment

Since RTTOV-SCATT v13.0, a method to approximate the effects of oriented frozen hydrometeors has been introduced. This empirical scheme symmetrically rescales the extinction in vertical (V) and horizontal (H) channels, effectively capturing the orientation-induced brightness temperature differences between V and H polarisation – known as the polarisation difference (PD) (Barlakas *et al*, 2021). Notably, this scheme is applicable only to conical scanners. Modelling the effects of oriented frozen hydrometeors for cross-track scanners is considerably more challenging, as the bulk optical properties – including but not limited to extinction – strongly depend on the zenith angle (Earth incidence angle), while the earth-relative polarisation rotates with the sensor's observation (scan) angle. To address this, RTTOV-SCATT v13.2 introduced an alternative, more physically based scheme suitable for both cross-track and conical scanners. Unlike the earlier empirical approach, the new method uses simulated horizontally oriented hydrometeors to represent changes in mean bulk scattering properties as well as polarisation differences.

The new scheme is implemented as a four-dimensional (4D) lookup table (LUT), which contains scaling factors dependent on frequency, temperature, angle, and water content. These factors are applied to the bulk optical properties of frozen species in each layer, approximating the optical properties of oriented frozen hydrometeors. The parameterisation has been validated against full polarisation simulations using a reference-quality radiative transfer model (Barlakas *et al*, 2022).

This scheme is designed to improve upon and supersede the earlier parameterisation, even for conical scanners. As described in Barlakas *et al* (2022), an asymmetry exists between polarisations, necessitating a larger scaling for H polarisation than for V polarisation. Finally, the scheme includes a parameterisation for radar backscattering. For more complete scientific details of the polarisation upgrade to RTTOV-SCATT, see Barlakas *et al* (2022). The scheme has subsequently been assessed within the IFS and brief results are presented here.

The impact of the new scheme on MHS radiances simulated from the IFS is shown in Figure 2.12.1. The left-hand panel shows simulated MHS channel 5 brightness temperatures in a small part of the north Pacific region with areas of TB below 250 K broadly indicating the presence of scattering generated by frozen particles (broadly snow, graupel/hail and ice cloud). The impact of representing scattering effects from oriented particles for the first time is shown in the right-hand panel. These changes are strongest at the centre of the swath (in other words they are largest near nadir) and they are, as expected, limited to the regions of depressed TBs caused by scattering from frozen particles. The new scheme broadly reduces the simulated brightness temperatures at nadir, due to the effect of horizontally aligned particles generating increased extinction compared to randomly oriented particles, consistent with the results in Barlakas *et al* (2022).

Activation of the new particle orientation treatment was also tested within the cycled data assimilation at ECMWF. For microwave imagers, (e.g. GMI, SSMIS, AMSR2) this meant an upgrade from the earlier particle orientation parameterisation. For sounders (e.g. MHS, AMSU-A, MWHS-2) this meant that particle orientation was represented for the first time, with effects similar to what is shown in Figure 2.12.1. Analysis-based forecast verification showed no significant impact. Background fits (standard deviation of background departures) to some independent observations were slightly degraded (e.g. 0.1-0.2% in ATMS humidity channels being assimilated in clear sky condition) but in most cases unaffected. Background fits to both microwave imagers and sounders directly affected through the change to the forward operator were also degraded: by up to 1% in specific microwave imager channels (e.g. GMI channels 166v and 183+/-7v); up to 3% for lower-peaking microwave sounder 183 GHz and 118 GHz channels; up to 0.7% for AMSU-A channel 5. This could be broadly down to the increased cloud effect (e.g. stronger scattering at nadir in the simulations) rather than a true sign of worse simulations (ultimately due to

the precipitation double penalty effect which can increase standard deviation when clouds are more accurately represented). However, further study and, if possible, more detailed observational validation of the oriented scattering signature would be required to justify such a change for an operational forecasting system. Hence the new scheme is not active by default in RTTOV v14 but is left for the moment as an option for advanced users, pending further validation and testing.

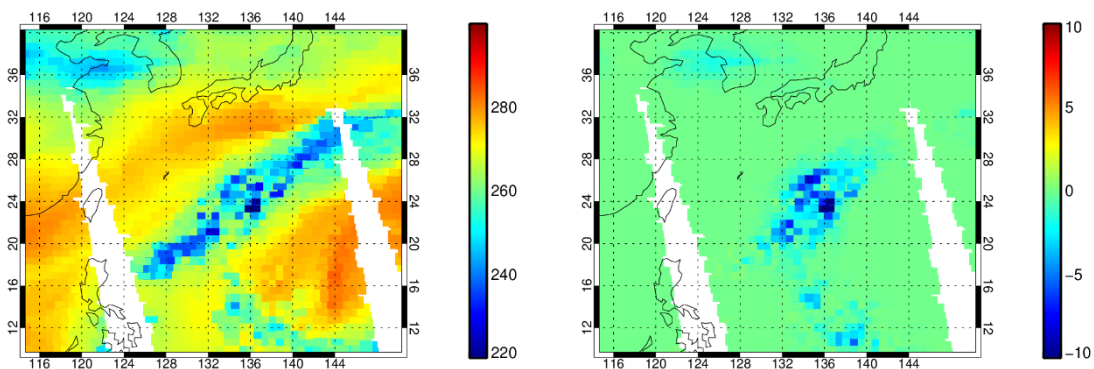


Figure 2.12.1: Impact of the new representation of scattering from oriented particles on channel 5 of MHS on Metop A around 1200 UTC on 1st December 2020: left: simulated TBs (K) with the new scheme; right: difference in TB compared to default simulations assuming total random particle orientation.

2.13 Per-channel effective Tskin input

The surface skin temperature in RTTOV is converted to the black-body equivalent radiance for each channel and multiplied by the channel-dependent surface emissivity to give the surface-emitted radiance in each channel. RTTOV has historically allowed a single surface skin temperature value per profile that is used for all channels being simulated for that profile. This is typically assumed to be the temperature of the very top layer of the surface, be it land, ocean/water, or sea-ice, as represented in NWP models.

However, some instruments, especially those in the microwave region of the spectrum, are sensitive to the sub-surface. The depth to which each channel is sensitive is dependent on the channel frequency (amongst other variables). Therefore, the effective radiative skin temperature may in practice be different for each channel, being better specified as some sort of averaged temperature through the relevant layers of the sub-surface.

The option to specify per-channel effective radiative skin temperatures was implemented in RTTOV v13.2 to support users wishing to study the impact and potential benefits of this. It

is up to the user to determine the appropriate input effective skin temperature value for each channel when this option is enabled.

2.14 Microwave sea surface emissivity models

A new fast microwave sea surface emissivity model, SURFEM-Ocean, was implemented in RTTOV v13.2. Full details of SURFEM-Ocean are given in Kilic *et al* (2023). A brief overview is given here.

SURFEM-Ocean is a neural-network-based parameterisation of the Passive and Active Reference Microwave to Infrared Ocean (PARMIO) physical radiative transfer model (Dinnat *et al*, 2023). PARMIO is a modular physical model allowing different parameterisations to be selected for the dielectric constant, foam coverage, foam emissivity, and wave spectrum. SURFEM-Ocean is trained on a particular configuration of PARMIO intended to provide good agreement for upcoming sensors in the sub-mm spectral region (up to 700 GHz) as well as for current sensors operating at frequencies below 200 GHz.

Inputs to SURFEM-Ocean (with valid ranges) are frequency (0.5 – 700 GHz), 10m wind speed (0 – 50 ms⁻¹), relative wind direction compared to the satellite view direction, satellite zenith angle (0 - 89°), sea surface temperature (-2 – 32°C), and sea surface salinity (0 – 40 psu).

The dielectric constant (emissivity for flat surface with zero wind speed) is computed via the physical model of Meissner and Wentz (2004, 2012). The emissivity contributions from isotropic and anisotropic wind-induced surface roughness are computed via neural network parameterisations of a selected PARMIO configuration.

SURFEM-Ocean computes emissivities for vertically and horizontally polarised radiation as well as for the third and fourth Stokes components. As such SURFEM-Ocean is applicable to all microwave instruments supported by RTTOV and is the recommended microwave sea surface emissivity model. The non-specular correction for surface reflectance applied in FASTEM versions 2 (Deblonde and English, 2001) and above is used for SURFEM-Ocean in RTTOV. The surface reflectance (referred to as diffuse reflectance in the RTTOV user guide, see [section 2.16](#) below) is used when considering downwelling radiation emitted by the atmosphere that is reflected by the surface and may then reach the satellite.

Geer *et al* (2024) presents results from the use of SURFEM-Ocean in the ECMWF operational NWP system.

RTTOV v14 retains the pre-existing FASTEM-5 (Bormann *et al*, 2012) and FASTEM-6 (R12REP2017) microwave sea surface emissivity parameterisations. The FASTEM-3

(R8REP2006) azimuthal calculation has been implemented for FASTEM-6 to enable emissivity computations for the third and fourth Stokes components. This means that FASTEM-6 may now also be used for polarimetric sensors but is not applicable in the sub-mm (see below). FASTEM-5 has been retained to provide continuity for some users but is not generally recommended and should not be used for polarimetric sensors or sub-mm sensors. FASTEM versions 1-4 have been removed from the code as they have been fully superseded by FASTEM-6 and now SURFEM-Ocean.

Figures 2.14.1 and 2.14.2 (reproduced from Kilic *et al*, 2023) compare emissivities and brightness temperatures respectively between SURFEM-Ocean and FASTEM-6 for nine different wind speeds and four polarisations.

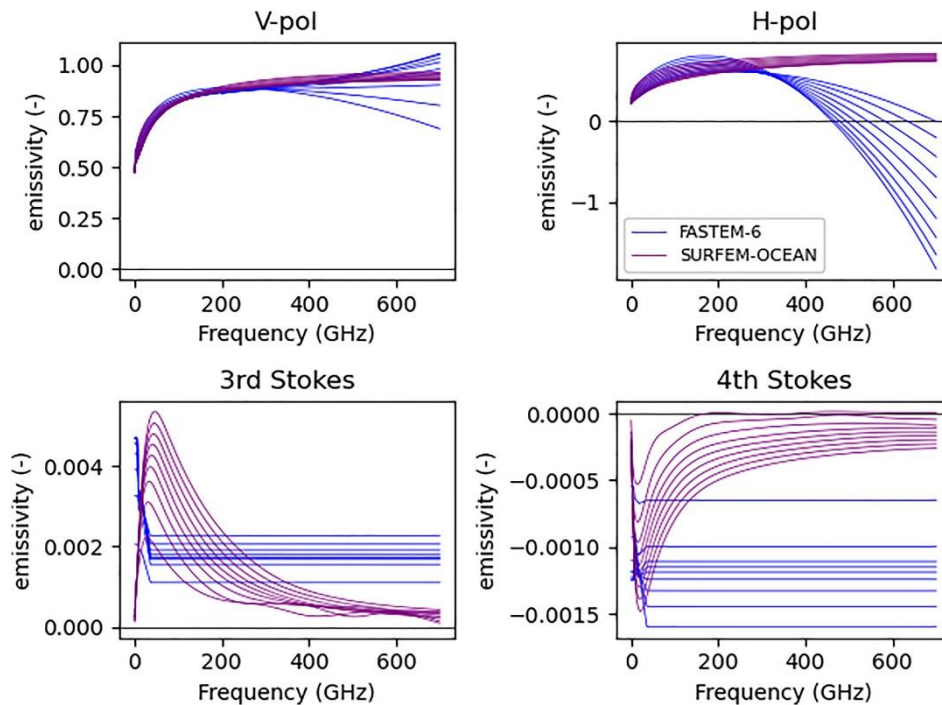


Figure 2.14.1: Plots of emissivities from SURFEM-Ocean (purple lines) and FASTEM-6 (blue lines) for nine equally spaced values of OWS between 5.7 and 36.2 ms^{-1} with all other factors held constant. All simulations use a single mean atmospheric profile, a satellite azimuthal angle of 0° and a satellite viewing angle of 53.1° , a value typical of conical scanning instruments. The frequency sampling resolution is 1 GHz .

In Figure 2.14.1 it is obvious that for higher frequencies (above $\sim 200 \text{ GHz}$), the two models deviate significantly from one another and FASTEM-6 can generate unphysical (negative) emissivity values in some cases. For the third and fourth Stokes components, the FASTEM parameterisation extrapolates at constant value above $\sim 37 \text{ GHz}$ whereas the SURFEM-Ocean behaviour is more realistic at higher frequencies.

Figure 2.14.2 focusses on frequencies up to 200 GHz due to the issues with FASTEM-6 at high frequencies. Differences of up to ~5 K are observed at the highest wind speeds in vertically and horizontally polarised channels, and even larger differences can occur at very low frequencies.

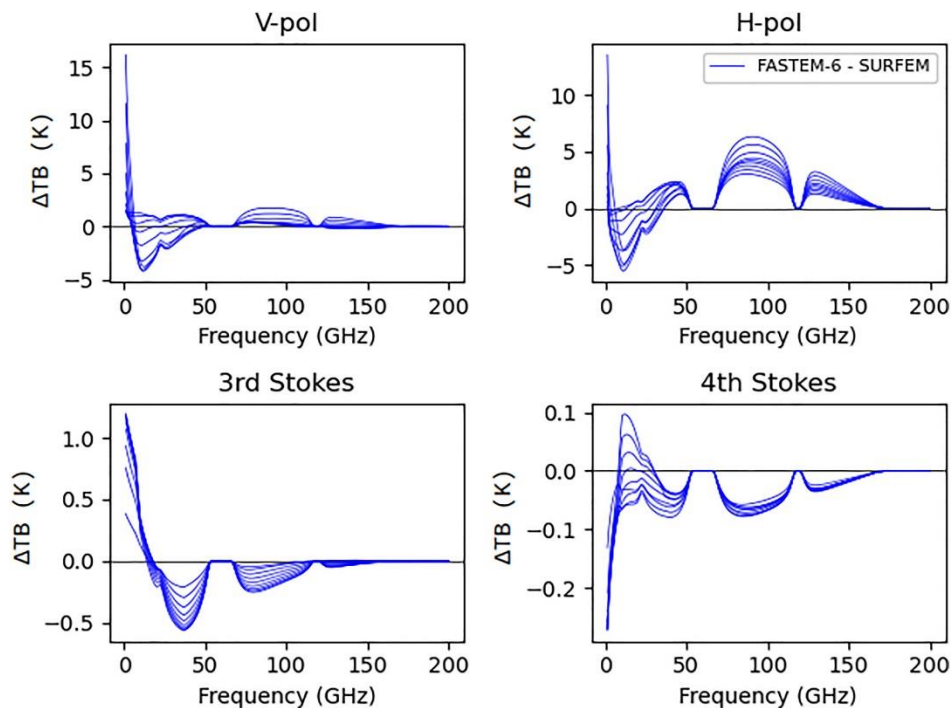


Figure 2.14.2: Differences in RTTOV simulated brightness temperatures between FASTEM-6 and SURFEM-Ocean for nine equally spaced values of OWS between 5.7 and 36.2 ms^{-1} with all other factors held constant. All simulations use a single mean atmospheric profile, a satellite azimuthal angle of 0° and a satellite viewing angle of 53.1° , a value typical of conical scanning instruments. The frequency sampling resolution is 1 GHz.

2.15 Heterogeneous surfaces

RTTOV v13 and earlier assumed the surface is homogeneous within the satellite footprint. Each input profile is associated with one surface type with a single set of near-surface (“2m”) and skin properties, and per-channel emissivities and reflectances.

RTTOV v14 introduces a heterogeneous surface capability whereby the input profiles may be associated with multiple surfaces. Each surface has its own surface type, its own set of 2m and skin properties, and independent per-channel emissivities and reflectances. It also has an associated area coverage fraction. All profiles have the same number of surfaces,

$nsurfaces$, specified by the user. The user specifies the area fraction for surfaces 1, 2, ..., $nsurfaces-1$, and RTTOV automatically computes the final fraction such that the sum of all fractions is 1. Thus, when assuming homogeneous surfaces (i.e., $nsurfaces=1$), the user does not need to specify any surface fraction. When assuming heterogeneous surfaces, a profile may still be associated with a homogeneous surface by setting the corresponding area fraction to 1, and all other fractions to 0.

The intention behind this capability is primarily to allow for better characterisation of surfaces around coastlines (a mixture of land and sea) and around the edges of sea-ice (a mixture of sea and sea-ice, or potentially land, sea, and sea-ice near coastlines). Typically, there would be 2 or 3 surfaces associated with each profile in the heterogeneous case, but RTTOV imposes no upper limit on the number of surfaces. This capability allows sea-ice fraction to be retrieved as part of the state vector in retrieval or assimilation applications, for example.

In this initial implementation, the surface properties are combined, and just one radiance calculation is performed per profile. This was done for efficiency, and this approach is discussed further below.

The $near_surface(:)$ and $skin(:)$ members of the RTTOV profile data structure are arrays of size $nsurfaces$ allowing independent specification of these variables for each surface. The $emis_refl(:)$ argument to the main RTTOV routines is also an array of size $nsurfaces$ and this data structure is used for input/output of emissivity, reflectance, and other per-channel surface-related information.

The combined surface leaving radiance for thermal channels is computed as shown in equation 2.15.1:

$$L_{surf} = \sum_{i=1}^{nsurfaces} f_i \varepsilon_i B(Tskin_i) \quad (2.15.1)$$

where B is the Planck function, and f_i , ε_i , $Tskin_i$ are the surface fraction, emissivity, and skin temperature associated with surface index i respectively.

The combined surface BRDF and diffuse reflectance are computed according to equation 2.15.2:

$$x_{surf} = \sum_{i=1}^{nsurfaces} f_i x_i \quad (2.15.2)$$

where x_{surf} is the total BRDF (or diffuse reflectance), and f_i and x_i are the surface fraction and BRDF (or diffuse reflectance) for surface index i respectively.

When using the RTTOV *lambertian* option (R11REP2013, R13REP2020), it is applied to all surfaces associated with each profile. Whether each individual surface is treated as

specular, Lambertian, or a mixture of the two can be controlled using the *specularity*(:) members of the *emis_refl*(:) structure array. For heterogeneous surfaces with the *lambertian* option, an additional diffuse reflectance is computed:

$$r_{surf,spec} = \sum_{i=1}^{nsurfaces} f_i s_i r_i \quad (2.15.3)$$

where r represents diffuse reflectance, f is the surface fraction, and s is the specularity. From equation 2.15.2 we have the usual specular diffuse reflectance r_{surf} . Equation 2.15.3 is the diffuse reflectance weighted by the specularity parameter s_i for each surface, $r_{surf,spec}$. When computing the downwelling radiance contribution to the TOA radiance for the *lambertian* option, r_{surf} is the reflectance used for the downwelling specular radiance, and $(r_{surf} - r_{surf,spec})$ is the reflectance used for the downwelling Lambertian radiance. It should be noted that for heterogeneous surfaces ($nsurfaces > 1$) with the *lambertian* option, there is no clear relationship between the *dnclear* (downwelling radiance arriving at the surface) and *refldnclear* (downwelling radiance reflected by the surface) members of the *rttov_radiance2* secondary radiance output structure unlike in the case of fully specular or homogeneous surface ($nsurfaces=1$) simulations.

The alternative approach to the treatment of heterogeneous surfaces is to carry out one radiance calculation per surface and to combine the resulting radiances weighted by the corresponding surface area fractions. For clear-sky simulations where only surface emissivity, surface reflectance, and skin temperature vary among the surfaces associated with a given profile, there is no difference between the “combined-surface” and “multi-radiance” approaches because the solution of the radiative transfer equation in the non-scattering case is linear in these variables. This means that it doesn’t make a difference if the properties are linearly combined and the RT equation is solved once, or if the RT equation is solved per surface and the radiances are linearly combined. The former approach, implemented in RTTOV v14, is more computationally efficient.

If the 2m temperature or 2m water vapour vary between surfaces, then the differences between the two approaches are of order mK (not shown) because these influence the optical depth in the near-surface layer (see [section 2.1](#)) and so have a non-linear impact on top-of-atmosphere radiance. However, the approximation due to the combined-surface approach is negligible in this case.

For scattering cases, the radiance solution is no longer linear in the surface variables and so the errors due to the combined-surface approach are larger. To illustrate this, hydrometeor scattering simulations have been carried out using every 25th profile from the NWP SAF 25000 diverse profile set on 137 levels (Eresmaa and McNally, 2014 & 2016), for ATMS, FCI IR channels, and FCI VIS/NIR channels using the thermal and solar scattering solvers implemented in RTTOV v14. Simulations are carried out with two surfaces per profile, one land and one sea, and setting the land fraction to 0.25, 0.5, and 0.75. These

are compared with radiances computed by doing the corresponding land-only and sea-only cases, and linearly combining the resulting radiances weighted by the corresponding surface fractions. Satellite and solar zenith and azimuth angles are varied among the profiles so that many viewing and solar geometries are tested. The land surface emissivity/BRDF atlases (TELSEM2 for ATMS, CAMEL climatology for FCI IR, BRDF for FCI VIS/NIR) for January are used for the land surface emissivities and BRDFs. SURFEM-Ocean (ATMS) and IREMIS (FCI IR) are used for sea surface emissivities, and the ocean BRDF model is used for FCI VIS/NIR channels. Skin temperature and near-surface variables are the same for both surfaces. The *col_threshold* option was set to 1.E-5 for efficiency, and Rayleigh multiple scattering is enabled. All other RTTOV options take their default values. Comparisons have been made for two cases: first where the optical properties are identical over land and sea surfaces, and second where they differ for land and sea.

The plots in Figure 2.15.1 show statistics (mean, standard deviation, maximum absolute difference) for the multi-radiance minus combined-surface radiances for the various solvers. In this case, the hydrometeor optical properties are identical over land and sea in all cases. For ATMS, the results indicate a maximum error of order 0.1 K in the surface sensitive channels, while the mean and standard deviation are an order of magnitude smaller than that. This indicates that the combined-surface approximation is reasonable in this case. For the FCI IR channels, the errors are somewhat larger, but the mean and standard deviation are typically less than ~0.1 K for all three thermal solvers which is modest compared to other errors in scattering simulations. For the FCI VIS/NIR channels with the DOM solver (R12REP2017), the mean and standard deviation are around 0.01, but the maximum differences are large, especially for the case with land fraction equal to 0.5. As described in [section 2.8.2](#), the MFASIS-NN solver provides an exact solution in this case, so the differences are negligible as in the clear-sky case (not shown).

Figure 2.15.2 shows similar plots for FCI IR and VIS/NIR channels for all solvers where the CLW Deff optical properties are used for cloud liquid water. The parameterisation of cloud liquid water particle size is different for land and sea profiles meaning the optical properties differ over land and sea. This results in larger differences due to the combined-surface approximation compared to the multi-radiance calculation.

The maximum errors for FCI IR channels are roughly doubled in this example compared to Figure 2.15.1. For the FCI VIS/NIR channels there are now small differences to the multi-radiance solution for MFASIS-NN and there is a corresponding small increase in the errors for the DOM solver.

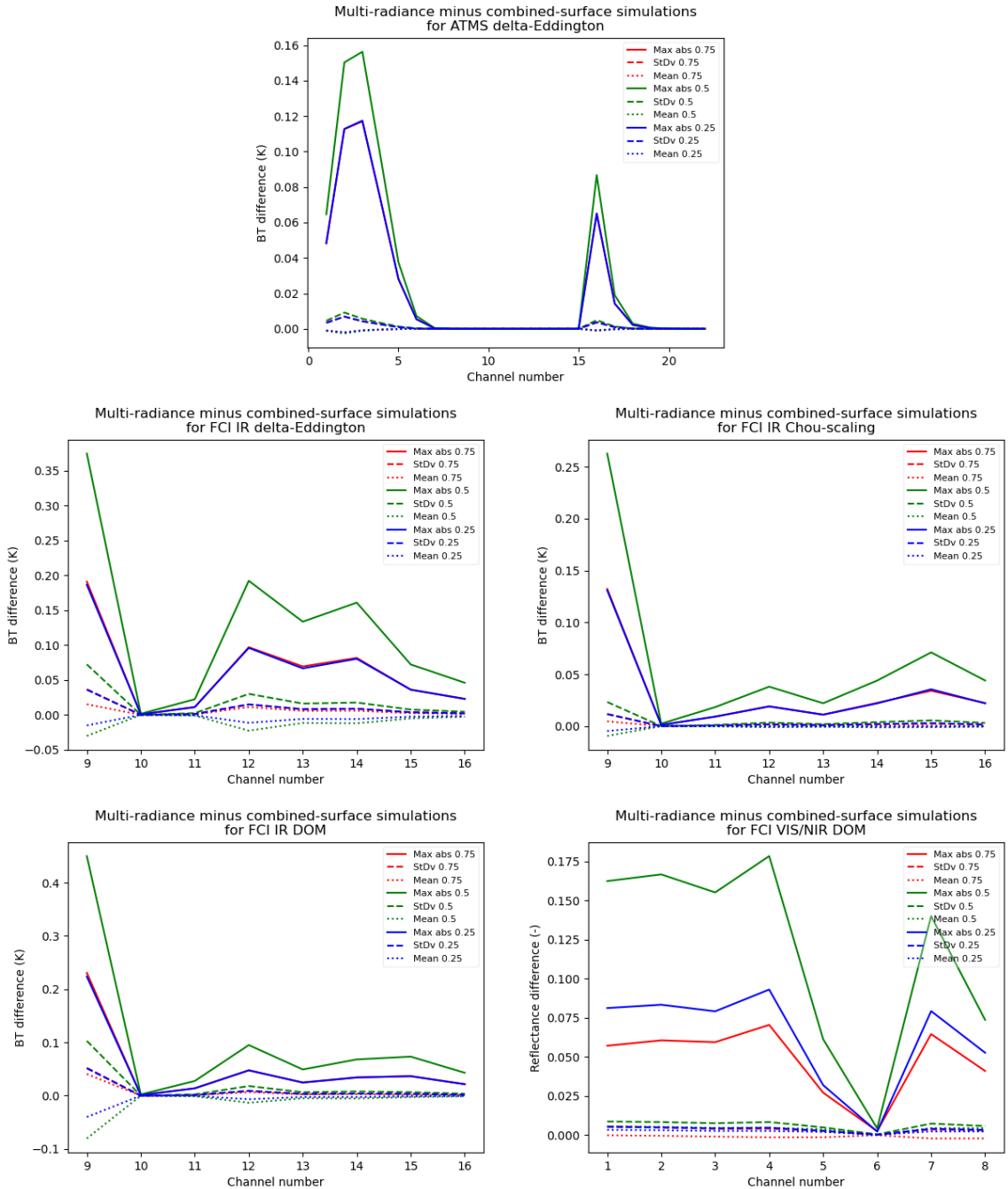


Figure 2.15.1: statistics of radiance differences from the multi-radiance minus combined-surfaces approaches for ATMS, FCI IR channels, and FCI VIS channels, for different solvers. Statistics are plotted for land fractions of 0.25, 0.5, and 0.75. The same optical properties are used over land and sea surfaces.

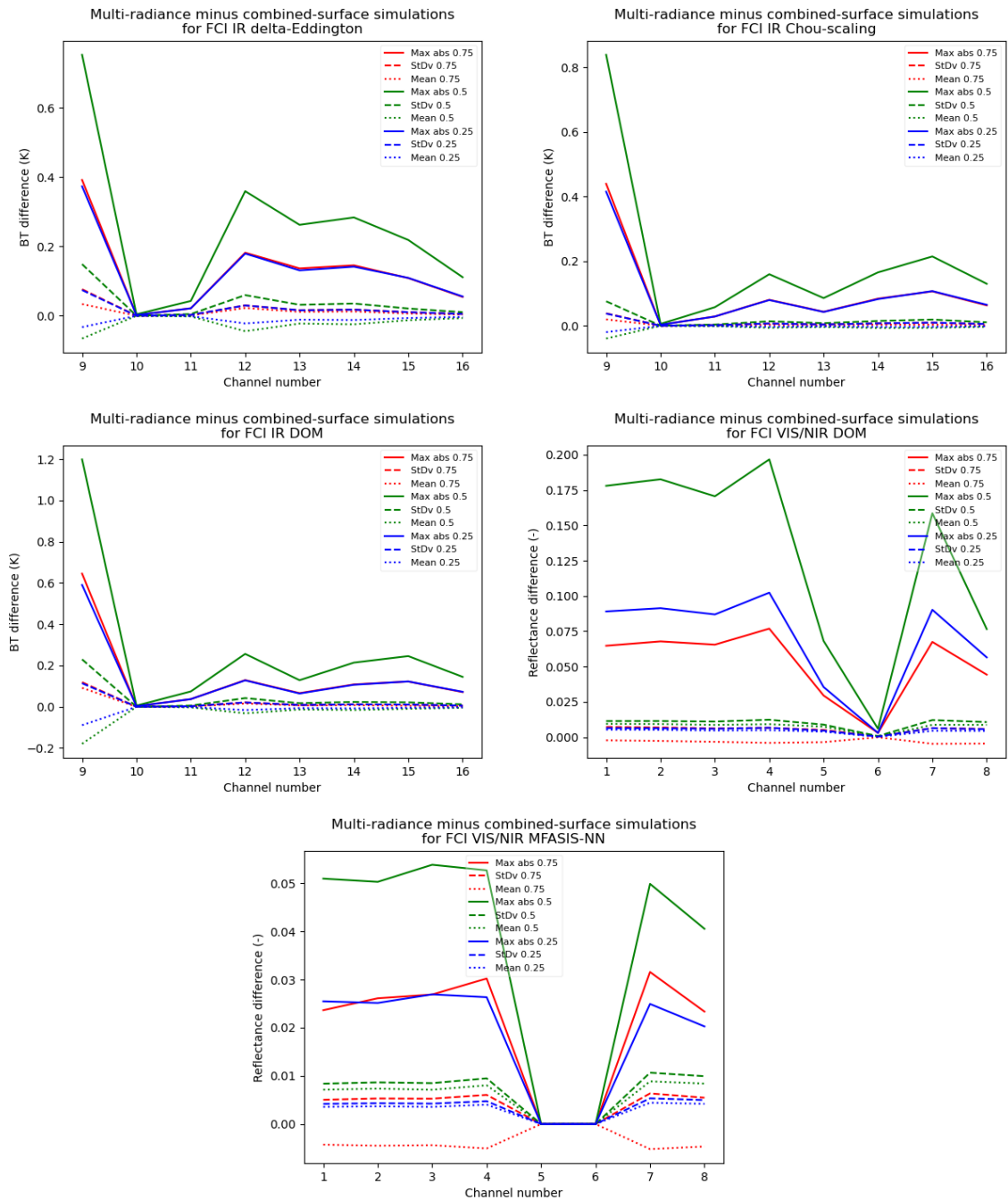


Figure 2.15.2: statistics of radiance differences from the multi-radiance minus combined-surfaces approaches for FCI IR channels, and FCI VIS channels, for different solvers. Statistics are plotted for land fractions of 0.25, 0.5, and 0.75. In this case the cloud liquid water optical properties differ over land and sea surfaces. Note that FCI channels 5 and 6 are not yet supported by MFASIS-NN.

Overall, while maximum differences due to the combined-surface approximation can be large, the typical errors shown by the mean and standard deviation are relatively small compared to the other errors expected in scattering simulations. Carrying out multiple radiance calculations per profile would be considerably more computationally expensive than the approximate approach implemented in RTTOV v14. There are additional questions for hydrometeor scattering simulations in terms of how cloud overlap should be treated with respect to the different surfaces. For example, should there be more cloud over land than over sea or vice versa? How can the user specify this? And how might this interact with different cloud types (optical properties) over different surfaces? The multi-radiance approach may be considered in a future version of RTTOV in order to mitigate the errors illustrated above.

2.16 Updates to treatment of diffuse reflectance

In RTTOV, the surface diffuse reflectance is used for all downwelling radiation emitted or scattered by the atmosphere. It applies to all channels, both thermal and solar. In RTTOV v12 and earlier, this quantity was computed internally and was not provided as an output to users. In RTTOV v13, the diffuse reflectance computed by RTTOV could be obtained for all channels (thermal and solar) by passing the *reflectance* argument which otherwise was only required/relevant for solar simulations. It was also possible to specify input values for the diffuse reflectance in visible/near-IR channels only (wavelengths below 3 μm), but only if the corresponding BRDF value was also being input by the user.

By contrast, the user has always had full control over the surface emissivity and, for solar simulations, the surface BRDF: users can choose to input values or have RTTOV provide values independently for each channel/profile being simulated. The values used by RTTOV (whether input by the user or computed internally) are available as outputs.

RTTOV v14 gives diffuse reflectance the same status: it can now optionally be input by the user in any channel/profile independently of the emissivity and BRDF, and the value used (whether input or computed by RTTOV) is available as an output.

In most cases it is recommended to let RTTOV compute values for the diffuse reflectance, especially for thermal channels (wavelengths greater than 3 μm). For thermal channels, the diffuse reflectance is usually computed as $(1 - \text{emissivity})$ representing specular reflectance, but for the microwave sea surface emissivity models this is modified according to the atmospheric transmittance to account for the non-specular nature of the reflectance.

For visible/near-infrared channels (wavelengths less than 3 μm), the value represents a BRDF multiplied by π . For sea surfaces, RTTOV interpolates values from USGS water

reflectance spectra (Kokaly *et al*, 2017; ocean or coastal according to whether the profile water type is set to ocean or fresh water), and for land/sea-ice surfaces the value is set to $BRDF \cdot \pi$. This is a difference to RTTOV v13, where input/output values of diffuse reflectance for visible/near-infrared channels were BRDF-like.

In RTTOV v13, for sea surfaces in solar channels (wavelengths less than 5 μm), the interpolated USGS water reflectance spectrum value is divided by π and added to the BRDF computed from the ocean sun glint BRDF model (when the user requests that RTTOV computes the BRDF). This is done because the sun glint model does not account for sub-surface scattering at all and underestimates reflectance away from the sun glint region. One key difference in RTTOV v14 is that it is the diffuse reflectance (whatever value that is) divided by π that is added to the sun glint model BRDF. This means that if the user has information about ocean colour, for example, they may wish to input values for the diffuse reflectance while allowing RTTOV to compute the sun glint BRDF. Then the sun glint BRDF will also include the same ocean colour information for consistency. If the user requests that RTTOV computes the diffuse reflectance, then the sun glint BRDF calculation is the same in v13 and v14 because RTTOV uses the USGS spectra for the diffuse reflectance.

In addition to the above change, the USGS reflectance datasets have been updated to the latest versions and have been extended in spectral range. Previously they were stored for wavenumbers in the range 4000-25000 cm^{-1} and in v14 the range is now 3650-50000 cm^{-1} . As before, constant value extrapolation is used for values outside this range. This change primarily affects the diffuse reflectance over sea surfaces for simulations at wavenumbers above 25000 cm^{-1} (wavelengths below 0.4 μm). [Section 3.1.3](#) illustrates the impact of this for GOME-2.

2.17 Updates to land surface emissivity/BRDF atlases

2.17.1 Interface to CAMEL v3 atlases

RTTOV v14 now includes the latest update of the NASA MEASURES CAMEL (Combined ASTER and MODIS Emissivity over Land) V003 IR land surface emissivity atlas (Borbás *et al*, 2023a&b). The first two atlases, the University of Wisconsin UWIREmis atlas (first included in RTTOV v10, Borbás *et al*, 2010), and the CAMEL 2007 atlas (first included in RTTOV v12.1, R12REP2017) are based on data from the selected year of 2007. This single year was chosen due to its high quality and better representation of the CAMEL emissivity climatology mean than other individual years. Upon availability of the CAMEL V002 product (2000-2016), the third emissivity atlas called CAMEL CLIM was made available in RTTOV v12.3 and is based on the actual full record of CAMEL V002 coefficient data (Hook, 2017) with an advanced snow correction.

The new CAMEL V003 IR land surface emissivity atlas in RTTOV v14 is being offered to run any month and year between 2003 and 2021; however the users need to download the necessary CAMEL V003 datafiles from the NASA LP DAAC (<https://lpdaac.usgs.gov/news/lpdaac-release-of-nasa-measures-camel-5-km-v3-products/>). The monthly climatology of the CAMEL V003 is also offered for RTTOV v14. It was calculated for the 19 years (2003 to 2021, using only Aqua/MODIS input data) on a spatial grid of 0.05 degrees (about 5 km x 5 km). Additionally, the mean and the variance of the IR emissivity have been updated based on the CAMEL V003 data and provided with a spatial resolution of 0.25x0.25 degrees similar to the CAMEL CLIM V002 module. More details about the methodology to create the climatology can be obtained from Loveless (2022). This climatology can be degraded to NWP model resolutions to make it suitable for a first guess to the land surface emissivity for variational data assimilation of infrared sensor data.

Differences between CAMEL V002 and CAMEL V003 are illustrated in Figures 2.17.1 and 2.17.2. Aside from the *time coverage change from 2000-2016 to 2000-2021*, the most significant update in CAMEL V003 is the *use of the latest calibrated MODIS products*, which are used as inputs to the CAMEL algorithm. The updated Collection 6.1 MODIS MYD11C3 Band 20, 22, and 23 data was used in combination with Band 29, 31, and 32 of the new MYD21C3 product (Hulley and Hook, 2021). Changes seen in the 3.6-4.0 μm region are due to the calibration update from Collection 4.1 to 6.1 of MYD11 Bands 20, 22, and 23, and changes over the 8-9 μm Reststrahlen band relate to the algorithm change from the MYD11 (CAMEL V002 input) day-night algorithm to the MYD21 (CAMEL V003 input) temperature and emissivity separation (TES) algorithm. Figure 2.17.1 illustrates the mean and the standard deviation (square root of the covariance diagonal) of CAMEL V002 vs. V003 at 4 μm for August. The CAMEL V003 standard deviation has been reduced over many areas of the globe, for example, in desert and mountainous regions. Still, it remains high in specific areas, such as the Sahel band, which reflects the realistic variation of the grassland over time.

Figure 2.17.2 shows an example of the IGBP type called Open Shrubs. CAMEL emissivity at each hinge point is averaged over all the Open Shrubs pixels for each month. The combination of Col 6.1 MOD11 and MOD21 for CAMEL V003 shows fewer unphysical trends and features; hence, the uncertainties are significantly reduced and smoothed out over time due to the better-calibrated input MODIS data.

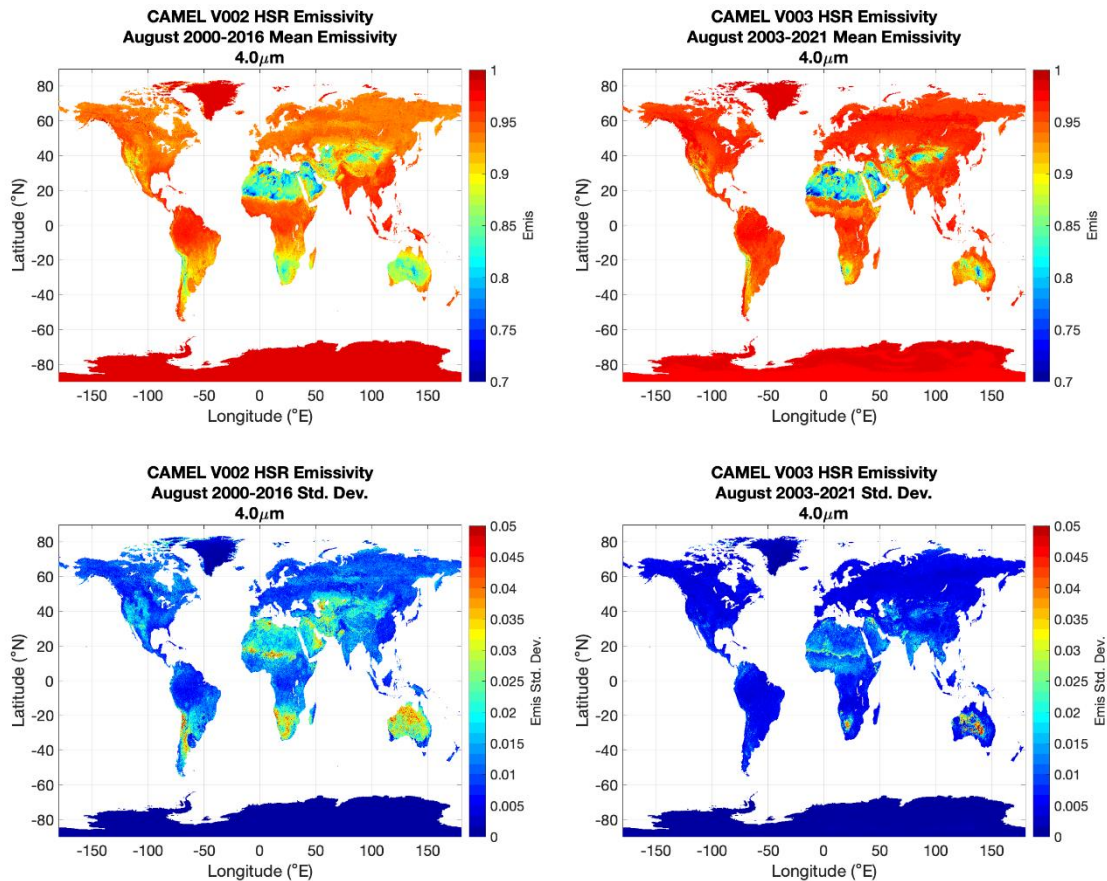


Figure 2.17.1: The mean (top) and standard deviation (bottom) of CAMEL V002 (left) vs. V003 (right) climatology emissivity at 4 μm for August. Statistics for CAMEL V002 were calculated between 2000 and 2016 (using Terra/MODIS data for the first three years) and for CAMEL V003 between the years 2003 and 2021 (using only Aqua/MODIS products).

Figure 2.17.3 shows examples of climatological HSR emissivity spectra at select case sites used to validate and assess the CAMEL product. These sites include the Namib Desert (quartz), Yemen (carbonate), Congo Forest, Atmospheric Radiation Measurement (ARM) Southern Great Plains (SGP) (grassland/cropland), Greenland (snow/ice), Park Falls WI (evergreen forest with partial snow cover), and a Rocky Mountain site over Mt. Massive (snow/mountainous site). The Namib Desert (top panel) spectral features around 8-9 μm is the quartz signature, while Yemen (2nd panel from top) spectral features at \sim 6.5 and 11 μm is the carbonate signature.

Overall, V003 is highly recommended over V002 data since it includes all the features of V002 but provides a longer data record based on the latest calibration of the input MODIS data. The CAMEL V3 emissivity - based on the cross-talk corrected Col6.1 MODIS data - shows fewer unphysical trends; hence, the uncertainties are significantly reduced.

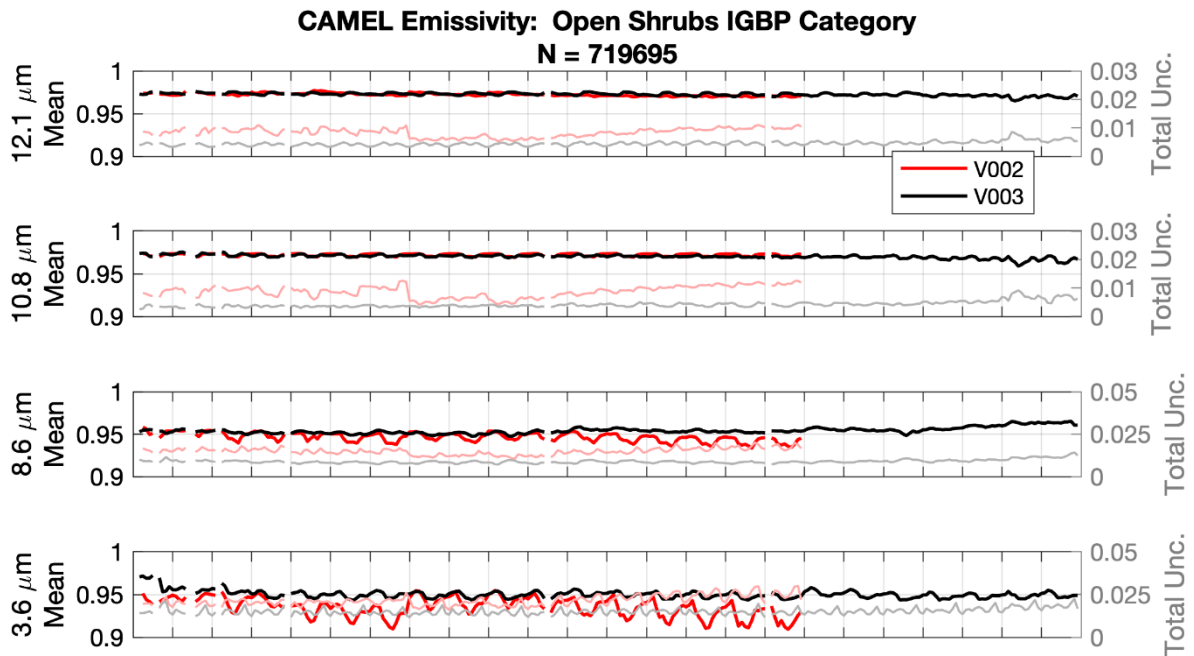


Figure 2.17.2: Comparison of V002 (red) vs. V003(black) CAMEL monthly product emissivity time-series (between 2000 and 2024) for IGBP category Open Shrubs for four selected hinge points. The solid line stands for the mean emissivity, while the faded lines are the total uncertainties.

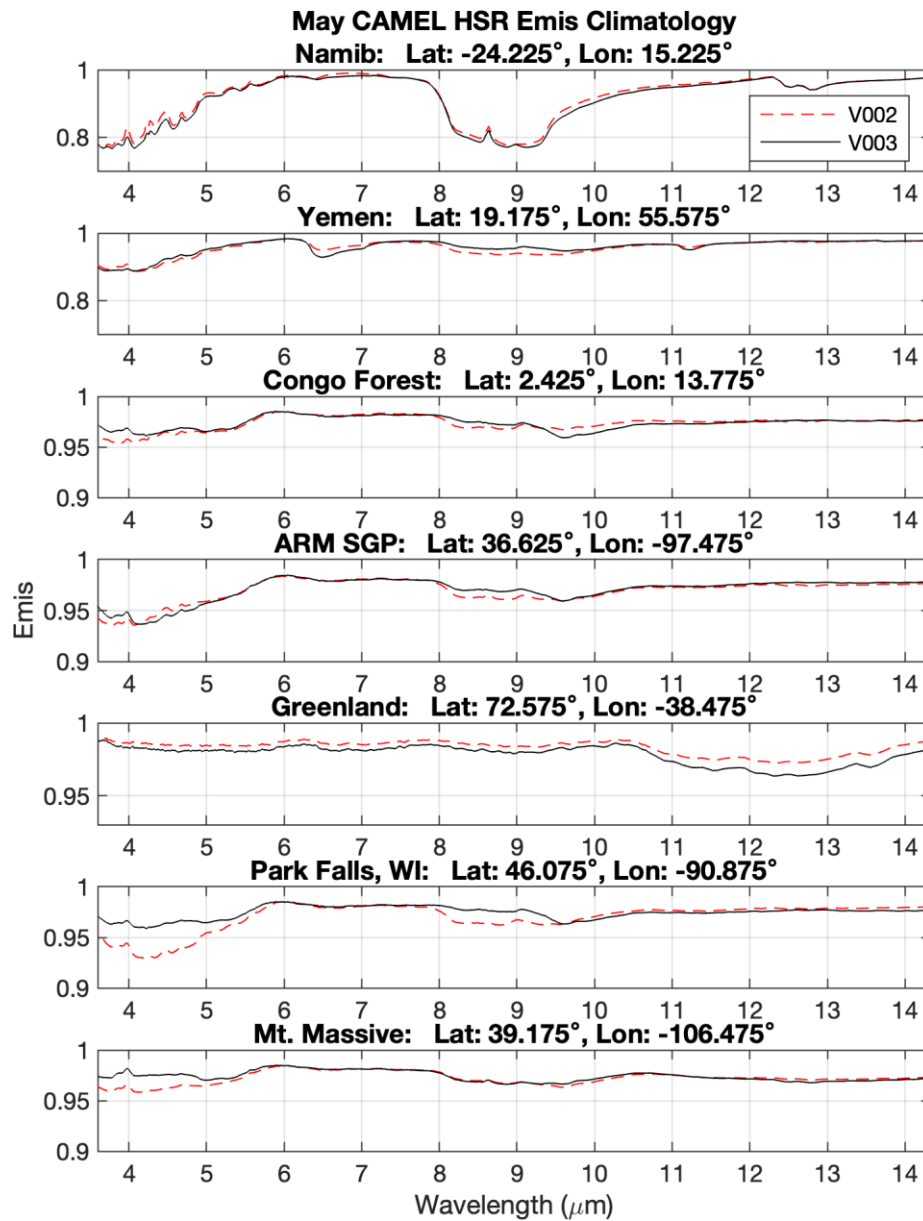


Figure 2.17.3: CAMEL V2 (red) and V3 (black) climatology HSR emissivity spectra overlaid for May at selected sites (top to bottom) Namib Desert (quartz), Yemen (carbonate), Congo Forest, ARM SGP site (grassland/cropland), Greenland (snow/ice), Park Falls WI (snow/evergreen forest), Mt. Massive (snowy mountainous) site.

2.17.2 Option to return nearby emissivity/BRDF values

When obtaining emissivity or BRDF values from the emissivity or BRDF atlases provided for use with RTTOV, the atlas may return no valid emissivity value for certain locations where the user believes that the surface type is land. This most often occurs around coastlines or close to in-land water bodies and may result from the resolution of the atlas. In some cases, users would like a reasonable alternative emissivity (or BRDF) as a “first guess”: this situation may be common in the context of retrievals or data assimilation.

RTTOV v14 introduces an option in the IR emissivity and BRDF atlases for users to specify a maximum distance argument. If no valid land surface value is found at the given location, the code searches the atlas in the neighbouring grid boxes within the specified distance of the original location and returns the first valid value (if any) found in this search.

For reasons of efficiency the search algorithm *does not necessarily* return the *closest* valid emissivity/BRDF value, but it returns one within the given search radius where a valid value exists.

The search works by looking in concentric regular latitudinal/longitudinal “square rings” around the grid box containing the initial location with incrementally increasing displacement from the original central grid box. It searches first the rows of grid points on the latitudinal boundaries of the ring, and then the columns of grid points on the longitudinal boundaries. It starts from the centre of each row or column and incrementally moves outwards to the ends of the row/column. It returns the first grid box encountered that contains a valid emissivity/BRDF within the specified search radius. To curtail the search process, latitudinal bands are excluded during the search when distances exceed the search radius. Through this method the returned grid point, while not guaranteed to be strictly the nearest one with a valid value, it will be near to it, as the search moves incrementally away from the starting location.

Searches near the poles do not go “over” the pole. There is no problem at the south pole as it is covered by land. At the north pole this would only cause valid grid points to be missed if the search radius was very large which is not recommended. An upper limit of 100 km is imposed for the search radius in the code.

2.18 Generalisation of dynamic emissivity retrieval outputs

RTTOV v12.2 introduced an optional argument to RTTOV-SCATT that, if present, is populated with data that can be used together with the corresponding observed brightness temperatures to carry out surface emissivity retrievals. An ancillary subroutine that carries

out the retrieval calculation is provided with RTTOV. This follows the methodology of Baordo and Geer (2016).

RTTOV v14 provides the same capability and generalises it to clear-sky simulations as well as hydrometeor scattering simulations with any cloud overlap parameterisation. It is now applicable to infrared sensors as well as microwave sensors. It is currently available only for the fast thermal scattering solvers (Chou-scaling and delta-Eddington) implemented in RTTOV v14.

From a user perspective, the contents of the *rttov_emis_retrieval_terms* data structure are not especially relevant. They are documented in the RTTOV v14 user guide, but the user simply needs to pass the corresponding argument into the call to the RTTOV direct model which populates it, and then pass the data structure into the *rttov_emissivity_retrieval* subroutine. The arguments to this subroutine are documented in the user guide and include information on which channels were simulated for each profile, the RTTOV coefficients data structure, the emissivity retrieval terms structure (populated by a call to *rttov_direct*), and the observed brightness temperatures corresponding to the RTTOV simulations. The primary output is an array containing the retrieved emissivities for each channel and profile.

The retrieved emissivity is calculated using a generalisation of equation 7 in Baordo and Geer (2016):

$$\varepsilon_{\text{ret}} = \frac{T_b - \sum c_i T_i^{\uparrow} - \sum c_i T_i^{\downarrow} \Gamma_i}{T_s \sum c_i \Gamma_i - \sum c_i T_i^{\downarrow} \Gamma_i}$$

where each summation is over cloud columns with index i . The clear column is index 0, and this is the only column for clear-sky simulations. Two column cloud overlap schemes (such as that implemented in RTTOV-SCATT, and now in RTTOV v14 – see [section 2.6](#)) have just one cloudy column in addition to the clear column. The RTTOV implementation of maximum/random overlap can generate many cloud columns. In all cases c_i represents the weight corresponding to cloud column i . The c_i sum to 1 over all cloud columns. In the above equation, T_b is the observed radiance, T_i^{\uparrow} is the upwelling atmospheric emitted radiance at the top of atmosphere for cloud column i , T_i^{\downarrow} is the downwelling atmospheric emitted radiance (plus cosmic microwave background contribution for microwave sensors) at the surface for cloud column i , and Γ_i is the total atmospheric transmittance for cloud column i . Finally, T_s is the Planck radiance equivalent to the surface skin temperature. This emissivity retrieval capability is not compatible with heterogeneous surfaces (see [section 2.15](#)).

The *rttov_emissivity_retrieval* routine also optionally allows for per-channel retrieval of skin temperature. In this case, emissivity values $\varepsilon_{\text{user}}$ for each channel and profile must be specified to use in this retrieval. The retrieved skin temperature for each channel is only

computed if $\sum c_i \Gamma_i > 0.3$. The black body radiance equivalent to the surface skin temperature, L_{surf} , is computed as:

$$L_{\text{surf}} = \frac{T_b - [(1 - \epsilon_{\text{user}}) \sum c_i T_i^{\downarrow} \Gamma_i] - \sum c_i T_i^{\uparrow}}{\epsilon_{\text{user}} \sum c_i \Gamma_i}$$

The Planck function is then used to convert L_{surf} to the retrieved skin temperature.

2.19 Updated NLTE coefficients

Updated NLTE coefficients have been generated for RTTOV v14 based on new line-by-line (LBL) spectroscopy and a bug identified in the processing of the training profiles has been fixed. The range of NLTE capable sensors has been extended from IASI, CrIS, and AIRS to also include IASI-NG and MTG-IRS. See the RTTOV v12 Science and Validation Report (R12REP2017) for details of the coefficient scheme, and Matricardi *et al* (2018) for the scientific basis.

Figure 2.19.1 shows the total radiance differences in IASI NLTE channels between the updated and previous coefficients, for two different solar and viewing geometries. In general differences are lower than 0.15 K which is around 1% of the overall NLTE effect itself.

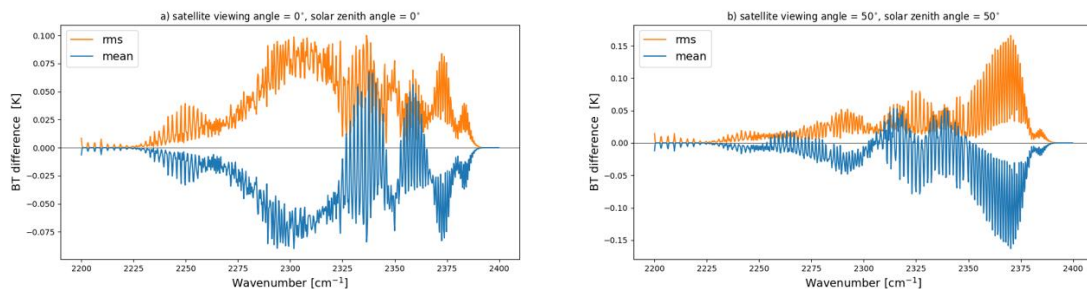


Figure 1.19.1. TOA BT differences between updated NLTE coefficients and the previous coefficients for the IASI instrument for a) satellite viewing angle and solar zenith angle of 0° , b) satellite viewing angle and solar zenith angle of 50° . The mean and root mean square statistics are generated from 5000 NWP SAF profiles with maximal temperature variability on 137 model levels.

The spectroscopy has been updated from LBLRTM 12.2 to LBLRTM 12.8 to bring it in line with the version used by all other non-NLTE channels. This change incorporates an update across almost all spectral lines to HITRAN 2012 (Rothman *et al*, 2013) and gas broadening parameters, such as CO_2 broadened by H_2O , have also been implemented. The MT-CKD continuum has also been updated to version 3.2, although the water vapour continuum has

a negligible effect on wavenumbers between 2200 – 2400 cm^{-1} . The difference due solely to the spectroscopy update is shown in Figure 2.19.2, and most differences are less than 0.075 K.

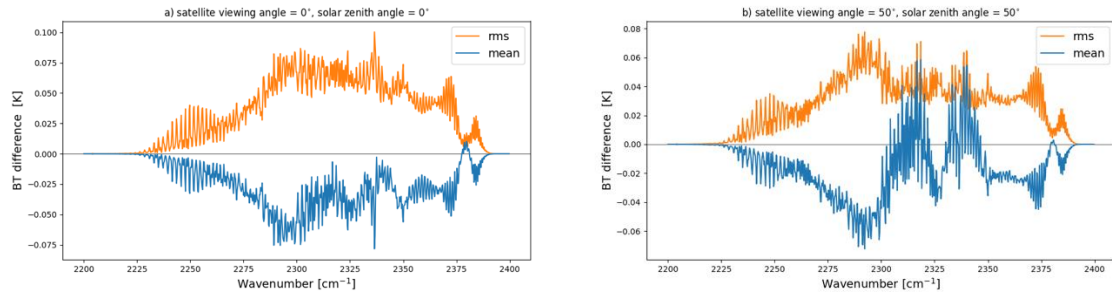


Figure 2.19.2. TOA BT differences between NLTE coefficients generated with LBLRTM 12.8 and LBLRTM 12.2 line-by-line databases for the IASI instrument for a) satellite viewing angle and solar zenith angle of 0° , b) satellite viewing angle and solar zenith angle of 50° . The mean and root mean square statistics are generated from 5000 NWP SAF profiles with maximal temperature variability on 137 model levels.

A minor bug has been identified in the input profiles, where no levels above 100 km were being considered for the NLTE calculations, and coincidentally levels at unfeasibly high altitudes were being considered for the LTE calculations. These two errors have the effect of cancelling each other out and the resulting bias compared to the corrected coefficient is minimal, as can be seen in Figure 2.19.3. In general, the mean difference is below 0.12 K, only slightly larger than the effect of the spectroscopy update.

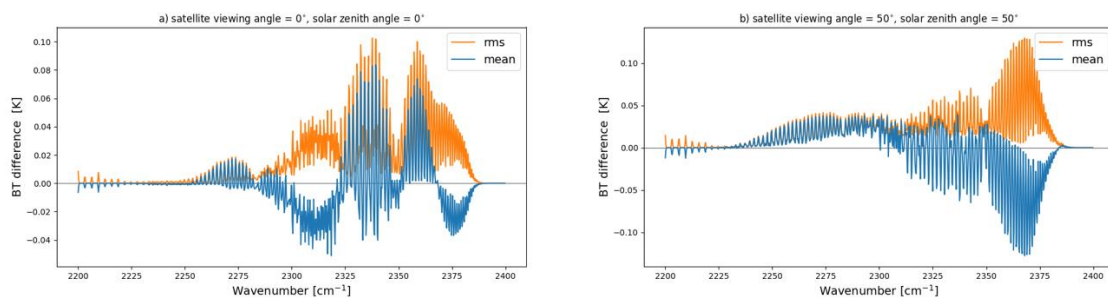


Figure 2.19.3. TOA BT differences between NLTE coefficients with and without the NLTE bug, both generated with LBLRTM 12.8 for the IASI instrument for a) satellite viewing angle and solar zenith angle of 0° , b) satellite viewing angle and solar zenith angle of 50° . The mean and root mean square statistics are generated from 5000 NWP SAF profiles with maximal temperature variability on 137 model levels.

Validation statistics for the three new NLTE coefficients IASI, IASI-NG, and MTG-IRS are shown in Figure 2.19.4. The statistics for IASI appear very close to the equivalent results presented for the previous coefficient in the RTTOV v12 Science and Validation Report

(R12REP2017, Figure 27). Statistics for IASI-NG are similar in overall shape but slightly worse due to the higher channel resolution, which is double that of IASI. MTG-IRS only covers the first quarter of the NLTE waveband and statistics are much higher than the other two instruments due to the increased coverage of satellite view. As the satellite is geostationary it is modelled with 14 secants (up to 85.2°) instead of 5 (up to 60°), the latter being appropriate for the low Earth orbits of IASI and IASI-NG. This introduces a slight degradation in the fast model with respect to LBL as each coefficient must be able to model the higher viewing angles as well as the lower ones. The rms spikes between $2200 - 2225 \text{ cm}^{-1}$ are a feature revealed by fixing the NLTE bug mentioned earlier.

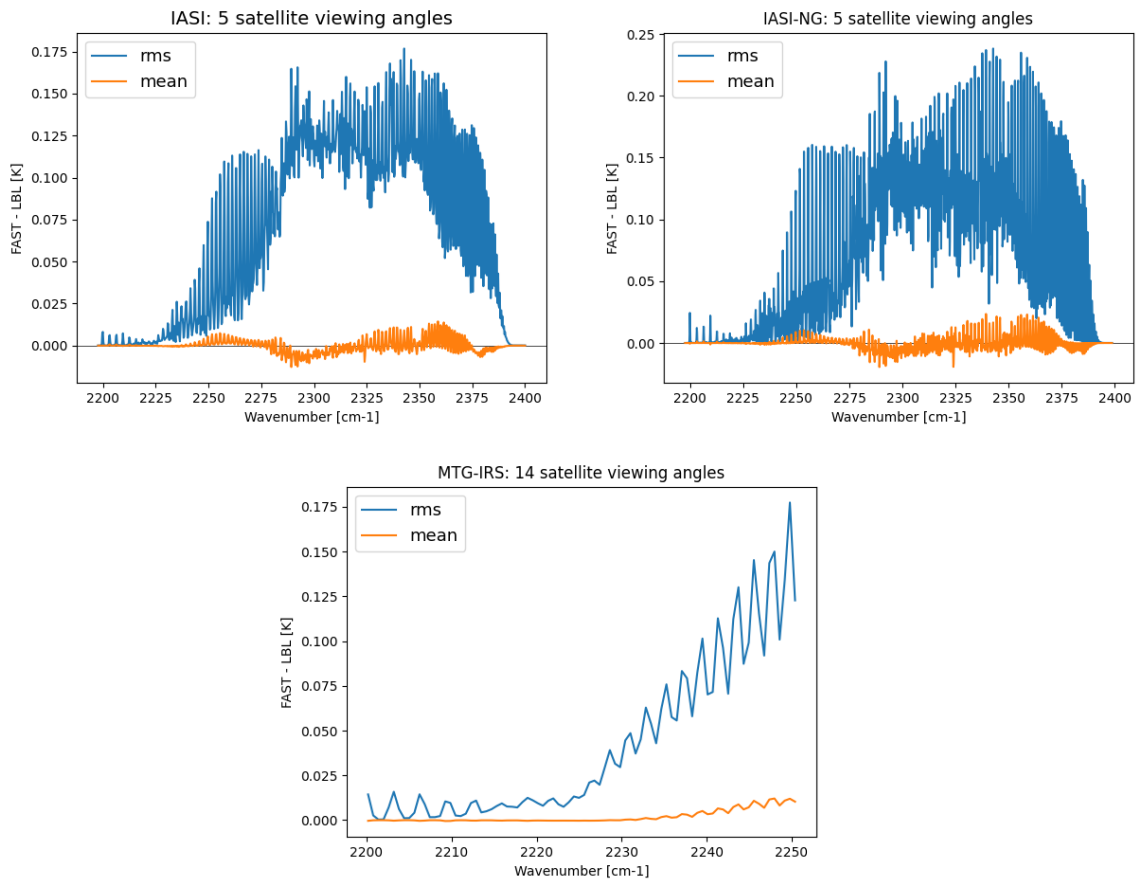


Figure 2.19.4. The mean and rms differences in TOA brightness temperature between the fast NLTE model and the LBL for: top left) IASI, top right) IASI-NG, and bottom) MTG-IRS. The dataset comprises 5 satellite zenith angles (14 for MTG-IRS), 12 solar zenith angles and 48 atmospheric profiles, which is the dependent set. Note the different axis scales.

2.20 PC-RTTOV updates

The PC-RTTOV implementation in RTTOV v14 brings together all PC-RTTOV capabilities implemented in previous versions. PC-RTTOV coefficients for RTTOV v14 are trained over land and sea surfaces and support all variable trace gases available in RTTOV (except SO₂ which has been omitted due to the larger errors in the RTTOV gas optical depth prediction for high SO₂ concentrations). In addition, the PC coefficients are trained for optional use of the NLTE bias correction ([section 2.19](#)), aerosol scattering with the OPAC aerosol species (specifically aerosol indices 1-10 in the OPAC aerosol optical property files), and cloud scattering. Scattering simulations must be run with the Chou-scaling solver. Due to the training methodology, the NLTE, aerosol, and cloud options are mutually exclusive: only one of the three may be activated at one time. The PC coefficients are trained for all capabilities, so there is only one PC coefficient file per sensor supporting all the above functionality.

The RTTOV v14 PC coefficient training uses v13 predictor 7gas optical depth coefficient files. Sea surface emissivities come from the IREMIS model (R12REP2017) unlike previous versions where the PC training used its own sea surface emissivity model. Land surface emissivities are taken from the CAMEL v3 climatology atlas: it is recommended to use this atlas for land surface emissivities when carrying out PC-RTTOV simulations in RTTOV v14.

During the PC coefficient training, various RTTOV options are given specific values. This includes the sea surface emissivity model, atmospheric refraction, the interpolation mode, and others. Unlike previous versions of RTTOV which left it to the user to ensure consistency in most cases, RTTOV v14 silently enforces these options for PC-RTTOV simulations in order to ensure consistency with the PC coefficient training. In cases where RTTOV does not automatically set certain options (because they imply that different inputs must be supplied, for example), an error is thrown so that the user is made aware of the inconsistency. The user guide lists the relevant options and indicates whether RTTOV automatically imposes consistent values or the user must explicitly set the correct value.

For PC-RTTOV simulations, when the RTTOV *apply_reg_limits* option is set to true, input profiles are no longer modified when they exceed the minimum/maximum regression limits. Values falling outside the regression limits are still notified to the user via the *quality(:)* array in the RTTOV output radiance structure.

For RTTOV v14, PC-RTTOV coefficients have been generated for IASI, IASI-NG, and MTG-IRS (this last case with Hamming apodisation on top of light apodisation). The coefficients for each sensor support all capabilities described above.

Full details of PC-RTTOV in RTTOV v14 are given in Matricardi (2024).

2.21 Additional changes to RTTOV inputs, outputs and internal calculations

This section documents changes in RTTOV v14 not discussed elsewhere in this document.

2.21.1 Changes to default option values

The default values of the following options have changed in RTTOV v14 compared to v13:

RTTOV v13 option and default	RTTOV v14 option and default
<i>opts%rt_all%switchrad</i> = .false. (thermal channel AD/K inputs in radiance)	<i>opts%config%adk_bt</i> = .true. (thermal channel AD/K inputs in BT)
N/A (pure-solar channel AD/K inputs in radiance)	<i>opts%config%adk_refl</i> = .true. (pure-solar channel AD/K inputs in reflectance)
<i>opts%interpolation%addinterp</i> = .false. (enable/disable RTTOV interpolator)	<i>opts%interpolation%enable_interp</i> = .true. (enable/disable RTTOV interpolator)
<i>opts%interpolation%interp_mode</i> = 1 (interpolation mode)	<i>opts%interpolation%interp_mode</i> = 4 (interpolation mode)
<i>opts%rt_mw%fastem_version</i> = FASTEM-6 (MW sea emissivity model)	<i>opts%surface%mw_sea_emis_model</i> = SURFEM-Ocean (MW sea emissivity model)
<i>opts%rt_ir%ir_scatt_model</i> = Chou-scaling (scattering solver for thermal IR)	<i>opts%scatt%thermal_solver</i> = delta-Eddington (scattering solver for thermal IR and MW)

RTTOV-SCATT v13 option and default	RTTOV v14 option and default
<i>opts_scatt%interp_mode</i> = 1 (interpolation mode)	<i>opts%interpolation%interp_mode</i> = 4 (interpolation mode)
<i>opts_scatt%fastem_version</i> = FASTEM-6 (MW sea emissivity model)	<i>opts%surface%mw_sea_emis_model</i> = SURFEM-Ocean (MW sea emissivity model)
<i>opts_scatt%cc_threshold</i> = 0.001 (minimum cloud column weight to consider)	<i>opts%cloud_overlap%col_threshold</i> = 0. (minimum cloud column weight to consider)

2.21.2 Changes to RTTOV outputs

In RTTOV v13 and earlier, the *cloudy* member of the radiance output structure contained the 100% overcast radiance for clear-sky simulations employing the simple cloud scheme (based on an opaque, black cloud with user-specified cloud top pressure). For VIS/IR scattering simulations with aerosols and/or clouds, the *cloudy* member was simply set equal to the *total* radiance representing the satellite-seen radiance. In RTTOV v14, the *cloudy* member is now equal in all cases to the cloudy radiance assuming there is no clear column. For hydrometeor scattering two-column cloud overlap schemes and the simple cloud scheme, this is the same as the radiance of the cloudy column. For aerosol simulations without hydrometeors, the cloudy radiance is always zero (the simple cloud scheme is not applied for aerosol simulations).

RTTOV v14 has a new “diagnostic output” data structure. When the user passes the argument of this type to RTTOV it is populated with ancillary data that are computed per-

profile. Currently this includes the altitudes (geometric heights) of the pressure half-levels and pressure full-levels, and the effective cloud fraction.

In RTTOV v13, the pressure level altitudes were output in the RTTOV radiance structure and, for consistency with other outputs in that structure, were provided for every channel simulated even though the values are identical for all channels simulated for a given profile. The output arrays are now sized by the number of profiles. The height of the top-most pressure half-level is omitted because the pressure of the top half-level may be arbitrarily close to 0 hPa in which case the height is not well-defined.

RTTOV-SCATT provided access to the effective cloud fraction computed by the model as part of the default two-column cloud overlap scheme (Geer *et al*, 2009a/b). This output is now provided in the diagnostic output structure and is set equal to one minus the weight of the clear column. This definition generalises the quantity to all cloud overlap schemes and the output is populated for all hydrometeor scattering simulations when the diagnostic output argument is provided by the user.

2.21.3 Capabilities that have been removed

Several previously supported capabilities have been removed from RTTOV v14. These are briefly discussed here.

Surface implicitly lies on bottom pressure half-level.

The changes to the atmospheric profile representation with the surface implicitly on the bottom pressure half-level mean that RTTOV can no longer be run on profile sets defined on fixed pressure levels. The RTTOV internal interpolation was implemented in v9 and since then it has always been recommended to input profiles to RTTOV on the native model pressure levels. NWP models typically have the surface at the bottom of the profile, so this should not be a major issue. As discussed in [section 2.1](#), there are various benefits to this change.

FASTEM-1/2/3/4 and TESSEM2 microwave sea surface emissivity models.

The earlier FASTEM models have been superseded by the new science in the newer versions. FASTEM-6 has been the recommended model for some time, and this has been retained in RTTOV v14 along with FASTEM-5 for continuity. The TESSEM2 microwave sea surface emissivity model was implemented to support sub-mm sensors. It has limitations, such as not being compatible with polarimetric sensors. TESSEM2 has been comprehensively superseded by SURFEM-Ocean which can be used for all microwave sensors supported by RTTOV.

SURFEM-Ocean is the recommended microwave sea surface emissivity model in v14.

JONSWAP wave spectrum option for solar sea BRDF model.

The older JONSWAP wave spectrum option was superseded in RTTOV v12.2 by the Elfouhaily *et al* (1997) option (see R13REP2020) which has improved fit to observations. The older parameterisation has now been removed from RTTOV.

Solar single-scattering solver for clouds/aerosols.

The single-scattering solar solver was inaccurate and has been removed. The DOM solar solver and MFASIS-NN solver will continue to be developed in future releases.

MFASIS-LUT fast visible solver for clouds based on look-up tables.

As discussed in [section 2.8](#), the look-up-table-based version of MFASIS has been superseded by MFASIS-NN, the neural-network-based version.

HTFRTC Principal Components based model.

A bug was discovered in the HTFRTC implementation in RTTOV v13 and resourcing issues mean that it was not possible to investigate and fix the problem. The interface to HTFRTC within RTTOV has been removed due to lack of resource to maintain it.

Deprecated options removed

- *grid_box_avg_cloud* – hydrometeor concentrations are always input to RTTOV v14 as grid box average concentrations. This is consistent with NWP model representations of cloud/hydrometeors.
- *dtau_test* – this switch was originally implemented in to eliminate small discontinuities in the direct model that resulted from ignoring the layer above the surface when it was sufficiently optically thin. In v13.0 it defaulted to false (to eliminate these discontinuities) and was deprecated. RTTOV v14 no longer applies this check on optically thin layers and removes the option.
- *reg_limit_extrap* – when the top-most input pressure level lies below the top coefficient level, the input profiles must be extrapolated to the top of the atmosphere for the optical depth regression. Previously there were two options: constant value extrapolation, or the “regression limit” extrapolation which uses the coefficient training profile min/max limits to extrapolate profiles in a physically plausible manner. This latter behaviour was recommended as it is in general much better than using constant values, and this switch was deprecated. In RTTOV v14 the option has been removed and the improved extrapolation is always applied.

- *spacetop* – by default RTTOV explicitly sets the optical depth of the top-most input pressure level to zero. This ensures that emission is included in addition to absorption from the entire atmosphere between the top of the user profile and the satellite (albeit with an assumption of constant temperature in that layer). Users could turn this off by setting this option to false, but it was never recommended as there is no reason to do so. The option has therefore been removed in v14.

2.21.4 Deprecation of older optical depth coefficients

For RTTOV v13, a very large variety of optical depth coefficient files have been produced. These include files based on the old optical depth predictors (v7, v8, and v9 predictors) and the newer v13 predictors. Files can be available supporting different variable gases, and for hyperspectral sensors, on both 54 and 101 coefficient levels. Users often desire continuity in the coefficients they are using operationally meaning requests are received for all types of coefficient files, not only the latest and/or recommended versions. Some users are still using old versions of RTTOV (v12 and earlier) that do not support the v13 predictors. However, it will not be practical to continue supporting the full range of optical depth coefficient files indefinitely, and the wide variety of coefficients is confusing for users.

After the release of RTTOV v14, only the recommended coefficients for each sensor will be produced as follows:

- **MW sensors:** all 54L, all v13 predictors, all variable O₃, all based on top-hat passbands, and additionally files based on measured spectral responses where available. This means there will be at most two files per sensor.
- **Multi-spectral UV/VIS/IR:** all 54L, all v13 predictors, all variable O₃+CO₂, additional 7gas files for relevant sensors (at most two files per sensor).
- **Hyperspectral UV/VIS/IR:** all 101L, v13 predictors O₃+CO₂, v13 and v9 predictors 7gas for relevant sensors (at most three files per sensor).
- **Special cases:** Zeeman, PMR, SSU PMC shift coefficients to remain available with all being updated to v13 predictors as soon as possible.

All other optical depth coefficient files will be deprecated. If/when users request these we will first respond to see if they can move to the recommended files, and if not, only then provide deprecated files. **Deprecated coefficients will be fully retired after the release of RTTOV v15 such that they will no longer be generated.**

It is planned during the lifetime of RTTOV v14 to develop new RTTOV v14-only coefficients (i.e., not compatible with v13 and earlier) incorporating various scientific improvements with the aim that these will become the standard for both RTTOV v14 and, later, v15.

3. Testing and Validation of RTTOV v14

3.1 Comparison of simulations between RTTOV v13 and RTTOV v14

This section presents differences between RTTOV v13 and RTTOV v14 simulated brightness temperatures, reflectances, and Jacobians for several instruments.

The simulations are run for profiles taken from the NWP SAF diverse profile sets. For clear-sky direct model simulations the 25000 profiles from the 137L diverse profile set (Eresmaa and McNally, 2014 & 2016) are used. For cloud liquid water absorption and hydrometeor scattering simulations, a subset of 10000 profiles from the 137L dataset is used: this comprises the “rcol” and “ccol” sampled sets which are selected for variability in precipitation and cloud condensate. For aerosol simulations, a 20000 profile subset from the 60L MACC profile dataset (Eresmaa *et al*, 2012a&b) is used comprising the profile sets sampled for variability in the various aerosol species. For the temperature and water vapour Jacobian simulations, the 5000 temperature and water vapour sampled subsets of the 137L profile set are used respectively.

Satellite and solar zenith angles, and relative satellite/solar azimuth angles are varied among profiles over their respective valid ranges so that the full range of satellite and solar geometries are included in the simulations.

The same optical depth coefficient files and the same optical properties are used in both v13 and v14. Simulations are configured identically for v13 and v14 using recommended/default settings in RTTOV v14 where these are supported in v13. The only exception is the interpolation mode where the recommended interpolation modes are used in each model: in v14 this is mode 4 in all cases, while in v13 mode 4 is used when there are more input profile levels than coefficient levels, and mode 1 otherwise. Ozone is enabled as a variable gas in the simulations for all coefficient files that support variable ozone.

The plots in this section show statistics of the differences between RTTOV v13 and v14. Plots of average and standard deviation of differences are shown separately to plots of the maximum absolute differences in each case for greater clarity. The most significant source of differences is the change in the profile representation implemented in v14.

3.1.1 MTG FCI comparisons

The simulations in this section use MTG-I1 FCI coefficients based on v13 predictors with variable O₃ and CO₂.

Figure 3.1.1 compares RTTOV v14 and v13 for clear-sky FCI IR channel simulations over the 25000 profiles on 137L. The largest differences are seen in the highest peaking water

vapour channel (6.3 μm). The lower peaking water vapour channel (7.3 μm) and the ozone channel (9.6 μm) also have larger differences compared to the other channels.

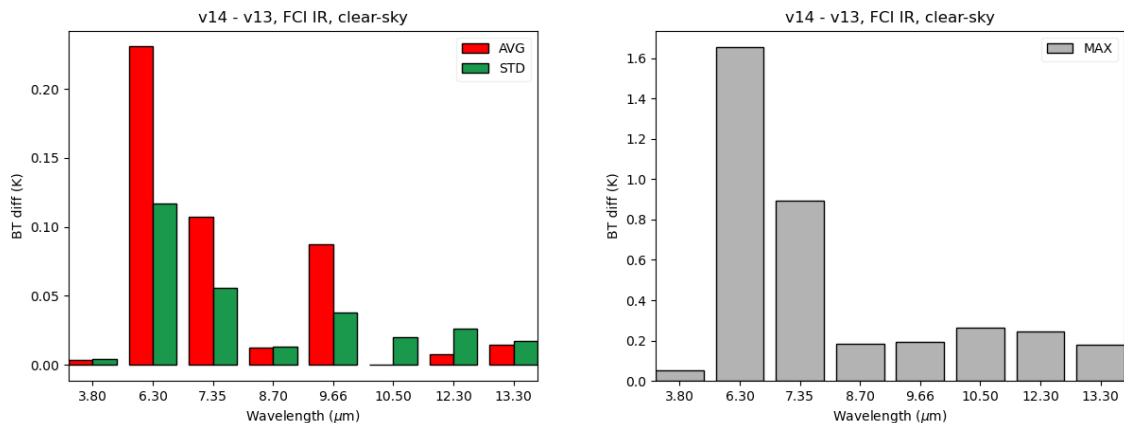


Figure 3.1.1: statistics of RTTOV v14 minus v13 brightness temperatures for clear-sky FCI IR channel simulations for the 25000 profile set on 137L with varying zenith angles.

Figure 3.1.2 compares RTTOV v14 and v13 for hydrometeor scattering FCI IR channel simulations using the Chou-scaling solver over the 10000 profile subset on 137L. Due to the inconsistency between the RTTOV v13 profile representation and the NWP model representation described in [section 2.1](#), a consistent bias is observed for thermal IR scattering simulations whereby RTTOV v14 BTs are warmer than v13. Typically, in RTTOV v13, the top-most NWP cloud layer is discarded, and the remaining cloud layers are input to RTTOV resulting in a half-layer shift upwards. Therefore, the top of the clouds in v13 are, on average, a little colder than in v14 resulting in warmer BTs in v14.

Figure 3.1.3 compares RTTOV v14 and v13 for hydrometeor scattering FCI IR channel simulations using the DOM solver with 8 streams over the 10000 profile subset on 137L. Results for the DOM solver are broadly similar to those for the fast Chou-scaling solver.

Figure 3.1.4 compares RTTOV v14 and v13 for aerosol scattering FCI IR channel simulations using the Chou-scaling solver over the 20000 MACC profile subset on 60L. The impact of aerosols on top of atmosphere radiances is smaller than clouds, and as such the differences related to water vapour absorption (as in Figure 3.1.1) are evident in the channels at 6.3 and 7.3 μm .

Figure 3.1.5 compares RTTOV v14 and v13 for aerosol scattering FCI IR channel simulations using the DOM solver with 8 streams over the 20000 MACC profile subset on 60L. Again, results for the DOM solver are broadly similar to those for the fast Chou-scaling solver.

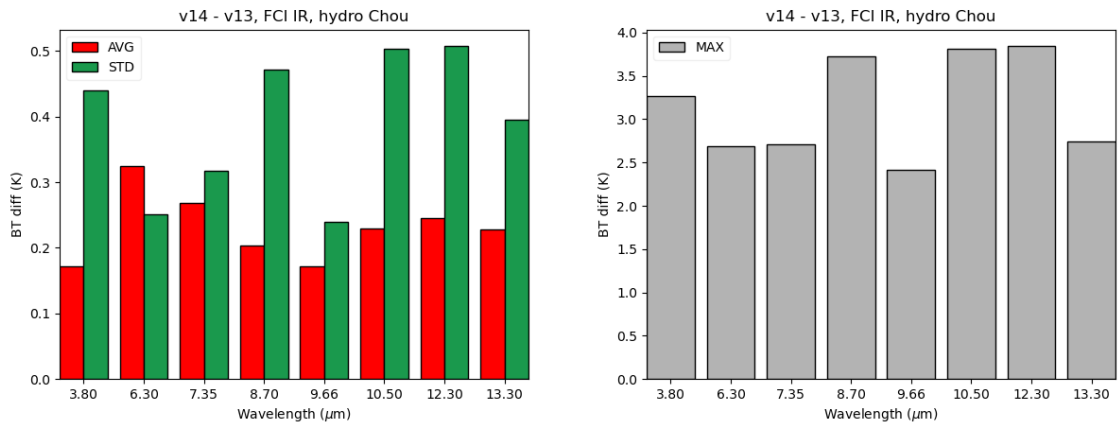


Figure 3.1.2: statistics of RTTOV v14 minus v13 brightness temperatures for hydrometeor scattering FCI IR channel simulations with the Chou-scaling solver for the 10000 profile subset on 137L with varying zenith angles.

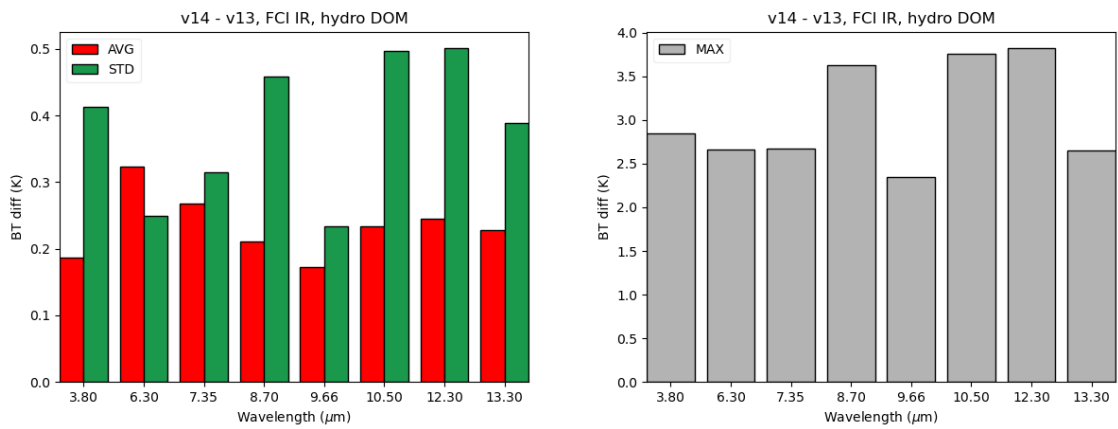


Figure 3.1.3: statistics of RTTOV v14 minus v13 brightness temperatures for hydrometeor scattering FCI IR channel simulations with the DOM solver for the 10000 profile subset on 137L with varying zenith angles.

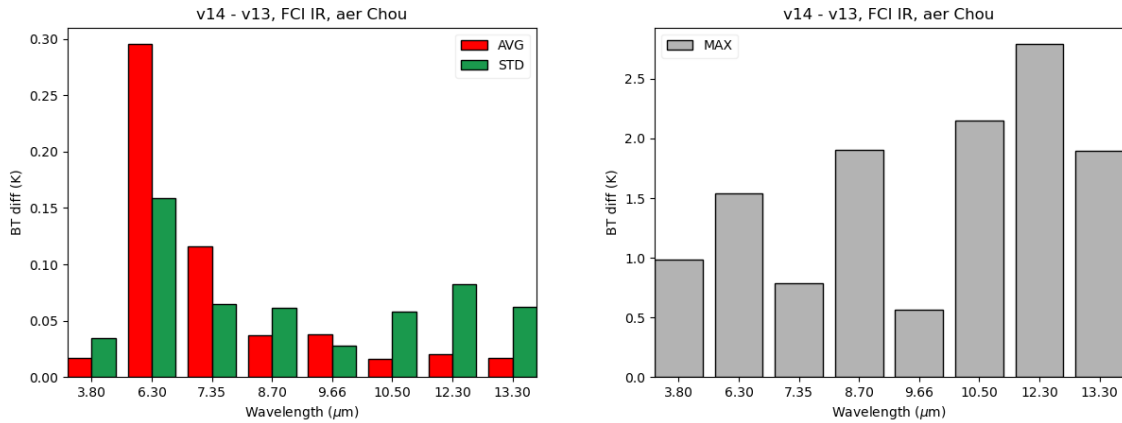


Figure 3.1.4: statistics of RTTOV v14 minus v13 brightness temperatures for aerosol scattering FCI IR channel simulations with the Chou-scaling solver for the MACC 20000 profile subset on 60L with varying zenith angles.

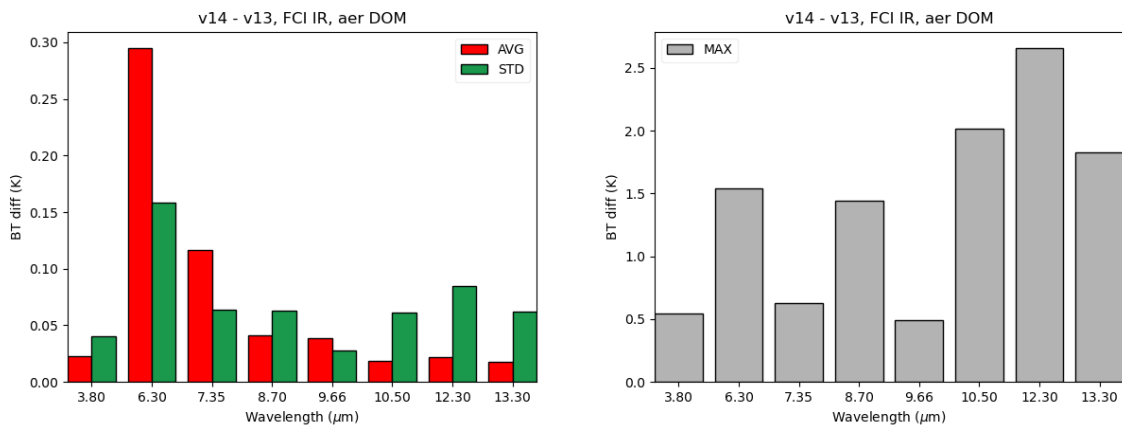


Figure 3.1.5: statistics of RTTOV v14 minus v13 brightness temperatures for aerosol scattering FCI IR channel simulations with the DOM solver for the MACC 20000 profile subset on 60L with varying zenith angles.

Figure 3.1.6 compares RTTOV v14 and v13 for clear-sky FCI VIS/NIR channel simulations over the 25000 profiles on 137L.

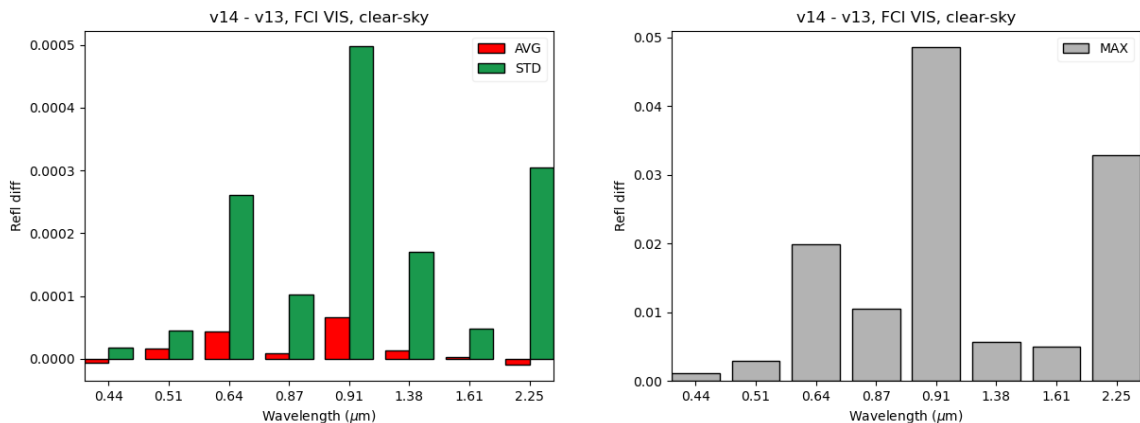


Figure 3.1.6: statistics of RTTOV v14 minus v13 reflectances for clear-sky FCI VIS/NIR channel simulations for the 25000 profile set on 137L with varying satellite and solar zenith and relative azimuth angles.

Figure 3.1.7 compares RTTOV v14 and v13 for hydrometeor scattering FCI VIS/NIR channel simulations using the DOM solver with 8 streams over the 10000 profile subset on 137L. Here the v13 reflectances are on average larger than those in v14 because of the half-layer shift upwards in the cloud profile described above. The result is less atmosphere between the cloud top and the satellite in v13 meaning less absorption.

Figure 3.1.8 compares RTTOV v14 and v13 for hydrometeor scattering FCI VIS/NIR channel simulations using the MFASIS-NN solver over the 10000 profile subset on 137L. Only channels supported by MFASIS-NN in both RTTOV v13 and v14 are compared. The Baum ice scheme is used for cloud ice as the Baran scheme is not supported by MFASIS-NN. As described in [section 2.8](#) MFASIS-NN has been improved for RTTOV v14 and as such the differences between v13 and v14 are larger than those for the DOM solver. The small negative bias (larger reflectances in v13 than v14) is still evident here.

Figure 3.1.9 compares RTTOV v14 and v13 for aerosol scattering FCI VIS/NIR channel simulations using the DOM solver with 8 streams over the 20000 MACC profile subset on 60L. Again, the negative bias is evident, with larger reflectances in v13 than v14.

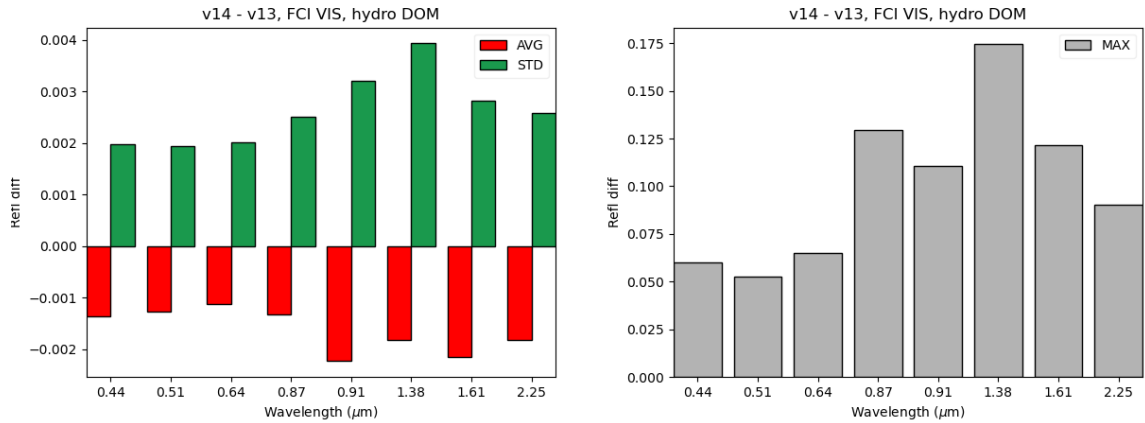


Figure 3.1.7: statistics of RTTOV v14 minus v13 reflectances for hydrometeor scattering FCI VIS/NIR channel simulations with the DOM solver for the 10000 profile subset on 137L with varying satellite and solar zenith and relative azimuth angles.

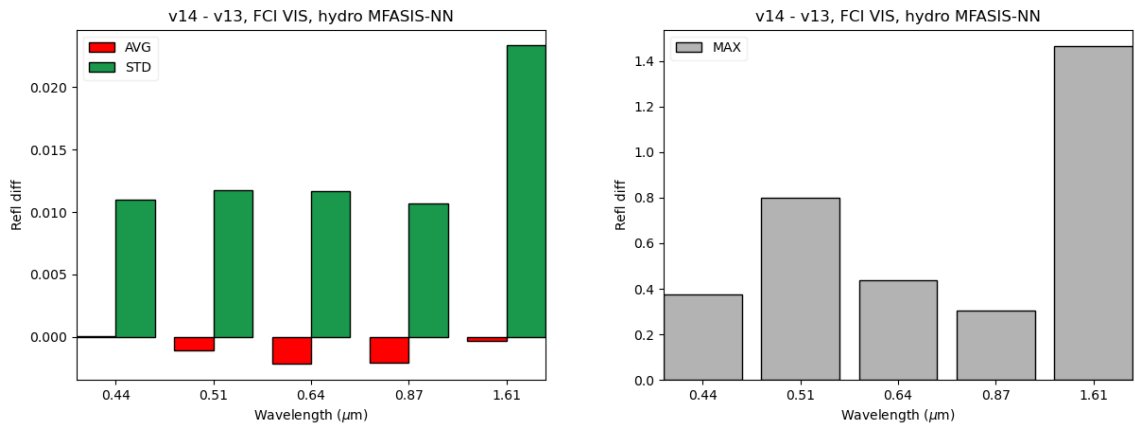


Figure 3.1.8: statistics of RTTOV v14 minus v13 reflectances for aerosol scattering FCI VIS/NIR channel simulations with the MFASIS-NN solver for the MACC 20000 profile subset on 60L with varying satellite and solar zenith and relative azimuth angles. Only channels supported by MFASIS-NN in both RTTOV v13 and v14 are included in the plots.

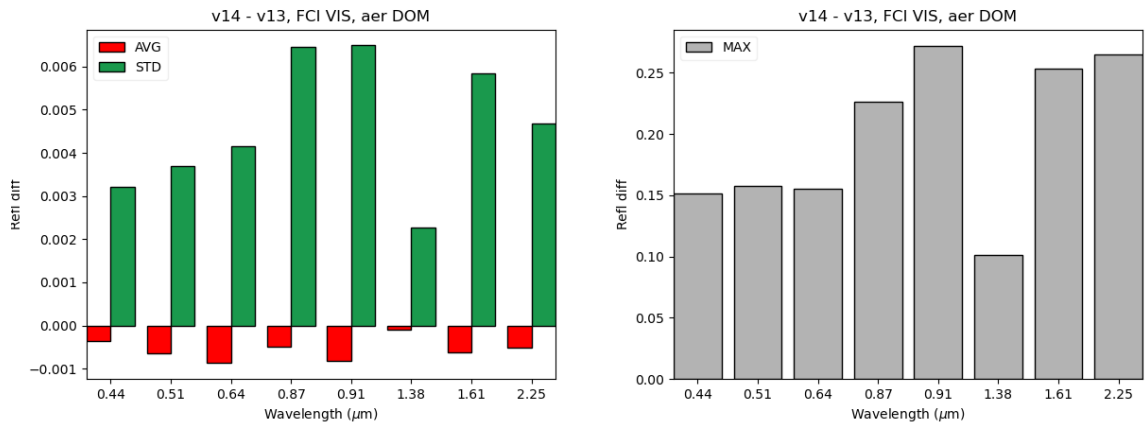


Figure 3.1.9: statistics of RTTOV v14 minus v13 reflectances for aerosol scattering FCI VIS/NIR channel simulations with the DOM solver for the MACC 20000 profile subset on 60L with varying satellite and solar zenith and relative azimuth angles.

Figure 3.1.10 compares RTTOV v14 and v13 mean Jacobians for clear-sky FCI IR channel simulations over the 5000 temperature-/water vapour-sampled subsets of the profiles on 137L. Overall there is good agreement between the v13 and v14 Jacobians.

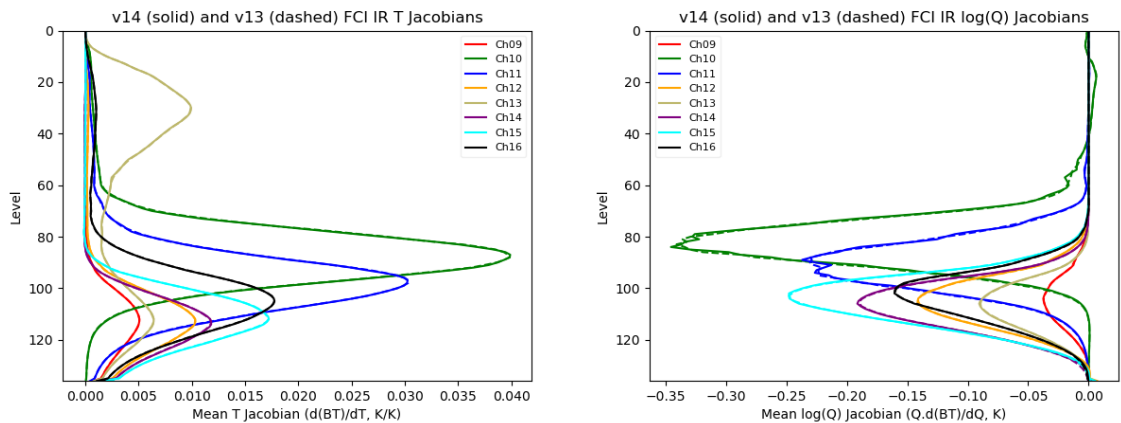


Figure 3.1.10: mean temperature (left) and water vapour (right) Jacobians for RTTOV v14 (solid lines) and RTTOV v13 (dashed lines) for clear-sky FCI IR channel simulations for 5000 profile subsets on 137L with varying zenith angles.

Figure 3.1.11 compares RTTOV v14 and v13 mean Jacobians for clear-sky FCI VIS channel simulations over the 5000 temperature-/water vapour-sampled subsets of the profiles on 137L. There is good agreement between the water vapour Jacobians. The v14 temperature Jacobians for visible/near-IR channels exhibit more jaggedness than in v13, but it should be noted that these channels do not convey much temperature information. The absolute

magnitude of the average temperature Jacobians is of order 10^{-6} when expressed in terms of reflectance.

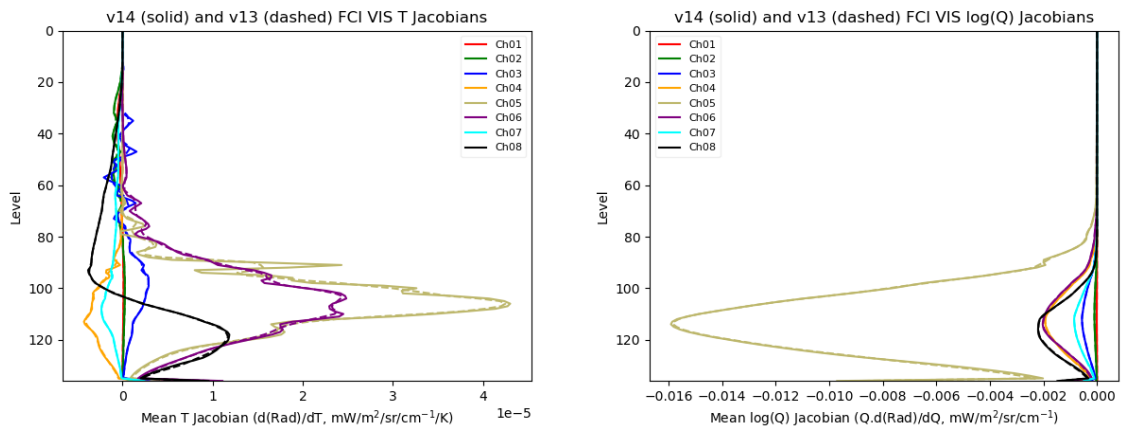


Figure 3.1.11: mean temperature (left) and water vapour (right) Jacobians for RTTOV v14 (solid lines) and RTTOV v13 (dashed lines) for clear-sky FCI VIS channel simulations for 5000 profile subsets on 137L with varying satellite and solar zenith and relative azimuth angles.

3.1.2 MetOp IASI comparisons

The simulations in this section use Metop IASI coefficients based on v13 predictors with all variable gases.

Figure 3.1.12 compares RTTOV v14 and v13 for clear-sky IASI simulations over the 25000 profiles on 137L. The mean and standard deviation of differences are typically smaller than those seen for multi-spectral sensors (Figure 3.1.1 for FCI IR channels, Figure 3.1.17 for ATMS). The largest differences occur for the water vapour channels and the highest peaking channels.

Figure 3.1.13 compares RTTOV v14 and v13 for hydrometeor scattering IASI simulations using the Chou-scaling solver over the 10000 profile subset on 137L. These differences are broadly comparable to those seen for FCI IR channels (Figure 3.1.2). Again, larger radiances in v14 are seen due to difference in the way the cloud profiles are represented within v13 and v14 as described above.

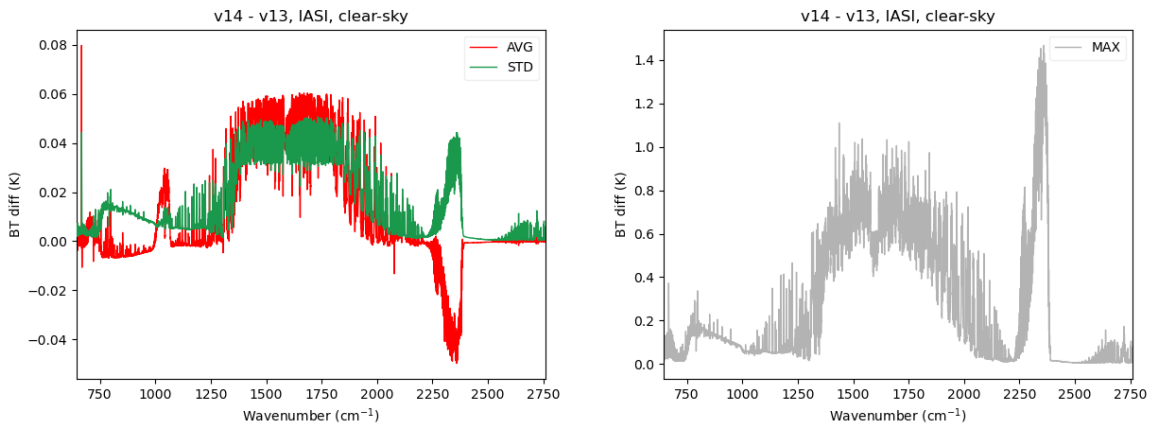


Figure 3.1.12: statistics of RTTOV v14 minus v13 brightness temperatures for clear-sky IASI channel simulations for the 25000 profile set on 137L with varying zenith angles.

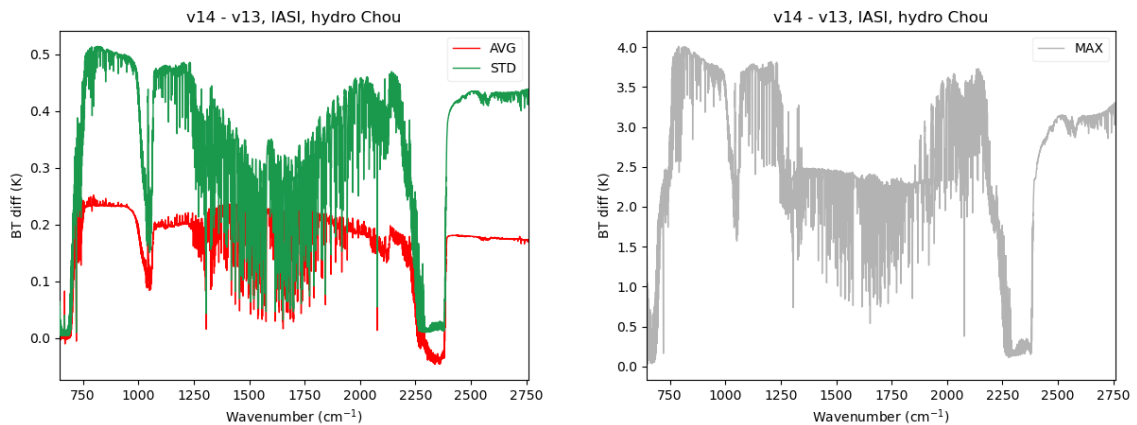


Figure 3.1.13: statistics of RTTOV v14 minus v13 brightness temperatures for hydrometeor scattering IASI channel simulations with the Chou-scaling solver for the 10000 profile subset on 137L with varying zenith angles.

Figure 3.1.14 compares RTTOV v14 and v13 for aerosol scattering IASI simulations using the Chou-scaling solver over the 20000 MACC profile subset on 60L. In this case, as for FCI IR channels (Figure 3.1.5), the impact of aerosols on radiances relatively small, so we see the larger differences in the water vapour and higher peaking channels as in the clear sky case. The differences are larger here compared to the clear-sky case due to the coarser vertical resolution (60 levels here vs 137 levels in the clear sky plot).

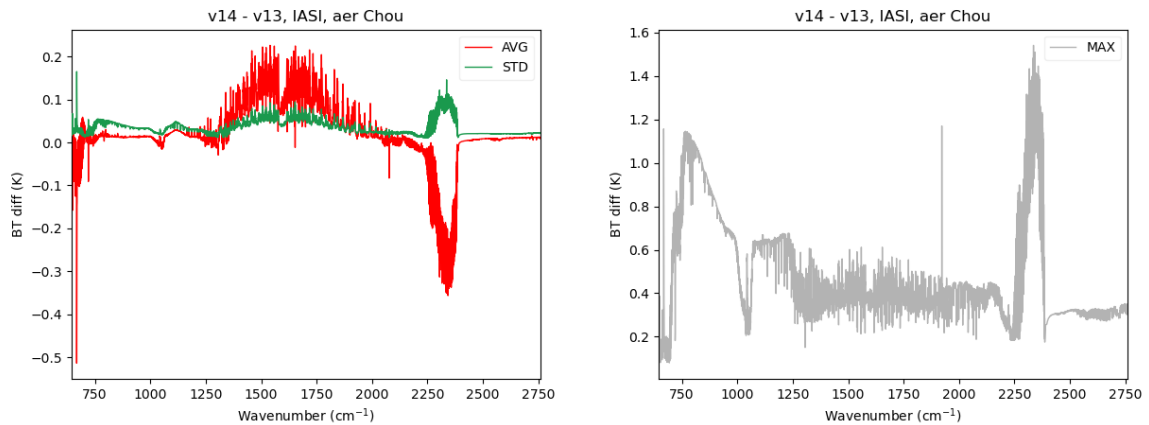


Figure 3.1.14: statistics of RTTOV v14 minus v13 brightness temperatures for aerosol scattering IASI channel simulations with the Chou-scaling solver for the MACC 20000 profile subset on 60L with varying zenith angles.

Figure 3.1.15 compares RTTOV v14 and v13 mean Jacobians for selected IASI channels for clear-sky simulations over the 5000 temperature-/water vapour-sampled subsets of the profiles on 137L. The channels were selected to represent different regions of the infrared spectrum covered by IASI. Overall, there is good agreement between the v13 and v14 Jacobians.

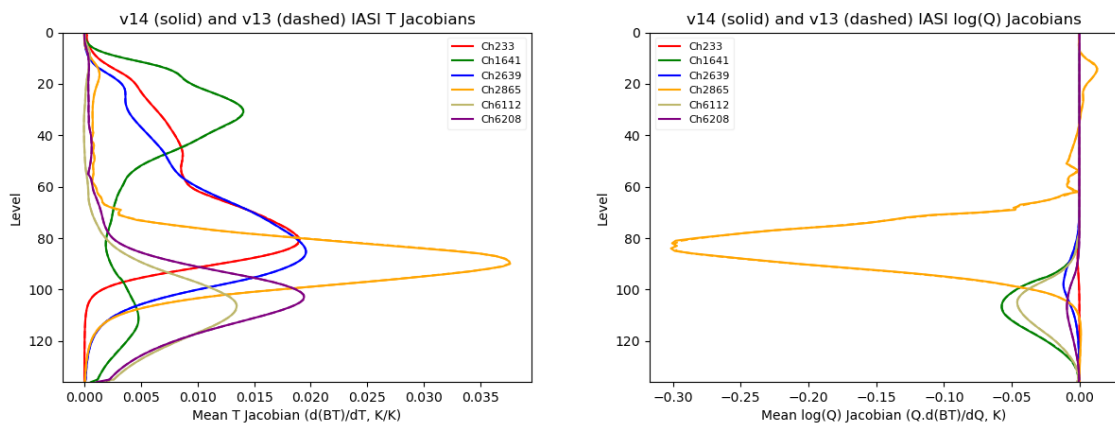


Figure 3.1.15: mean temperature (left) and water vapour (right) Jacobians for RTTOV v14 (solid lines) and RTTOV v13 (dashed lines) for selected IASI channels for clear-sky simulations for 5000 profile subsets on 137L with varying zenith angles.

3.1.3 MetOp GOME-2 comparisons

The simulations in this section use Metop GOME-2 coefficients based on v13 predictors with variable O_3 .

Figure 3.1.16 compares RTTOV v14 and v13 for clear-sky GOME-2 simulations over the 25000 profiles on 137L. The simulations include Rayleigh single scattering. The impact of the extended USGS water reflectance dataset ([section 2.16](#)) is evident in the surface sensitive channels at 25000-34000 cm^{-1} . Some differences are also visible in the regions of water vapour absorption below 20000 cm^{-1} (to the right of the plots).

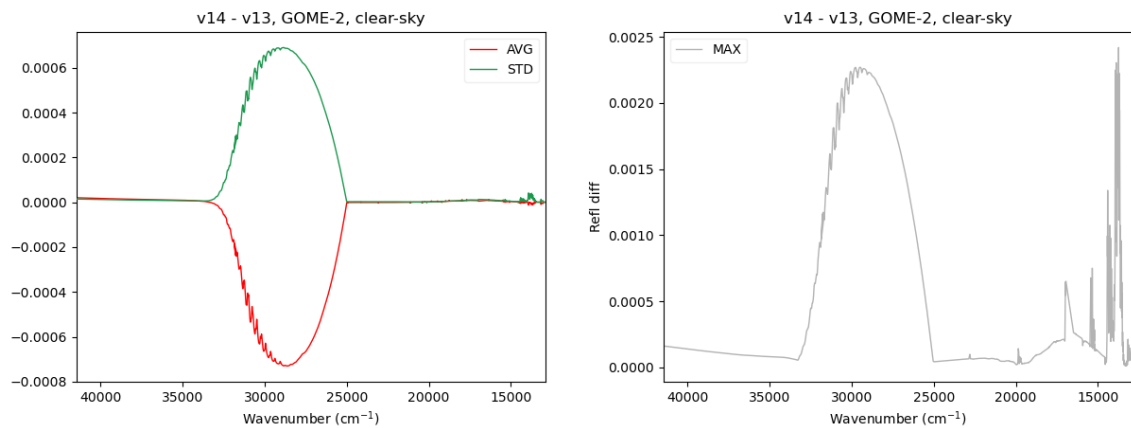


Figure 3.1.16: statistics of RTTOV v14 minus v13 brightness temperatures for clear-sky GOME-2 simulations for the 25000 profile set on 137L with varying satellite and solar zenith and relative azimuth angles.

3.1.4 Suomi-NPP ATMS comparisons

The simulations in this section use SNPP ATMS coefficients based on v13 predictors with no variable gases and top hat pass bands.

Figure 3.1.17 compares RTTOV v14 and v13 for clear-sky ATMS simulations over the 25000 profiles on 137L. The largest differences between v13 and v14 typically occur in the highest peaking channels (e.g., 14 and 15) and the water vapour channels (18-22).

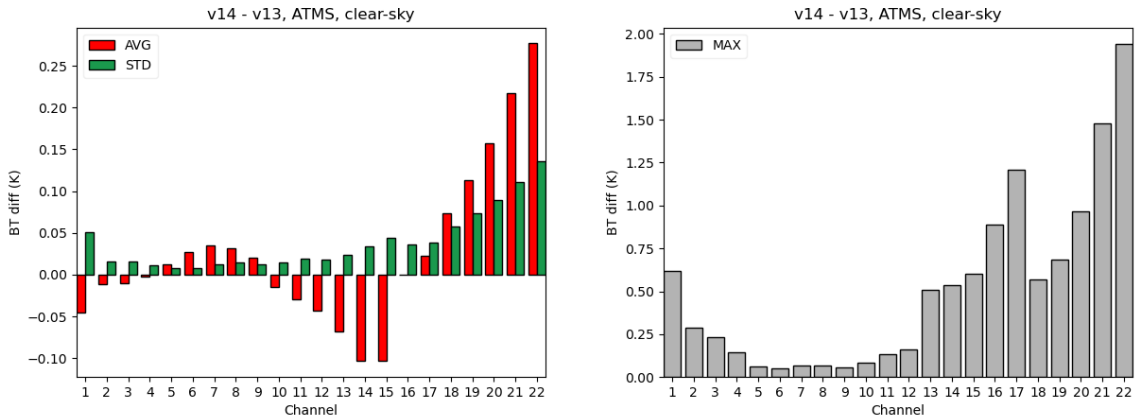


Figure 3.1.17: statistics of RTTOV v14 minus v13 brightness temperatures for clear-sky ATMS simulations for the 25000 profile set on 137L with varying zenith angles.

Figure 3.1.18 compares RTTOV v14 and v13 for clear-sky ATMS simulations with cloud liquid water absorption (no scattering) over the 10000 profile subset on 137L. The change in the atmospheric representation and calculation of cloud liquid water absorption ([section 2.1](#)) leads to larger differences on top of those seen in the clear-sky case above.

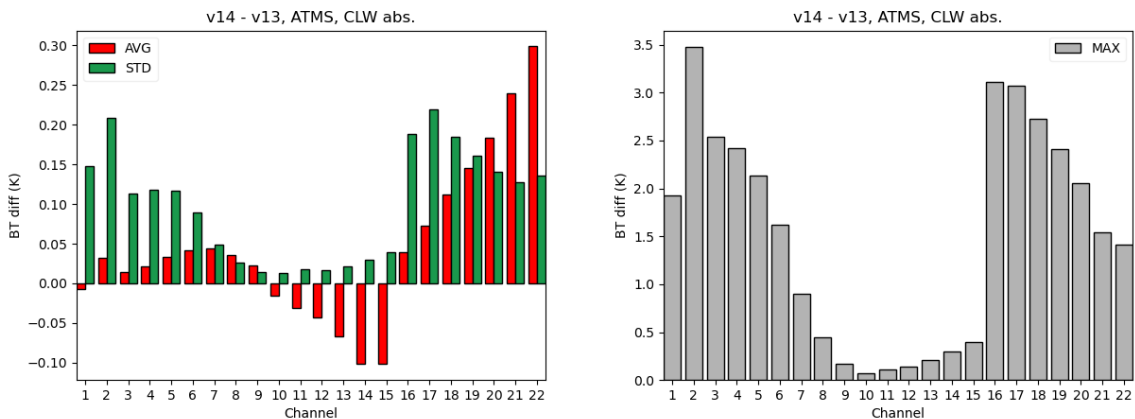


Figure 3.1.18: statistics of RTTOV v14 minus v13 brightness temperatures for clear-sky ATMS simulations with cloud liquid water absorption (no scattering) for the 10000 profile subset on 137L with varying zenith angles.

Figure 3.1.19 compares RTTOV v14 and v13 for hydrometeor scattering ATMS simulations using the delta-Eddington solver over the 10000 profile subset on 137L. Biases are quite similar to the clear-sky case, and slightly larger for WV channels. The standard deviation is similar to the clear-sky case for temperature sounding and window channels, but larger in the water vapour channels compared to the clear-sky case. The delta-Eddington/scattering

implementation is very similar – though not identical – between v13 and v14, so the impact of the clear-sky differences are evident here.

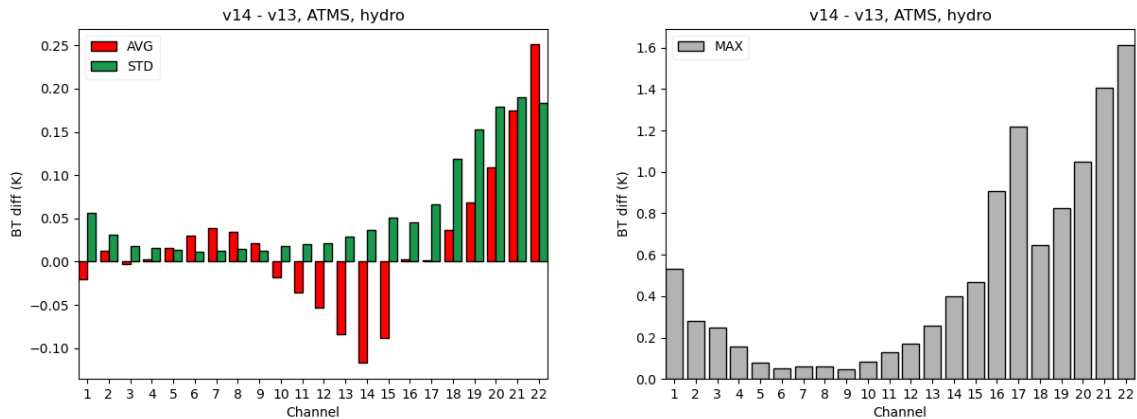


Figure 3.1.19: statistics of RTTOV v14 minus v13 brightness temperatures for hydrometeor scattering ATMS simulations with the delta-Eddington solver for the 10000 profile subset on 137L with varying zenith angles.

Figure 3.1.20 compares RTTOV v14 and v13 mean Jacobians for clear-sky ATMS simulations over the 5000 temperature-/water vapour-sampled subsets of the profiles on 137L. Overall there is good agreement between the v13 and v14 Jacobians.

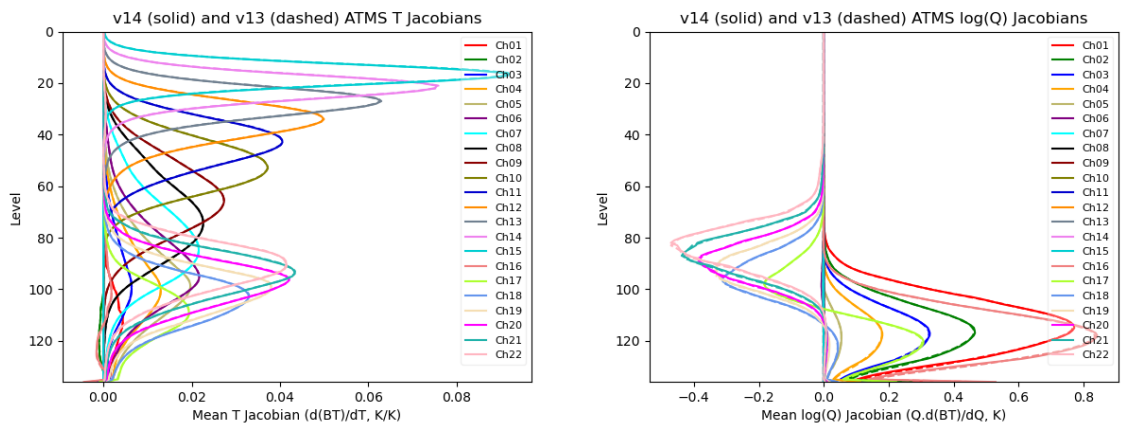


Figure 3.1.20: mean temperature (left) and water vapour (right) Jacobians for RTTOV v14 (solid lines) and RTTOV v13 (dashed lines) for clear-sky ATMS simulations for 5000 profile subsets on 137L with varying zenith angles.

3.1.5 MetopSG ICI comparisons

The simulations in this section use MetopSG ICI coefficients based on v13 predictors with variable ozone and top hat pass bands. Ozone varies among the simulated profiles.

Figure 3.1.21 compares RTTOV v14 and v13 for clear-sky ICI simulations over the 25000 profiles on 137L. Again, the largest differences are observed in channels with the greatest water vapour absorption.

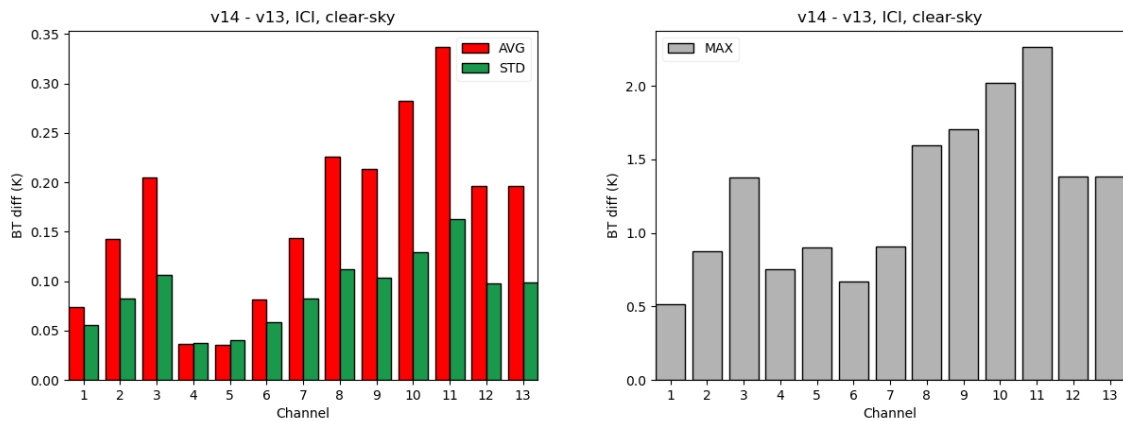


Figure 3.1.21: statistics of RTTOV v14 minus v13 brightness temperatures for clear-sky ICI simulations for the 25000 profile set on 137L with varying zenith angles.

Figure 3.1.22 compares RTTOV v14 and v13 for clear-sky ICI simulations with cloud liquid water absorption (no scattering) over the 10000 profile subset on 137L. As for ATMS (Figure 3.1.18), the biases are slightly larger than the clear-sky case, while the standard deviations are significantly larger.

Figure 3.1.23 compares RTTOV v14 and v13 for hydrometeor scattering ICI simulations using the delta-Eddington solver over the 10000 profile subset on 137L. Scattering is stronger in the sub-mm, leading to greater sensitivity to the differences between v13 and v14. The differences are therefore larger than in the clear-sky case.

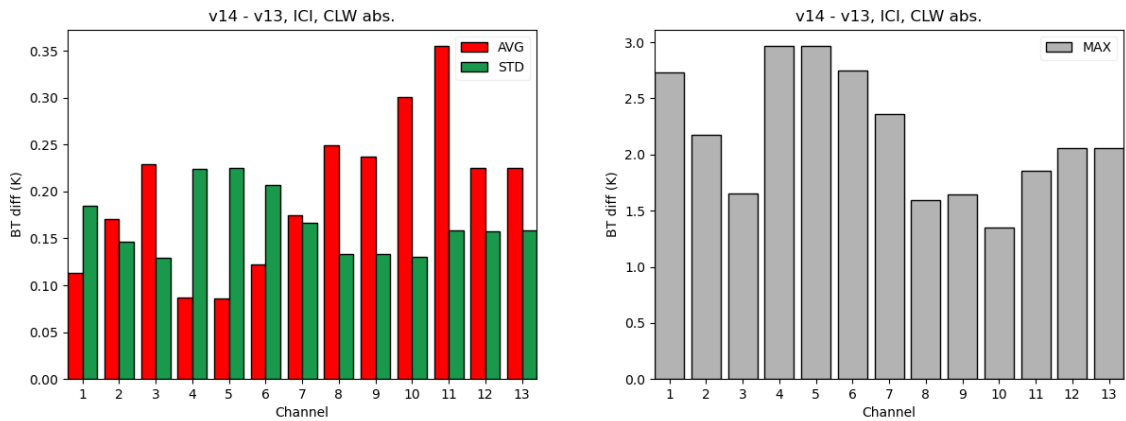


Figure 3.1.22: statistics of RTTOV v14 minus v13 brightness temperatures for clear-sky ICI simulations with cloud liquid water absorption (no scattering) for the 10000 profile subset on 137L with varying zenith angles.

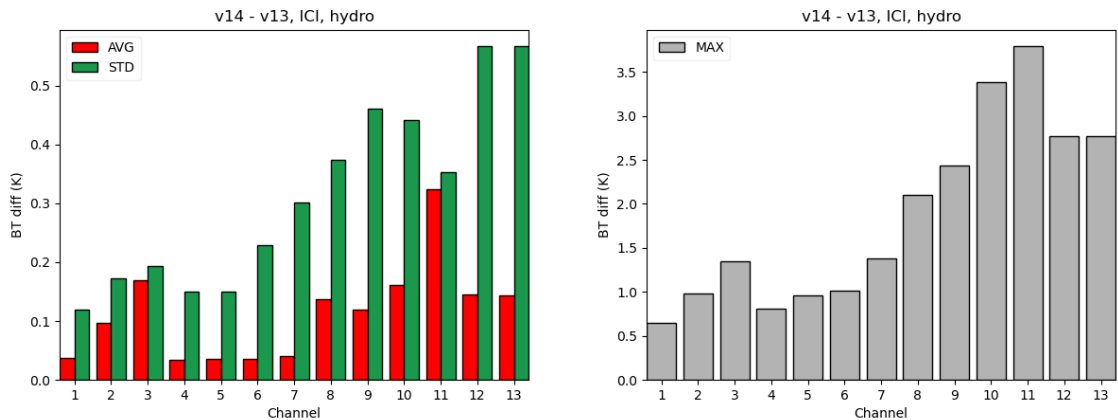


Figure 3.1.23: statistics of RTTOV v14 minus v13 brightness temperatures for hydrometeor scattering ICI simulations with the delta-Eddington solver for the 10000 profile subset on 137L with varying zenith angles.

Figure 3.1.24 compares RTTOV v14 and v13 mean Jacobians for clear-sky ICI simulations over the 5000 temperature-/water vapour-sampled subsets of the profiles on 137L. Overall there is good agreement between the v13 and v14 Jacobians.

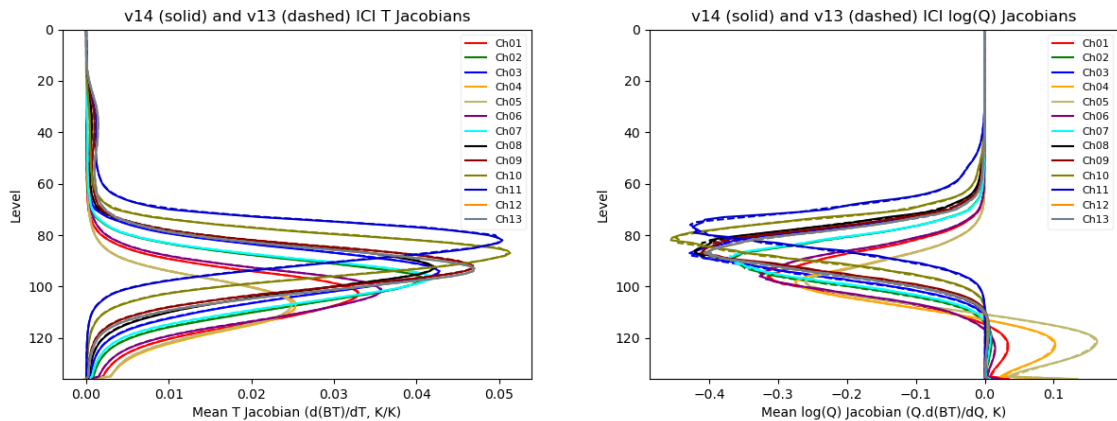


Figure 3.1.24: mean temperature (left) and water vapour (right) Jacobians for RTTOV v14 (solid lines) and RTTOV v13 (dashed lines) for clear-sky ICI simulations for 5000 profile subsets on 137L with varying zenith angles.

3.2 Comparisons with observations - IFS

This section documents the evaluation of RTTOV v14.0 in the ECMWF Integrated Forecast System (IFS). In the monitoring and assimilation experiments discussed below, RTTOV v14.0 has been configured to be as similar as possible to the existing operational RTTOV v13.2 configuration in the IFS.

3.2.1 Monitoring results

An essential step on assessing the impact of changes in the radiative transfer model is to evaluate the consistency between radiances simulated by the RTTOV from an input atmospheric profile and the real observations measured by a variety of microwave and infrared instruments.

In the IFS this is done by performing monitoring-only experiments, which monitor a change in first-guess departure without generating a new analysis and forecast. ECMWF IFS cycle 49R1 was used for the experiments, with 137 vertical levels and 12-hour long window delayed cutoff analysis and first guess forecast cycles. The model resolution was set to TCo399 (triangular-cubic-octahedral truncation at wavenumber 399), giving a grid spacing of ~28 km.

To assess the effect of the changes from RTTOV v13.2 (control) to RTTOV v14.0 (experiment) on the fit to observations, we now present an evaluation of IASI and ATMS data in terms of background departure statistics against clear-sky brightness temperatures simulated from short-term forecasts. The RTTOV v14.0 experiment uses the same gas

optical depth coefficient files as used operationally at ECMWF with the RTTOV v13.2 run, whereas the hydrometeor optical property files are in a new RTTOV v14 format but are scientifically unchanged.

In the plots discussed below from the passive monitoring experiment, the VarBC bias correction is taken from the operational RTTOV v13 system and as such is not appropriate to RTTOV v14. Therefore, the lines showing results “After VarBC” should be disregarded. It is to be expected that in full cycling runs with v14, VarBC would adapt and would better fit the v14 departures.

Figure 3.2.1 show mean and standard deviation of background departures in MetOp-B/C IASI brightness temperature data as a function of channel central wavenumber for both RTTOV v13.2 and v14.0 simulations. The statistics have been evaluated over a one-month July 2022 period to ensure the adequate representation of channels that are frequently removed because of cloud contamination. The mean and standard deviation statistics of background departures before bias correction (solid lines) show generally very small differences between the runs with either version of RTTOV. Using RTTOV v14.0 improves the standard deviation of background departures (before bias correction) for most of IASI channels (e.g., sounding channels sensitive to tropospheric temperature in the wavenumber range 710-810 cm^{-1} , ozone and water vapour sensitive channels, see Figure 3.2.5a). Although results are shown here primarily for the IASI instruments, similar results are obtained from spectra observed by the S-NPP and NOAA-20 CrIS instruments (Figure 3.2.2 and Figure 3.2.5b) and the Aqua AIRS (not shown).

Background fits to ATMS on S-NPP and NOAA-20 are shown in Figure 3.2.3. Global mean of background departure before bias correction calculated by RTTOV v14.0 and RTTOV v13.2 are rather similar in the temperature sounding channels 6-15, resulting in up to 0.03 K smaller RTTOV v14 biases in channels 6-9 and slightly larger RTTOV v14 biases in channels 10-15, going up to 0.1 K for the stratospheric temperature sounding channels 14-15. Differences between RTTOV v14 and RTTOV v13.2 simulations are found for biases in the humidity-sensitive sounding channels, resulting in RTTOV v14 biases being up to 0.2 K smaller than RTTOV v13.2 biases in the 183 GHz band. Standard deviations of background departure statistics before bias correction overall decreased for most of ATMS channels, showing encouraging signs for the RTTOV v14 experiment (Figure 3.2.5c).

Figure 3.2.4 briefly explores the effect of changes for five AMSU-A instruments, used in all-sky conditions within the IFS. Fits to AMSU-A channels 5-14 primarily sampling the oxygen absorption band near 50 GHz are similar with fits to ATMS channels 6-15. As it is expected, the standard deviation of background departures is much larger for the window channels 1 (23.8 GHz) and 2 (31.4 GHz) than for most temperature sounding channels 5-14 (typically less than 1K). With RTTOV v14.0, there is a small but detectable degradation (less than 0.1

%) in fit to AMSU-A channels 1 (23.8 GHz) and 2 (31.4 GHz), sensitive to cloud water and precipitation (Fig3.2.5d).

The all-sky framework at ECMWF includes many different sensor and satellite combinations. While results are channel, sensor and satellite dependent, the confidence on the RTTOV v14 results can be increased by analysing data from multi-instruments measuring in the same frequency range. Broadly, the standard deviation of background departures in 183 ± 7 and 183 ± 3 GHz channels (SSMIS, MHS, MWHS2, GMI) was increased by up to 0.4% in the RTTOV v14 experiment, while in 183 ± 3 GHz was typically decreased by up to 0.2% (SSMIS, MHS, MWHS2). For cloud-sensitive channels from 19 to 166 GHz (e.g. GMI, AMSR2, SSMIS) consistent results are obtained, and in the RTTOV v14 run, the standard deviation was increased, but only by 0.005% (not shown).

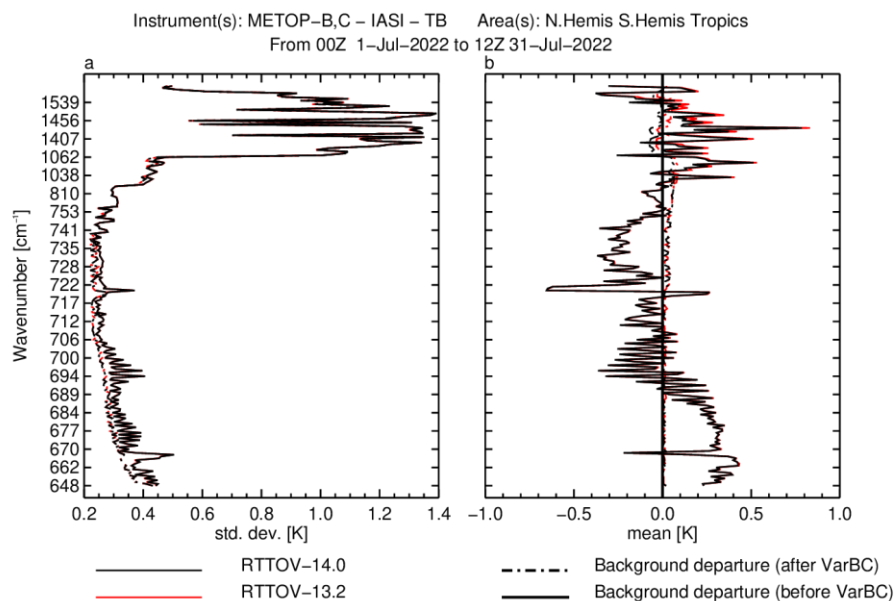


Figure 3.2.1: Background departure statistics for IASI (on MetOp-B and MetOp-C) for July 2022 in the ECMWF system. Global statistics (mean and standard deviation) for RTTOV v14.0 experiment are shown in black, whereas statistics for the RTTOV v13.2 experiment are shown in red, with solid (dotted) lines showing background departure statistics before (after) bias correction.

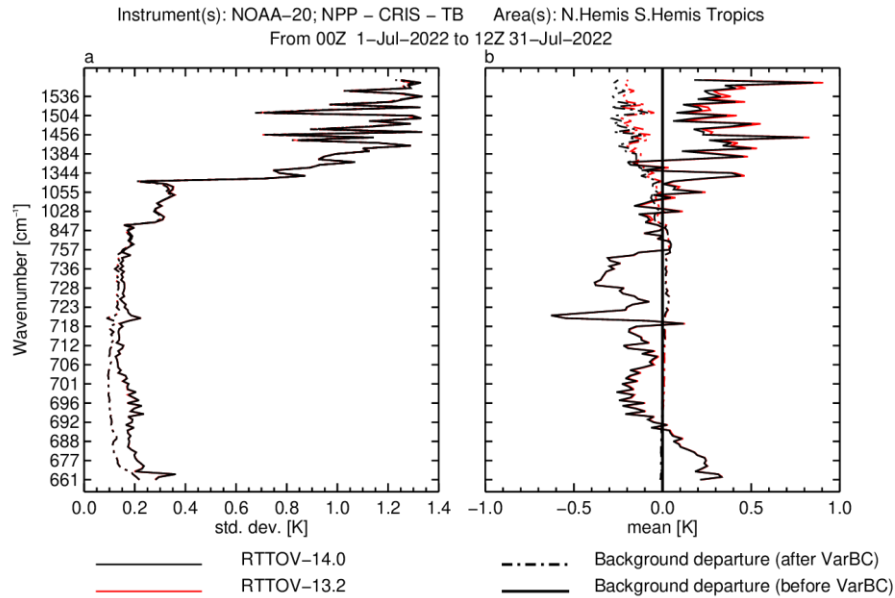


Figure 3.2.2: As Figure 3.2.1, but for CrIS on NOAA-20 and S-NPP over the globe.

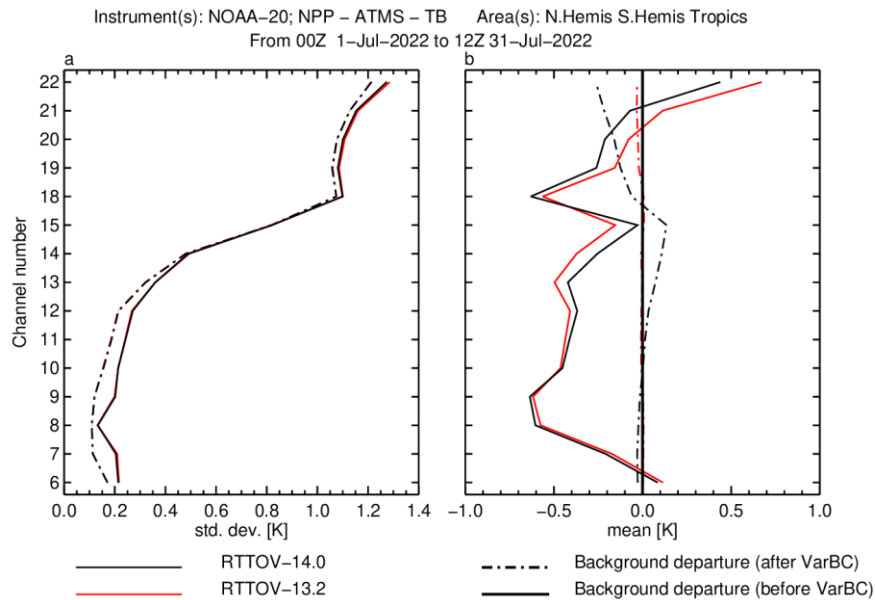


Figure 3.2.3: Background departure statistics for ATMS (on S-NPP and NOAA-20) for July 2022 in the ECMWF system. Global statistics (mean and standard deviation) for RTTOV v14.0 experiment are shown in black, whereas statistics for the RTTOV v13.2 experiment are shown in red, with solid (dotted) lines showing background departure statistics before (after) bias correction.

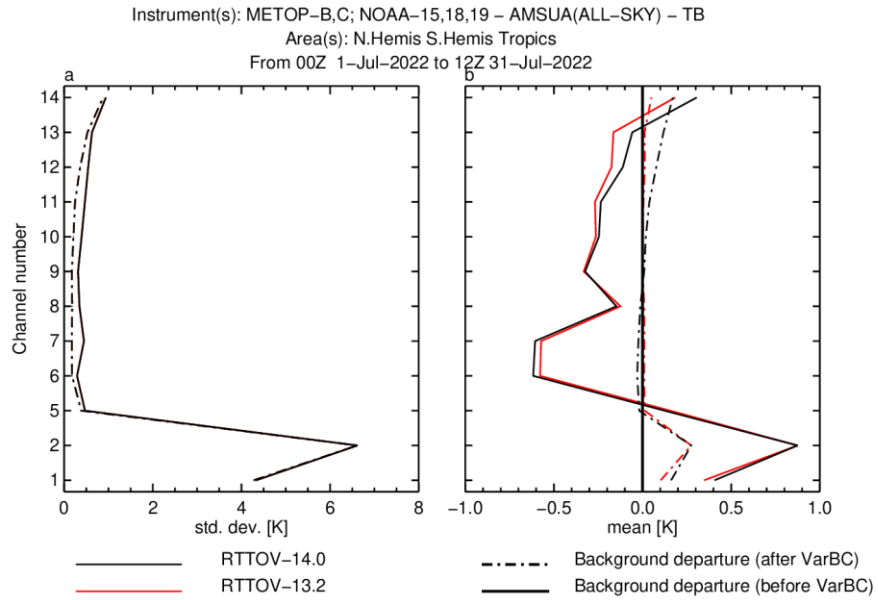


Figure 3.2.4: As Figure 3.2.3, but for AMSU-A radiances on MetOp-B/C and NOAA-15/18/19 satellites.

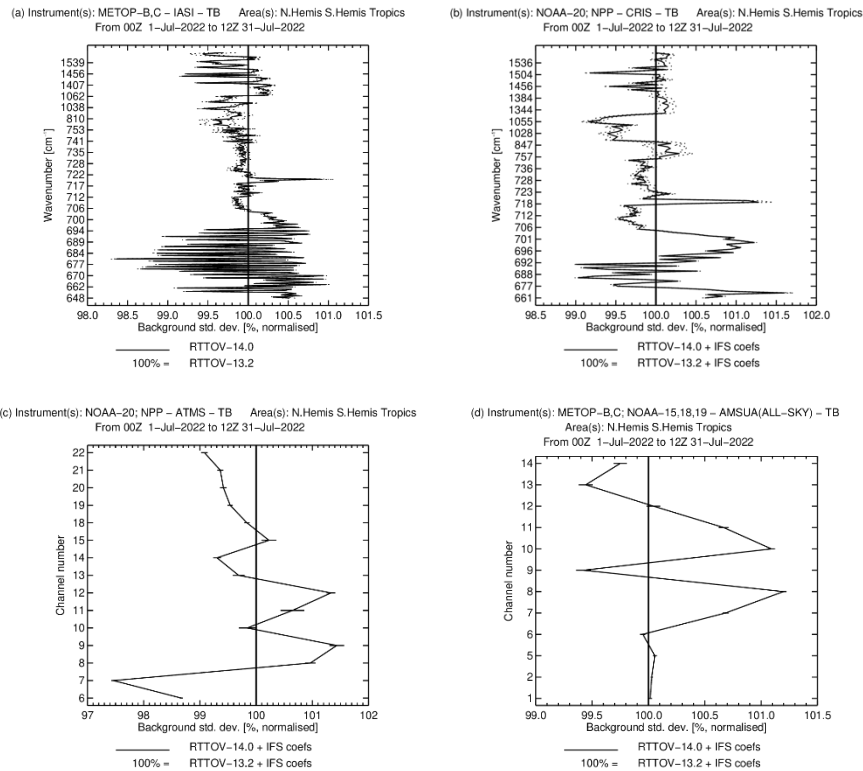


Figure 3.2.5: Normalised change in background departure standard deviation before VarBC for actively assimilated channels of (a) IASI (b) CrIS (c) ATMS and (d) AMSU-A. The results are based on a global sample of observations aggregated over the one-month experiment period.

3.2.2 Data assimilation results – full cycling results

The move from RTTOV v13.2 (Control) to RTTOV v14 was tested for its forecast impact in experiments based on two periods, 1st June 2022 to 31st August 2022 and 1st December 2020 to 28th February 2023. The experiments use a full observing system that follows that used in ECMWF operations and are based on the standard testing configuration at TCo399 (about 25 km horizontal resolution) with a 12-hour assimilation window. Background errors are held fixed between the two experiments and come from a separate ensemble data assimilation experiment based on the cycle 49r1 configuration.

Replacing RTTOV v13.2 with RTTOV v14 shows a neutral to positive forecast impact. Figure 3.2.6 shows the impact on vector wind errors, but similar results are seen in relative humidity and temperature. The impact at T+24 (T+N where N is the forecast length in hours) is in the lower troposphere around 30°S, while for longer forecast lead times of T+96, the impact dissipates across the southern mid-latitudes.

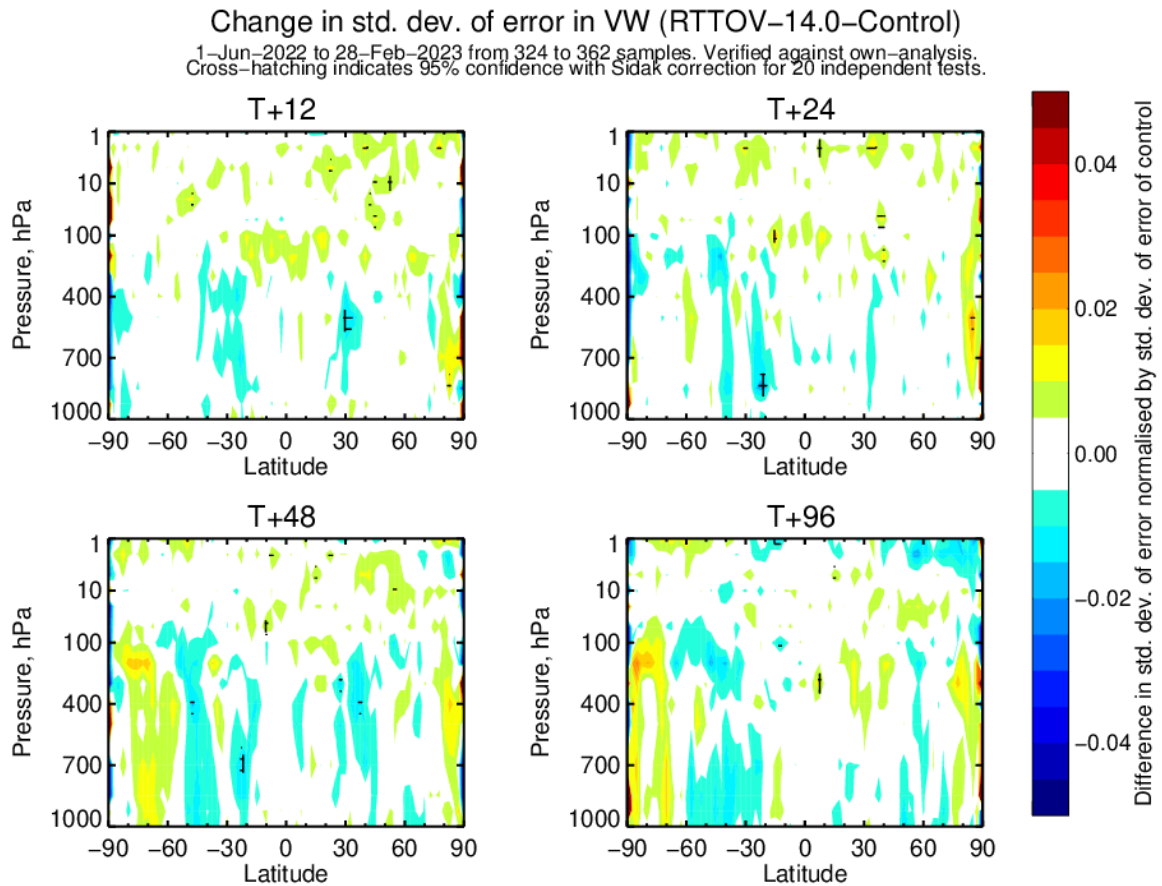


Figure 3.2.6: Difference in RMSE of vector wind (VW) error between RTTOV v14.0 and RTTOV v13.2 (Control) experiments, normalised by the RMSE of the Control experiment. Verification is against own-analysis. Cross-hatching shows statistical significance at the 95% confidence level based on 20 independent tests per panel. Captions T+N describe the forecast time N in hours.

Figure 3.2.7 shows the southern and northern extratropics impact on geopotential height at 500 hPa (Z500) forecasts, which is neutral at short and medium range forecasts.

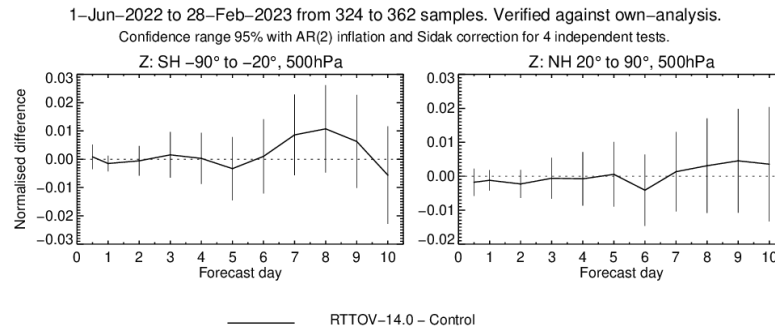


Figure 3.2.7: As Figure 3.2.6 but showing the difference in RMSE for geopotential height at 500 hPa aggregated over southern hemisphere extratropics (left) and northern hemisphere extratropics (right) as a function of forecast range. Error bars show the statistical significance range at the 95% confidence level based on 4 independent tests in the figure, and correcting for time correlations using an autoregressive AR(2) model.

Figure 3.2.8 shows that IASI fits to most channels sensitive to the stratospheric and tropospheric temperature and moisture improve by up to about 0.1% at background and by up to 0.5% at analysis (not shown), indicating that temperature and mid and upper-tropospheric humidity is better in agreement with IASI. Broadly similar impacts are seen for other infrared sensors in both the background (e.g. CrIS) and the analysis (not shown). Fits to ATMS humidity-sounding channels show similar improvements in the background and analysis. AMSU-A fits in channel 5 and 8 shows small but detectable degradation in background fit, however there is slightly improved fit to channels 1 and 2, which peak in the lower troposphere as well as to the stratospheric AMSU-A channels 13 and 14.

Figure 3.2.9 summarises the impact on the fit to independent observations. Positive short-range forecast impact is suggested by radiosondes and aircraft temperature observations, radiosonde humidity observations in the upper troposphere, as well as atmospheric motion vector winds. Robust and statistically significant positive improvements are seen at altitudes where GPS-RO radio occultation measurements are increasingly sensitive to humidity (i.e. the lower troposphere) and slight degradation (up to 0.1%) in altitude range 14 to 20 km.

A look at several timing statistics in OOPS with both RTTOV v14 and RTTOV v13.2 indicated that in the context of 4D-Var, the changes in RTTOV performance are completely negligible, both versions requiring similar computer resources.

The accuracy of the radiative transfer model underpins the operational radiance assimilation system and continuous efforts are dedicated to ensuring that the ECMWF system uses the most up-to-date version of RTTOV released by the EUMETSAT NWP SAF. The RTTOV v14 package introduces new science capabilities that pave the way for future developments,

and current research projects will benefit from this upgrade implementation successfully submitted for IFS CY50R1.

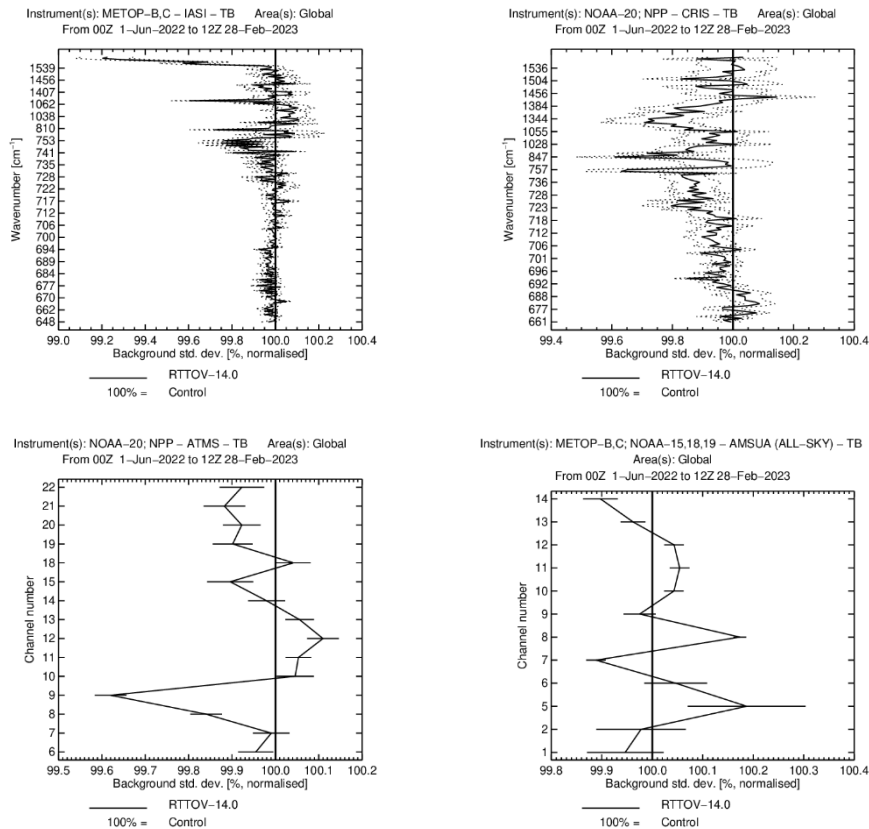


Figure 3.2.8: Changes in global background fits to observations resulting from using RTTOV v14 in assimilation runs. The observation types are IASI (top left), CrIS (top right), ATMS (bottom left) and AMSU-A (bottom right). The 100% line here represents the Control system, i.e. RTTOV v13.2 version. Only every fourth IASI channel is labelled on the axis. Values below 100% show an improved fit from using RTTOV v14 and above 100% show a degraded fit. Horizontal bars show the 95% confidence range. Results are based on a global sample of observations aggregated over two experiment periods of around 3 months each.

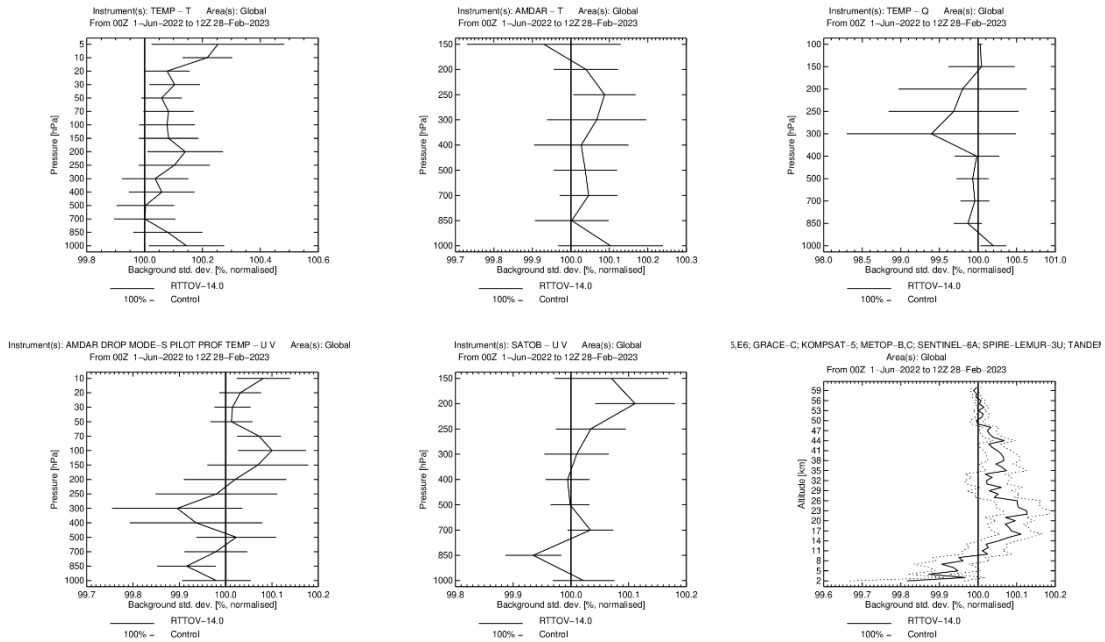


Figure 3.2.9: Change in the first guess fits to: temperature from radiosondes (top left), temperature from aircraft (top middle), humidity from radiosondes (top right), vector wind from radiosondes, profiler, pilot, and aircraft observations (bottom left), atmospheric motion vector winds (bottom middle) and GNSSRO bending angle (bottom right) for RTTOV v14 against the Control with RTTOV v13.2. Statistics cover the two seasons combined. Values are normalised to the control so that a shift left indicates a reduction in error. Horizontal lines indicate statistical significance at the 95 % level.

4. Summary

The latest version of RTTOV, RTTOV v14.0, has been validated in several ways to show similar or improved performance for the prediction of satellite top of atmosphere radiances for clear air, cloudy/hydrometeor-affected, and aerosol-affected profiles. It builds on previous versions of RTTOV. The changes have been validated as described in this document and in the further references to the new science implemented given herein. Referring to the list of changes made between RTTOV v13 and RTTOV v14 given in [section 2](#) the following comments can be made:

- The representation of the vertical profile has changed in v14 in respect of the way the pressure levels and layers are defined.

RTTOV's representation of the atmosphere is more closely aligned with that of NWP models. This change also allowed the unification of the RTTOV-SCATT model for microwave scattering simulations with the core RTTOV model (see below). This change has simplified the code, but it does mean that RTTOV v14 cannot replicate RTTOV v13 radiances.

- Updated microwave spectroscopy and coefficients for microwave sensors now include variable ozone.

New microwave gas optical depth coefficients have been made for the RTTOV v14 release based on updated water vapour and ozone spectroscopy. The new coefficients allow ozone as a variable gas for all microwave sensors to provide consistency across all instruments.

- Zeeman coefficients are available based on v13 predictors.

New Zeeman coefficients have been generated based on the v13 predictors. These are based on updated spectroscopy and supersede the previous coefficients based on the now-deprecated v7 predictors.

- Simulations for UV sensors are now possible.

RTTOV has been extended to support simulations at wavelengths down to $\sim 0.24 \mu\text{m}$. Validation against an alternative radiative transfer model showed reasonable agreement, but further work is planned, for example in extending the BRDF atlas down to UV wavelengths.

- Depolarisation is now accounted for in the Rayleigh scattering phase function.

This simple change mitigates a small source of error in the simulation of Rayleigh scattering.

- Scattering simulations for MW sensors are now done through the main RTTOV model. Science from the old RTTOV-SCATT model has been implemented in RTTOV.

All RTTOV-SCATT capabilities have been implemented within RTTOV and in some cases these have been enhanced (such as the generalisation of the dynamic emissivity retrieval outputs, and simultaneous calculation of passive radiances alongside radar reflectivities). Microwave scattering simulations are now run in a very similar way to those for infrared sensors from a technical perspective. This simplifies implementation of RTTOV for users. It also improves spectral consistency in scattering simulations through a unified representation of the atmosphere (see above) and by applying the same calculations for simulations at all wavelengths (for example, conversion of hydrometeor units). It also enables various capabilities to be shared across the spectrum (such as the application of the delta-Eddington solver to infrared sensors). Further work is planned in the future, for example to provide unified hydrometeor scattering optical properties across the whole spectrum.

- The Tang et al (2018) modification to the Chou-scaling fast solver for IR scattering has been implemented.

The initial implementation of this adjustment scheme for the existing fast scattering solver can improve simulations accuracy for ice clouds in the far infrared. Future developments are planned including generalising the adjustment to liquid cloud and aerosols.

- Implementation and improvement in the MFASIS-NN neural network based fast visible/near-IR scattering solver.

MFASIS-NN replaces the previous look-up table (LUT) version of MFASIS. MFASIS-NN is more accurate, more efficient, and more flexible than MFASIS-LUT. The implementation in v14 has been extended to support additional channels over the original implementation in v13.2. It will continue to be further developed for cloudy simulations and will be extended to support aerosol simulations in future RTTOV releases.

- Flexible VIS/IR hydrometeor optical properties.

This update brings the VIS/IR cloud/hydrometeor optical properties in line with the VIS/IR aerosol and MW hydrometeor optical properties. It provides a unified, extensible representation of scattering optical properties within the code and paves the way for supporting additional hydrometeor types in VIS/IR simulations (beyond cloud liquid and ice water), for generating fully spectrally consistent properties, and

for the creation of user-level tools to generate custom VIS/IR hydrometeor optical property files.

- New aerosol optical property tables are available defining optical properties for a subset of ICON-ART aerosol species.

These additional aerosol optical property files allow RTTOV to be used directly with ICON-ART fields for the supported aerosol species.

- MW hydrometeor optical property training options have been updated.

These updates extend the ranges of temperatures and water contents over which the optical properties are parameterised and include an improved treatment of the melting layer. In addition, it is possible to write out the Legendre decomposition of phase functions to microwave hydrotables for use with the DOM solver, although this is still undergoing testing and validation.

- A physically-based treatment of polarisation, ARO-scaling, has been implemented.

This extends the approximate simulation of polarisation differences between V- and H-pol channels to include microwave sounders as well as imagers. This new scheme is physically-based, unlike the previous empirical scheme for imagers only, and employs a look-up table for scaling all optical properties, instead of only the extinction. Further validation and testing of the new scheme is planned.

- Optional input of per-channel effective skin temperature.

This update allows for investigation of improved surface models, especially in the microwave, whereby effective skin temperatures may vary depending on frequency.

- A new neural network based MW sea surface emissivity model, SURFEM-Ocean, has been implemented.

The SURFEM-Ocean emissivity model, first implemented in v13.2, supports all microwave sensors simulated by RTTOV including those with channels in the sub-mm. This has become the recommended sea surface emissivity model for MW sensors.

- Treatment of heterogeneous surfaces.

RTTOV now provides the option to treat multiple surface types within the satellite footprint. This provides the potential for assimilation of sea-ice fraction as part of the state vector, for example.

- Updates to the treatment of diffuse reflectance in RTTOV.

The surface diffuse reflectance is now available as an input and output in the same way as surface emissivity and BRDF for all simulations. There is an improved treatment of sea surface BRDFs whereby the diffuse reflectance (whether RTTOV-computed or user-specified) is added to the BRDF allowing for greater consistency between BRDFs and diffuse reflectances (if the user has information about ocean colour, for example). Finally, the USGS water reflectance datasets have been updated and are now extended down to UV wavelengths.

- Support for the CAMEL v3 single-year and climatology IR land surface emissivity atlases.

This update brings RTTOV support for the latest versions of the CAMEL single year and climatology atlases. The CAMEL v3 single year atlas datasets are available for multiple years spanning 2003 – 2021 rather than only 2007 for CAMEL v2. The v3 atlases are strongly recommended over v2.

- Dynamic emissivity retrieval generalised to clear and all cloud overlap options.

The dynamic emissivity retrieval capability was previously only available in RTTOV-SCATT. It is now supported for clear-sky and scattering simulations using the fast solvers (delta-Eddington and Chou-scaling) for infrared and microwave sensors. It has also been generalised to all cloud overlap options supported by RTTOV.


- New/updated NLTE coefficients for IASI, IASI-NG, MTG-IRS based on LBLRTM v12.8.

The NLTE coefficients have been updated using LBLRTM 12.8 (consistent with the current VIS/IR optical depth coefficients), and a bug has been fixed that affected previous coefficients. Supported sensors now include IASI-NG and MTG-IRS in addition to IASI, CrIS, and AIRS.

- Updates to PC-RTTOV.

PC-RTTOV has been updated for RTTOV v14.0 with support for IASI, IASI-NG, and MTG-IRS. All previous PC-RTTOV capabilities (land/sea surfaces, all trace gases, NLTE correction, cloud, and aerosol simulations) are now supported by single PC coefficient files available for each sensor. The treatment of surface emissivity has also been updated.

This report refers to the version 14.0 of RTTOV. Higher number versions of RTTOV v14 will contain updated science and technical developments issued approximately once a year. These will be documented in the RTTOV v15 Science and Validation Report, but the interim

 <p>EUMETSAT NWP SAF NUMERICAL WEATHER PREDICTION</p>	<p>RTTOV v14 Science and Validation Report</p>	<p>Doc ID: NWPSAF-MO-TV-051 Version: 1.0.1 Date: 31/01/2025</p>
---	--	---

release notes will include some details of any changes. There may be updates to this document which will be posted on the NWP SAF web site so check the version number in the header.

5. Acknowledgements

The RTTOV v14 developments and validation described here were carried out as part of the EUMETSAT funded NWP SAF activities by the Met Office, ECMWF, DWD and Météo-France. In addition, contributions from other scientists including visiting and associate scientists are gratefully acknowledged.

6. References

R7REP2002 RTTOV v7 science and validation report available at:

https://nwp-saf.eumetsat.int/oldsite/deliverables/rtm/rttov7_svr.pdf

R8REP2006 RTTOV v8 science and validation report available at:

https://nwp-saf.eumetsat.int/oldsite/deliverables/rtm/rttov8_svr.pdf

R9REP2008 RTTOV v9 science and validation report available at:

https://nwp-saf.eumetsat.int/oldsite/deliverables/rtm/rttov9_files/rttov9_svr.pdf

R10REP2010 RTTOV v10 science and validation report available at:

https://nwp-saf.eumetsat.int/oldsite/deliverables/rtm/docs_rttov10/rttov10_svr_1.11.pdf

R11REP2013 RTTOV v11 science and validation report available at:

https://nwp-saf.eumetsat.int/site/download/documentation/rtm/docs_rttov11/rttov11_svr.pdf

R12REP2017 RTTOV v12 science and validation report available at:

https://nwp-saf.eumetsat.int/site/download/documentation/rtm/docs_rttov12/rttov12_svr.pdf

R13REP2020 RTTOV v13 science and validation report available at:

https://nwp-saf.eumetsat.int/site/download/documentation/rtm/docs_rttov13/rttov13_svr.pdf

Abadi, M., A. Agarwal, P. Barham *et al*, 2015: Tensor-Flow: Large-Scale Machine Learning on Heterogeneous Systems, <https://www.tensorflow.org/>.

Abel, S. and I. Boutle, 2012: An improved representation of the raindrop size distribution for single-moment microphysics schemes, *Q.J.R. Meteorol. Soc.*, **138**, 2151–2162.

Baordo, F. and A.J. Geer, 2016: Assimilation of SSMIS humidity-sounding channels in all-sky conditions over land using a dynamic emissivity retrieval. *Q.J.R. Meteorol. Soc.*, **142**, 2854-2866.

Barakas, V., A. J. Geer, and P. Eriksson, 2021: Introducing hydrometeor orientation into all-sky microwave and submillimeter assimilation, *Atmos. Meas. Tech.*, **14**, 3427–3447, <https://doi.org/10.5194/amt-14-3427-2021>.

Barakas, V., A. J. Geer, and P. Eriksson, 2022: Cloud particle orientation and polarisation for cross-track microwave sensors in RTTOV, *NWP SAF report*, https://nwp-saf.eumetsat.int/publications/vs_reports/nwpsaf-ec-vs-061.pdf (last access: 31 December 2024).

Bauer, P., 2001: Including a melting layer in microwave radiative transfer simulation for clouds, *Atmospheric research*, **57**, 9–30.

Bauer P., E. Moreau, F. Chevallier, and U. O’Keeffe, 2006: Multiple-scattering microwave radiative transfer for data assimilation applications. *Q.J.R. Meteorol. Soc.* **132**, 1259-1281.

Baur, F., L. Scheck, C. Stumpf, C. Köpken-Watts, and R. Potthast, 2023: A neural- network-based method for generating synthetic 1.6 μm near-infrared satellite images, *EGU Atm. Meas. Tech.*, **16**, 5305–5326, <https://doi.org/10.5194/amt-16-5305-2023>.

Borbas, E. E. and B. C. Ruston, 2010: The RTTOV UWiremis IR land surface emissivity module. *NWP SAF report*. https://www.nwpsaf.eu/publications/vs_reports/nwpsaf-mo-vs-042.pdf

Borbas, E., S. Hook, G. Hulley, M. Loveless, and R. Knuteson, 2023a: Combined ASTER and MODIS Emissivity database over Land (CAMEL) Emissivity Monthly Global 0.05Deg V003 [Data set]. NASA EOSDIS Land Processes Distributed Active Archive Center. Accessed 2024-10-16 from <https://doi.org/10.5067/MEaSURES/LSTE/CAM5K30EM.003>

Borbas, E., G. Hulley, M. Loveless, R. Knuteson, K. Cawse-Nicholson, and S. Hook, 2023b: MEaSURES Unified and Coherent Land Surface Temperature and Emissivity (LST&E) Earth System Data Record (ESDR): The Combined ASTER and MODIS Emissivity database over Land (CAMEL) Version 3 Algorithm Theoretical Basis Document and Users’ Guide, https://lpdaac.usgs.gov/documents/1612/CAMEL_V3_UG_ATBD.pdf

Bormann, N, A. Geer, S. English, 2012: Evaluation of the microwave ocean surface emissivity model FASTEM-5 in the IFS. *ECMWF Technical Memorandum 667*.

Bucholtz, A., 1995: Rayleigh-scattering calculations for the terrestrial atmosphere, *Appl. Optics*, **34**, 2765-2773.

Chou M.-D., K.-T. Lee, S.-C. Tsay, and Q. Fu, 1999: Parameterization for Longwave Scattering for Use in Atmospheric Models, *J. Clim.*, **12**, 1, 159-169, [https://doi.org/10.1175/1520-0442\(1999\)012%3C0159:PFCLSF%3E2.0.CO;2](https://doi.org/10.1175/1520-0442(1999)012%3C0159:PFCLSF%3E2.0.CO;2)

Deblonde, G., and S., English, 2001: Evaluation of the FASTEM-2 fast microwave oceanic surface emissivity model. *In Proceedings of the 11th International ATOVS Study Conference* (pp. 67–78).

Dinnat, E., S. English, C. Prigent, L. Kilic, M. Anguelova, S. Newman, T. Meissner, J. Boutin, A. Stoffelen, S. Yueh, B. Johnson, F. Weng, and C. Jimenez, 2023: PARMIO: A reference quality model for ocean surface emissivity and backscatter from the microwave to the infrared," *Bull. Am. Meteorol. Soc.*, **104**, 4, E742–E748. <https://doi.org/10.1175/BAMS-D-23-0023.1>

Elfouhaily, T., B. Chapron, K. Katsaros, and D. Vandemark, 1997: A unified directional spectrum for long and short wind-driven waves, *J. Geophys. Res.*, **102**(C7), 15781-15796, doi:10.1029/97JC00467.

Eresmaa, R., A. Benedetti, and A. P. McNally, 2012a: Diverse profile database of aerosol and trace gas concentrations from the Monitoring Atmospheric Composition and Climate short-range forecasts, *NWP SAF report*, https://nwp-saf.eumetsat.int/site/download/documentation/rtm/nwpsaf-ec-tr-015_macc_profile_dataset.pdf

Eresmaa, R., A. Benedetti, and A. P. McNally, 2012b: NWP SAF MACC 60L Profile Data [data set], <https://nwp-saf.eumetsat.int/site/software/atmospheric-profile-data>.

Eresmaa, R. and A. P. McNally, 2014: Diverse profile datasets from the ECMWF 137-level short-range forecasts, *NWP SAF report*, <https://nwp-saf.eumetsat.int/site/download/documentation/rtm/nwpsaf-ec-tr-017.pdf>.

Eresmaa, R. and A. P. McNally, 2016: NWP SAF 137L Profile Data [data set], <https://nwp-saf.eumetsat.int/site/software/atmospheric-profile-data>.

Eyre, J.R. and H.M. Woolf 1988: Transmittance of atmospheric gases in the microwave region: a fast model. *Applied Optics*, **27**, 3244-3249.

Eyre, J. R., 1991: A fast radiative transfer model for satellite sounding systems. *ECMWF Technical Memorandum 176*.

Fielding, M. and M. Janisková, 2020: Direct 4D-Var assimilation of space-borne cloud radar reflectivity and lidar backscatter. Part I: Observation operator and implementation, *Q.J.R. Meteorol. Soc.*, **146**, 3877–3899.

Gasch, P., D. Rieger, C. Walter, P. Khain, Y. Levi, P. Knippertz, and B. Vogel, 2017: Revealing the meteorological drivers of the September 2015 severe dust event in the Eastern Mediterranean, *Atmos. Chem. Phys.* **17**, 13573-13604

Geer A.J., P. Bauer and C. W. O'Dell, 2009a: A revised cloud overlap scheme for fast microwave radiative transfer in rain and cloud, *J. App. Met. Clim.*, **48**, 2257–2270

Geer, A.J., R.M. Forbes and P. Bauer, 2009b: Cloud and precipitation overlap in simplified scattering radiative transfer, *EUMETSAT/ECMWF Fellowship Programme Research Report no. 18*. <https://www.ecmwf.int/sites/default/files/elibrary/2009/9516-cloud-and-precipitation-overlap-simplified-scattering-radiative-transfer.pdf>

Geer, A., C. Lupu, D. Duncan, N. Bormann, and S. English, 2024: SURFEM-ocean microwave surface emissivity evaluated. *ECMWF Technical Memorandum 915*.

<https://www.ecmwf.int/sites/default/files/elibrary/022024/81550-surfem-ocean-microwave-surface-emissivity-evaluated.pdf>

Han, Y., F. Weng, Q. Liu, and P. van Delst, 2007: A fast radiative transfer model for SSMIS upper atmosphere sounding channels. *Journal of Geophysical Research: Atmospheres*, **112** (D11).

<https://doi.org/10.1029/2006JD008208>

Hocking, J., 2014: Interpolation methods in the RTTOV fast radiative transfer model. *Met Office Forecasting Research Technical Report 590*.

https://digital.nmla.metoffice.gov.uk/download/file/digitalFile_911bd873-f30f-4617-9810-ad73b5457ea1

Hook, S., 2017: Combined ASTER and MODIS Emissivity database over Land (CAMEL) Coefficient Monthly Global 0.05Deg V002 [Data set]. Distributed by NASA EOSDIS Land Processes DAAC. <https://doi.org/10.5067/MEaSURES/LSTE/CAM5K30CF.002>

Hulley, G., S. Veraverbeke, and S. Hook, 2014: Thermal-based techniques for land cover change detection using a new dynamic MODIS multispectral emissivity product (MOD21). *Remote Sensing of Environment*, **140**, 755-765. <https://doi.org/10.1016/j.rse.2013.10.014>

Hulley, G., and S. Hook, 2021: MODIS/Aqua Land Surface Temperature/3-Band Emissivity Monthly L3 Global 0.05Deg CMG V061 [Data set]. Distributed by NASA EOSDIS Land Processes DAAC, <https://doi.org/10.5067/MODIS/MYD21C3.061>.

Illingworth, A. J. and T. M. Blackman, 2002: The need to represent raindrop size spectra as normalized gamma distributions for the interpretation of polarization radar observations, *J. App. Met.*, **41**, 286–297

Johnson, B., W. Olson, and G. Skofronick-Jackson, 2016: The microwave properties of simulated melting precipitation particles: Sensitivity to initial melting, *Atmos. Meas. Tech.*, **9**, 9–21.

Jonkheid, B. J., R. A. Roebeling, and E. van Meijgaard, 2012: A fast SEVIRI simulator for quantifying retrieval uncertainties in the CM SAF cloud physical property algorithm, *Atmos. Chem. Phys.*, **12**, 10957–10969, <https://doi.org/10.5194/acp-12-10957-2012>

Kilic L., C. Prigent, C. Jimenez, E. Turner, J. Hocking, S. English, T. Meissner, and E. Dinnat, 2023: Development of the SURface Fast Emissivity Model for Ocean (SURFEM-Ocean) Based on the PARMIO Radiative Transfer Model. *Earth and Space Science*, **10**, 11, <https://doi.org/10.1029/2022EA002785>.

Kokaly, R.F., R.N. Clark, G.A. Swayze, K.E. Livo, T.M. Hoefen, N.C. Pearson, R.A. Wise, W.M. Benzel, H.A. Lowers, R.L. Driscoll, and A.J. Klein, 2017: USGS Spectral Library Version 7: U.S. Geological Survey Data Series 1035, 61 p., <https://doi.org/10.3133/ds1035>.

Labonnote, L., J. Hocking, and J. Vidot, 2022: Improvement of the scattering parameterisation in RTTOV. *NWP SAF report*. https://nwp-saf.eumetsat.int/publications/vs_reports/nwpsaf-mo-vs-059.pdf

Larsson, R., B. Lankhaar, and P. Eriksson, 2019: Updated Zeeman effect splitting coefficients for molecular oxygen in planetary applications. *J. Quant. Spectrosc. and Rad. Transfer*, **224**, 431-438. <https://doi.org/10.1016/j.jqsrt.2018.12.004>

Loveless, M., E.E. Borbas, R. Knuteson, K. Cawse-Nicholson, G. Hulley, and S. Hook, 2021: Climatology of the Combined ASTER MODIS Emissivity over Land (CAMEL) Version 2. *Remote Sens*, **13**, 111. <https://doi.org/10.3390/rs13010111>

Mangla, R., M. Borderies, P. Chambon, A. Geer, and J. Hocking, 2025: Assessment and application of melting layer simulations for spaceborne radars within the RTTOV-SCATT v13.1 model, *Atmos. Meas. Tech. Discuss.* [preprint], <https://doi.org/10.5194/amt-2024-131>, in review.

Marshall, J. S., and W. M. Palmer, 1948: The distribution of raindrops with size, *Journal of Meteorology*, **5**, 165-166.

Matricardi, M., F. Chevallier, G. Kelly G, and J.-N. Thepaut, 2004: An improved general fast radiative transfer model for the assimilation of radiance observations. *Q.J.R. Meteorol. Soc.*, **130**, 153-173.

Matricardi M., M. López Puertas, and B. Funke, 2018: Modelling of nonlocal thermodynamic equilibrium effects in the principal component based version of the RTTOV fast radiative transfer model. *JGR Atmos.* **123**, 11, 5741-5761 <https://doi.org/10.1029/2018JD028657>

Matricardi, M., 2024: Enhancing the capabilities of the PC-RTTOV model, *NWP SAF report*, https://nwp-saf.eumetsat.int/publications/vs_reports/nwpsaf-ec-vs-063.pdf

Meissner, T., and F. J. Wentz, 2004: The complex dielectric constant of pure and sea water from microwave satellite observations. *IEEE Transactions on Geoscience and Remote Sensing*, **42**(9), 1836–1849. <https://doi.org/10.1109/tgrs.2004.831888>

Meissner, T., and F. J. Wentz, 2012: The emissivity of the ocean surface between 6 and 90 GHz over a large range of wind speeds and Earth incidence angles. *IEEE Transactions on Geoscience and Remote Sensing*, **50**(8), 3004–3026. <https://doi.org/10.1109/tgrs.2011.2179662>

Meng, Z., P. Yang, G. W. Kattawar, L. Bi, K. N. Liou, and I. Laszlo, 2010: Single-scattering properties of tri-axial ellipsoidal mineral dust aerosols: A database for application to radiative transfer calculations, *J. Aerosol Science*, **41** (5), 501-512, <https://doi.org/10.1016/j.jaerosci.2010.02.008>

Muser, L., C. Stumpf, L. Scheck, and C. Köpken-Watts, 2022: Preparing an extension of RTTOV-DOM for application to ICON-ART aerosol, *NWP SAF report*, https://nwp-saf.eumetsat.int/publications/vs_reports/nwpsaf-dwd-vs-059.pdf

Rochon, Y., L. Garand, D.S. Turner and S. Polavarapu, 2007: Jacobian mapping between vertical co-ordinate systems in data assimilation. *Q.J.R. Meteorol. Soc.*, **133**, 1547-1558.

Rosenkranz, P. W., and D. H. Staelin, 1988: Polarized thermal microwave emission from oxygen in the mesosphere. *Radio science*, **23** (05), 721-729. <https://doi.org/10.1029/RS023i005p00721>

Rosenkranz, P. W., 2023: Line-by-line microwave radiative transfer (non-scattering) [software] (version 2023/07/24) http://cetemps.aquila.infn.it/mwrnet/lblmrt_ns.html

Rothman, L. S., C. P. Rinsland, A. Goldman, S. T. Massie, D. P. Edwards, J. M. Flaud, ..., and P. Varanasi, 1998: The HITRAN molecular spectroscopic database and HAWKS (HITRAN atmospheric workstation): 1996 edition. *J. Quant. Spectrosc. and Rad. Transfer*, **60** (5), 665-710. [https://doi.org/10.1016/S0022-4073\(98\)00078-8](https://doi.org/10.1016/S0022-4073(98)00078-8)

Rothman, L. S., I. E. Gordon, Y. Babikov, A. Barbe, D. C. Benner, P. F. Bernath, ... and G. Wagner, 2013: The HITRAN2012 molecular spectroscopic database. *J. Quant. Spectrosc. and Rad. Transfer*, **130**, 4-50. <https://doi.org/10.1016/j.jqsrt.2013.07.002>

Saunders, R.W., M. Matricardi, and P. Brunel, 1999a: A fast radiative transfer model for assimilation of satellite radiance observations - RTTOV-5. *ECMWF Technical Memorandum 282*.

Saunders, R.W., M. Matricardi, and P. Brunel, 1999b: An Improved Fast Radiative Transfer Model for Assimilation of Satellite Radiance Observations. *Q.J.R. Meteorol. Soc.*, **125**, 1407-1425.

Saunders, R., J. Hocking, E. Turner, P. Rayer, D. Rundle, P. Brunel, J. Vidot, P. Roquet, M. Matricardi, A. Geer, N. Bormann, and C. Lupu, 2018: An update on the RTTOV fast radiative transfer model (currently at version 12), *Geosci. Model Dev.*, **11**, 2717–2737, <https://doi.org/10.5194/gmd-11-2717-2018>

Scanlon, T., A. Geer, and N. Bormann, 2023: Microwave imagers in the IFS: adding further observations and improving convective anvils in the observation operator, *EUMETSAT/ECMWF Fellowship Programme Research Report no. 61*. https://www.ecmwf.int/sites/default/files/elibrary/2023/81347-microwave-imagers-ecmwf-ifs-adding-further-observations-and-improving-convective-anvils_1.pdf

Scheck, L. P. Frèrebeau, R. Buras-Schnell, and B. Mayer, 2016: A fast radiative transfer method for the simulation of visible satellite imagery, *J. Quant. Spectrosc. and Rad. Transfer*, **175**, 54-67, ISSN 0022-4073, <https://doi.org/10.1016/j.jqsrt.2016.02.008>.

Scheck, L., 2021a: A neural network based forward operator for visible satellite images and its adjoint, *J. Quant. Spectrosc. and Rad. Transfer*, **274**, 107841, ISSN 0022-4073, <https://doi.org/10.1016/j.jqsrt.2021.107841>.

Scheck, L., 2021b: FORNADO, GitLab [code], <https://gitlab.com/LeonhardScheck/fornado>.

Tang, G., P. Yang, G. W. Kattawar, X. Huang, E. J. Mlawer, B. A. Baum, and M. King, 2018: Improvement of the simulation of Cloud Longwave Scattering in Broadband Radiative Transfer Models, *J. Atmos. Sci.*, **75**, 7, 2217 – 2233, 2018, <https://doi.org/10.1175/JAS-D-18-0014.1>

Tretyakov, M. Y., M. A. Koshelev, V. V. Dorovskikh, D. S. Makarov, and P. W. Rosenkranz, 2005: 60-GHz oxygen band: precise broadening and central frequencies of fine-structure lines, absolute absorption profile at atmospheric pressure, and revision of mixing coefficients. *Journal of molecular spectroscopy*, **231** (1), 1-14. <https://doi.org/10.1016/j.jms.2004.11.011>

Turner E. and R. Saunders, 2019a: Sub-millimetre Spectroscopy for AMSUTRAN. Part One: The Theoretical Basis, *NWP SAF Report NWPSAF-MO-TR-038*, https://nwp-saf.eumetsat.int/publications/tech_reports/amsutran_1Thz_NWPSAF_report.pdf

Turner, E., P. Rayer, and R. Saunders, 2019b: AMSUTRAN: A microwave transmittance code for satellite remote sensing. *J. Quant. Spectrosc. and Rad. Transfer*, **227**, 117-129, <https://doi.org/10.1016/j.jqsrt.2019.02.013>

Turner, E., S. Fox, V. Mattioli, and D. Cimini, 2022: Literature Review on Microwave and Sub-millimetre Spectroscopy for MetOp Second Generation. *NWP SAF report*, NWPSAF-MO-TR-039, https://nwp-saf.eumetsat.int/site/download/members_docs/cdop-3_reference_documents/NWPSAF_report_submm_litrev.pdf

Wang, P. and O. Tuinder, 2022: Comparison of RTTOV and DISAMAR for clear sky and aerosol cases. *NWP SAF report*. https://nwp-saf.eumetsat.int/publications/vs_reports/nwpsaf-ec-vs-062.pdf (last access: 31 December 2024).

End of Report